University of Alberta

*Characterization and Prediction of Delamination in Fiber-reinforced Composites*

by

Chengye Fan ©

A thesis submitted to the Faculty of Graduate Studies and Research in partial fulfillment of the requirements for the degree of *Doctor of Philosophy*

Department of Mechanical Engineering

Edmonton, Alberta

Spring 2008

Library and Archives Canada

Published Heritage Branch

395 Wellington Street
Ottawa ON K1A 0N4
Canada

Bibliothèque et Archives Canada

Direction du Patrimoine de l'édition

395, rue Wellington
Ottawa ON K1A 0N4
Canada

*Your file Votre référence*
*ISBN: 978-0-494-45423-7*
*Our file Notre référence*
*ISBN: 978-0-494-45423-7*

NOTICE:
The author has granted a non-exclusive license allowing Library and Archives Canada to reproduce, publish, archive, preserve, conserve, communicate to the public by telecommunication or on the Internet, loan, distribute and sell theses worldwide, for commercial or non-commercial purposes, in microform, paper, electronic and/or any other formats.

The author retains copyright ownership and moral rights in this thesis. Neither the thesis nor substantial extracts from it may be printed or otherwise reproduced without the author's permission.

AVIS:
L'auteur a accordé une licence non exclusive permettant à la Bibliothèque et Archives Canada de reproduire, publier, archiver, sauvegarder, conserver, transmettre au public par télécommunication ou par l'Internet, prêter, distribuer et vendre des thèses partout dans le monde, à des fins commerciales ou autres, sur support microforme, papier, électronique et/ou autres formats.

L'auteur conserve la propriété du droit d'auteur et des droits moraux qui protège cette thèse. Ni la thèse ni des extraits substantiels de celle-ci ne doivent être imprimés ou autrement reproduits sans son autorisation.

---

In compliance with the Canadian Privacy Act some supporting forms may have been removed from this thesis.

While these forms may be included in the document page count, their removal does not represent any loss of content from the thesis.

Conformément à la loi canadienne sur la protection de la vie privée, quelques formulaires secondaires ont été enlevés de cette thèse.

Bien que ces formulaires aient inclus dans la pagination, il n'y aura aucun contenu manquant.

Canada

## Abstract

This thesis discusses methodologies for experimental measurement of delamination resistance and the prediction of delamination development in fiber-reinforced composites in mixed or pure fracture modes using analytical approaches or finite element methods.

A new test method, named internal-notched flexure (INF) test, was developed to measure the composites' resistance to delamination growth in pure shear mode. Experiments and theoretical analysis have shown that the INF test generates unconditionally stable delamination growth, with monotonic increase of load and displacement in a nearly linear way. The resistance curve (R-curve) associated with the delamination growth in the INF test was established using a new data reduction method, the direct method with final crack length correction (DMC). Compared to the R-curves by the traditional compliance calibration method, the DMC avoids difficulties of in-situ crack length measurement, thus improve consistency of the results. Through a series of tests with different setup configurations and fiber content, the mode II delamination resistance was found to be independent of setup configuration but decreases with the increase of fiber volume fraction.

A cohesive damage material model was developed for the simulation of delamination onset and propagation using finite element method. The cohesive damage material model adopts delamination toughness to govern the damage evolution and uses a multi-axial-stress-based criterion to predict the damage initiation, so that the model is able to show the hydrostatic stress effect. This material model can also address some issues related to mode-II-dominated delamination such as the frictional force effect. The validity of the model was firstly examined by simulating delamination growth in pre-

cracked coupon specimens of fiber composites, including stable/unstable delamination growth in pure/mixed fracture mode. The material model was then used to simulate delamination in a composite specimen for without starting defects (or a pre-crack). The results were compared with those from experimental studies, for physical location of the delamination initiation and the final crack size developed. In addition, thesis also presents a parametric study that investigates the influence of material strength on the delamination initiation in composites with or without initial defects.

## Acknowledgements

I am sincerely thankful to my supervisor, Dr. Jar and Dr. Cheng, for their guidance during the course of PhD study. With their consistent support, I was never worried about getting stuck in doing research, which troubled many of graduate students. I am also grateful to Dr. Takashi Kuboki and Mr. Bernie Faulkner for their assist in doing test. Appreciation is extended to members of the Durable Materials Research Lab: HJ, Yemi, Tik, Riski, Jie, Paul and Souvenir for their friendship and the provision of a pleasant environment. Finally, my gratitude must be given to my wife, Ye Tang. She always trust and encourage me for pursuing the excellence.

# Table of Content

**Chapter 1 Introduction** ..... **1**
1.1 Background ..... 1
1.2 Aims and scope ..... 3
1.3 Structure of thesis ..... 6

**Chapter 2 Analytical Methods for the Calculation Energy Release Rate** ..... **9**
2.1 Introduction ..... 9
2.2 Compliance method ..... 10
2.2.1 The energy release rate in cracked beams ..... 11
2.2.2 Energy release rate in cracked plates ..... 25
2.3 Crack tip element analysis ..... 30
2.3.1 Crack tip element theory ..... 30
2.3.2 Frictional force effect on $G$ in mode II delamination tests ..... 35
2.4 Concluding remarks ..... 39

**Chapter 3 FEM Based Techniques for the Calculation of Energy Release Rate** ..... **40**
3.1 Review of the existing FEM-based methods ..... 40
3.1.1 Compliance derivative technique ..... 41
3.1.2 Virtual crack closure technique ..... 41
3.1.3 The $J$-integral ..... 43
3.2 Energy derivative technique ..... 44
3.2.1 Principle of the energy derivative technique ..... 44
3.2.2 Special forms of the $G$ expression ..... 46
3.2.3 Example: $G$ of a penny-shaped crack in a plate ..... 47
3.2.4 Example: $G$ of a cracked beam under 3-point bending ..... 50
3.3 Frictional force effect on $G$ using the EDT ..... 52
3.3.1 Expression of $G$ with friction and constant force loading ..... 52
3.3.2 Frictional force effect in the ENF and 4ENF tests ..... 55
3.4 Applications of energy derivative technique in nonlinear fracture ..... 58
3.4.1 Central crack in a rubber sheet ..... 58
3.4.2 Double-edge-notched tensile test ..... 62
3.5 Concluding remarks ..... 68

**Chapter 4 Delamination Tests for Measuring the Critical Energy Release Rates ... 69**
4.1 Introduction ... 69
4.2 The internal notched flexure test ... 73
4.2.1 Test setup ... 73
4.2.2 Analysis on the INF test ... 74
4.2.3 Experimental details ... 79
4.2.4 Data reduction methods ... 82
4.2.5 The effect of fiber volume fraction on $G_{IIC}$ ... 91
4.3 Beam test ... 100
4.3.1 Introduction to the beam test ... 100
4.3.2 Test details and results ... 101
4.3.3 Vibration energy in the Beam test ... 104
4.4 Concluding remarks ... 108

**Chapter 5 Analytical Prediction of Delamination Development in the Beam Test 110**
5.1 Introduction ... 110
5.2 Prediction of delamination crack path ... 111
5.2.1 Criteria for crack growth direction ... 111
5.2.2 Crack path in the Beam test ... 112
5.3 Prediction of the delamination crack length ... 116
5.3.1 Based on the energy release rate ... 116
5.3.2 Based on the balance of total energy ... 118
5.4 Concluding remarks ... 121

**Chapter 6 Finite Element Simulation of Delamination ... 122**
6.1 Introduction ... 122
6.2 Cohesive damage material ... 125
6.2.1 Constitutive relationship ... 126
6.2.2 Damage initiation criterion ... 127
6.2.3 Damage evolution law ... 128
6.2.4 Stress-strain response in pure mode fracture ... 130
6.2.5 Special issues related to mode II fracture ... 133
6.3 Application to pre-cracked composites ... 139
6.3.1 FEM models ... 140

6.3.2 The DCB test ..... 142
6.3.3 The ENF test ..... 143
6.3.4 The ELS test ..... 145
6.3.5 The MMB test ..... 146
6.4 Application to the defect-free Beam test ..... 149
6.4.1 Experimental results from the Beam test ..... 149
6.4.2 FEM simulation of the Beam test ..... 150
6.5 Conclusions ..... 161

**Chapter 7 Conclusions and Future Work ..... 164**
7.1 Main conclusions ..... 164
7.2 Future work ..... 167

**References ..... 170**

# List of Tables


Table 3.1 FEM-based techniques for the energy release rate and their application conditions ("Y" means applicable while "-" means not applicable)..... 46

Table 3.2 Material and geometrical properties used in the penny-shaped crack model. ..... 47

Table 3.3 Material properties of the cracked beam..... 52

Table 3.4 Material and geometrical properties used in the rubber sheet model. ..... 59

Table 3.5 Material and geometrical properties used in the DENT model. ..... 62

Table 4.1 Predicted stabilities in mode II delamination tests. ..... 77

Table 4.2 The specifications of the INF specimens and test setup ..... 93

Table 4.3 Results the Beam test with varied span lengths. ..... 103

Table 5.1 Mechanical properties of the Beam test specimens ..... 116

Table 5.2 Comparison of the results from the Beam test and those predicted using the approaches based on $G$ (ERR) and change of total energy (TE). ..... 118

Table 6.1 Geometrical parameters of the DCB, ENF and ELS tests. ..... 140

Table 6.2 Material properties for unidirectional fiber composites used in the study. 141

Table 6.3 Properties for cohesive damage materials and parameters for the cohesive damage material model. ..... 141

# List of Figures


Figure 1.1 Scope of thesis. ..... 5

Figure 1.2 Configurations of the DCB, MMB, ENF, ELS and 4ENF tests. ..... 8

Figure 2.1 Sign conventions for displacements and rotation angle ..... 12

Figure 2.2 Sign conventions for bending moment $M$, shear force $Q$, and distributed shear force $q$ on an beam element. ..... 13

Figure 2.3 Free body diagram of a beam element for equilibrium ..... 13

Figure 2.4 Illustration of the deformation in a Timoshenko beam ..... 14

Figure 2.5 Poisson's ratio effect in (a) a narrow beam, and (b) a wide beam. ..... 17

Figure 2.6 Crack configurations in a beam subjected to 3-point bending ..... 18

Figure 2.7 Diagrams for beam analysis: (a) upper beam model; (b) free body diagram of the upper beam; and (c) boundary conditions. ..... 20

Figure 2.8 Deformation mechanism of a beam with shear force. ..... 25

Figure 2.9 Penny-shaped crack embedded in a plate. ..... 28

Figure 2.10 Schematic illustration of the superposition ..... 29

Figure 2.11 Free body diagrams for (a) crack tip element, and (b) half crack tip element ..... 31

Figure 2.12 Free body diagram for determining $F_C$. ..... 35

Figure 2.13 Schematic free body diagram of a half beam ..... 36

Figure 2.14 The free body diagram of upper half of an ENF specimen ..... 37

Figure 3.1 Mesh at the crack tip for the VCCT ..... 42

Figure 3.2 Definition of the $J$-integral ..... 44

Figure 3.3 Penny-shaped crack in a plate: (a) the FEM model, (b) plot of $U$ versus $a$ for two different meshes, and (c) $G$ by the EDT and the analytical solution. ... 49

Figure 3.4 Predefined crack path in the cracked beam..... 50

Figure 3.5 Comparison between FEM and analytical solution: (a) compliance and (b) the energy release rate, $G$..... 51

Figure 3.6 Monotonic load-displacement curves for crack growth with friction..... 55

Figure 3.7 FEM model of the ENF test for studying the frictional force effect..... 56

Figure 3.8 The frictional force effect in the ENF and 4ENF tests, predicted by analytical solution, the EDT and the VCCT. ..... 58

Figure 3.9 Rubber sheet with a central crack in tension: (a) geometries, (b) FEM model, and (c) comparison of $G$ values from the EDT and Eq. (3.15). ..... 62

Figure 3.10 Plastic deformation of DENT test: (a) specimen configuration, and (b) FEM model..... 63

Figure 3.11 Stress-strain curves based on the incremental plasticity theory and the deformation plasticity theory. ..... 64

Figure 3.12 Values of $h_1$ for the DENT model using the EDT based on the deformation plasticity theory, and the comparison with those in the literature. ..... 67

Figure 3.13 Values of $h_1$ for the DENT model using the EDT, based on the incremental plasticity theory..... 67

Figure 4.1 Typical fracture surface topographies of (a) mode I fracture and (b) mode II fracture. ..... 70

Figure 4.2 Schematic load displacement curves of the ENF, ELS, 4ENF and INF tests. ..... 72

Figure 4.3 The INF test setup. ..... 73

Figure 4.4 Schematic load-displacement curve of the INF test, with varied initial crack length and $G_C$. ..... 74

Figure 4.5 Glass fiber with/without stitching threads. ..... 79

Figure 4.6 Photograph of an INF specimen taken during testing..... 80

Figure 4.7 The INF test results, load-displacement curve and crack growth against displacement. ..... 81

Figure 4.8 Determine $G_{IIC}$ by direct method. ..... 82

Figure 4.9 *R*-curve obtained by direct method. ..... 83

Figure 4.10 Photograph of a post-tested INF specimen showing bridging fibers between the fracture surfaces. ..... 84

Figure 4.11 Side view of the matrix hackles on the crack surfaces from SEM. ..... 85

Figure 4.12 Comparison of R-curves by DM, DMC, CC method and area method. ..... 86

Figure 4.13 Calculated crack length versus visual crack length for verifying the linear mapping, "×" represent calculated crack lengths without mapping and "•" representing those with mapping. ..... 87

Figure 4.14 Linear curve fitting for the INF test. ..... 89

Figure 4.15 Glass fiber preform with stitching fibers. ..... 92

Figure 4.16 Typical load-displacement curve and crack length history of the INF test with stitching threads on the delamination growth path. ..... 94

Figure 4.17 SEM pictures of stitching fiber: (a) side view and (b) front view. ..... 95

Figure 4.18 *R*-curves obtained by DM, DMC and area method ..... 96

Figure 4.19 Typical load-displacement curve of 4ENF test. ..... 97

Figure 4.20 Typical *R*-curves built by the DM and DMC base on the 4ENF test. ..... 97

Figure 4.21 Average $G_{IIC}$ versus fiber volume fraction. ..... 98

Figure 4.22 Average $G_{IIC}$ versus half span length, $L$ ..... 99

Figure 4.23 Average $G_{IIC}$ versus initial crack length, $a_0$. ..... 99

Figure 4.24 Typical load displacement curves of the Beam test with span length 30, 40, 50 and 60 mm ..... 101

Figure 4.25 Matrix cracking (pointed by a white arrow) and delamination (black arrows) in a beam specimen. ..... 102

Figure 4.26 Crack length and location measurement. ..... 102

Figure 4.27 Photographs of the beam vibration: (a) beam deflection before delamination, and (b) beam deflection after delamination at the lowest position during vibration. ..... 104

Figure 4.28 Vibration motion of the Beam test specimen. ..... 105

Figure 4.29 Schematic description of two modes of motion used to simulate the vibration. ..... 107

Figure 5.1 The process for delamination development in the Beam test: (a) stage 1, (b) stage 2, and (c) stage 3. ..... 115

Figure 5.2 Variation of $G$ with delamination length for a beam specimen subject to constant deflection. ..... 117

Figure 5.3 Total energy change during the delamination growth when subjected to constant deflection. ..... 119

Figure 6.1 Schematic of the cohesive zone model. ..... 123

Figure 6.2 Finite element model for determining load-displacement response in opening mode fracture. ..... 130

Figure 6.3 The developments of stress and damage parameters with strain. ..... 132

Figure 6.4 Swelling due to mode II fracture and coarse fracture surface. ..... 134

Figure 6.5 Modeling the swelling in the cohesive damage material model: (a) undeformed state and (b) with shear deformation. ..... 135

Figure 6.6 Single element for obtaining stress-strain curve and the loading history. . 137

Figure 6.7 The development of stresses under pure mode II loading with swelling effect and friction. ..... 139

Figure 6.8 The mesh pattern for the DCB, ENF, ELS and MMB tests. ..... 142

Figure 6.9 Load-displacement curves for the DCB test. ..... 143

Figure 6.10 The load-displacement curves of the ENF test. ..... 144

Figure 6.11 The load-displacement curves of the ELS test by the analytical solution and the FEM predictions with varied shear strengths..... 146

Figure 6.12 Comparison between the FEM results and the analytical solutions in the MMB test: (a) load-displacement curves; and (b) mode mixing ratio..... 148

Figure 6.13 The finite element mode of Beam test. ..... 150

Figure 6.14 Comparisons of the load-displacement curves from Beam tests for (a) 1/2-beam, (b) 1/4-beam, and (c) 3/4-beam. ..... 152

Figure 6.15 Comparisons of the delamination onset locations in the Beam test for (a) 1/2-beam, (b) 1/4-beam, and (c) 3/4-beam. ..... 154

Figure 6.16 Comparisons of the final delamination area generated by the Beam test for (a) 1/2-beam, (b) 1/4-beam, and (c) 3/4-beam. ..... 156

Figure 6.17 Parametric study of the effect of $\sigma_{33}$ in the 1/4-Beam test: (a) load-displacement curves, and (b) the resulting delamination area with and without the consideration of $\sigma_{33}$. ..... 158

Figure 6.18 Parametric study of the effect of material strength ($T$ and $S$) in the 1/4-beam test: (a) load-displacement curves, and (b) the resulting delamination area. ..... 159

Figure 6.19 Load-displacement curves of the 1/2-beam with the swelling effect and friction. ..... 161

Figure 6.20 Residual strain in the 1/2-beam due to the swelling effect. ..... 161

# List of Symbols

| | |
|---|---|
| $A$ | crack area |
| $A_{cr}$ | cross-section area |
| $A_0, A_2 \ldots A_7$ | coefficients in differential equations |
| [A], [B], [C] | constant matrixes in the CTE analysis |
| $a$ | crack length |
| $a_0$ | initial crack length |
| $a_1$ | crack tip position, measured from loading pin to the tip which is farther than the other. |
| $a_2$ | crack tip position, measured from loading pin to the tip which is nearer than the other. |
| $B$ | width of a beam |
| $B_V$ | maximum displacement during vibration |
| $B_0, B_2 \ldots B_7$ | coefficients in differential equations |
| $b$ | opening distance of a elliptical crack in a rubber-like material |
| C | compliance |
| $C_{10}, C_{20}, C_{30}$ | constants for strain energy density function in a hyper-elastic material model |
| $C_0, C_1$ | constants for the expression of $C$ |
| $C_0$ | initial compliance without crack |
| $c$ | half ligament length in DENT test |
| $c_{MMB}$ | geometrical parameter in MMB test |
| $D$ | bending rigidity of a plate |
| $d$ | damage parameter |
| $d^E$ | damage parameter in terms of energy |
| $E$ | Young' modulus of elasticity |
| $E_{11}$ | Young' modulus of in local 1-direction |
| $E_{ijkl}$ | component of the elasticity tensor |
| $e_f$ | frictional force effect |

| | |
|---|---|
| $F$ | work of friction |
| $F_C$ | concentrated force acting on the crack tip |
| $F_{c1}$, $F_{c2}$ | nodal forces in the 1- and 2-direction at node 'c' |
| $f$ | foefficient governing frictional force effect |
| $f_r$ | vibration frequency |
| $f_i$ | frictional force |
| $G$ | energy release rate |
| $G_{a1}$ | energy release rate, associated with crack growth in $a1$ direction |
| $G_{a2}$ | energy release rate, associated with crack growth in $a2$ direction |
| $G_0$ | energy release rate without friction |
| $G_f$ | energy release rate with friction |
| $G_C$ | critical energy release rate |
| $G_{IC}$, $G_{IIC}$ | mode I or II critical energy release rate |
| $H$ | beam thickness |
| $h_1$ | coefficient in the expression of the $J$-integral for DENT test |
| **I** | unit 2nd order tensor |
| $I_1$, $I_2$ | 1st and 2nd invariables of left Cauchy-green strain tensor |
| $J$ | the J-integral |
| $J_C$ | threshold value of the J-integral |
| $K$ | Stress intensity factor |
| $K_C$ | threshold value of $K$ |
| $k$ | coefficient for mapping an R-curve |
| $k_{sh}$ | correction factor for shear force deformation in beams |
| $L$ | half span length of experimental setup |
| $l$ | overhanging length of in the Beam test |
| $l_{cz}$ | size of cohesive zone |
| $M$ | bending moment |
| $M_C$ | concentrated moment acting on the crack tip |
| [N] | Matrix of concentrated force at the crack tip |
| $N(x)$ | axial force |
| n | exponent in Ramberger-Osgood model |

| | |
|---|---|
| $\mathbf{n}$ | normal of a curve, in the definition of the *J*-integral |
| $P$ | concentrated force |
| $p$ | distributed force |
| $P_1, P_2$ | equivalent concentrated force components for the DCB- and ENF-type loading |
| $P_{max}$ | maximum force in the Beam test |
| $P_i$ | external load |
| $Q$ | shear force |
| $q$ | distributed shear force |
| $\mathbf{q}$ | a unit vector in crack advance direction, |
| $R$ | radius |
| $r$ | radius |
| S | shear strength |
| T | tensile strength |
| $t$ | ratio of crack growth in $da_1$ to $da$ |
| $t_0$ | original thickness of cohesive zone |
| $U$ | strain energy |
| | strain energy density |
| $U_D$ | dissipated energy |
| $U_K$ | kinetic energy |
| $U_K^{max}$ | maximum kinetic energy |
| $U_I, U_{shear}$ | energy consumed per unit area by opening or shear fracture |
| $\mathbf{u}$ | displacement vector |
| $u, v, w$ | displacement in the x-, y- or z-direction |
| $u_1, u_2, u_3$ | displacement in the 1-, 2- or 3-direction |
| $u_0$ | displacement on the neutral axis in the x-direction |
| $W$ | external work |
| $W_I$ | strain energy density function for a hyper-elastic material model |
| $w_{\bar{0}}$ | displacement on the neutral axis in the z-direction |
| $\alpha$ | "yield" offset in Ramberg-Osgood model |
| | coefficient in the damage onset criteria |

| | |
|---|---|
| $\beta$ | mode-mixing ratio |
| $\gamma$, $\gamma_{xy}$ | shear strain |
| $\Delta$ | opening displacement due to swelling effect |
| $\delta_i$ | associated displacements of $P_i$ |
| $\delta_l$, $\delta_{shear}$ | normal or shear separation of cohesive surfaces |
| $\varepsilon_{ij}$, $\boldsymbol{\varepsilon}$ | strain components and strain tensor |
| $\varepsilon_x$, $\varepsilon_y$ | normal strain in the x- or y-direction |
| $\dot{\varepsilon}_0$ | yielding strain |
| $h$ | parameter in B-K criteria |
| $\eta_i$ | associated displacements of $f_i$ |
| $\theta$ | beam rotation angle |
| $\kappa$ | curvature |
| $\lambda_y$ | extension ratio, in the y-direction |
| $\mu$ | shear modulus |
| $\mu_{12}$ | shear modulus 1-2 plane |
| $\mu_f$ | Coefficient of friction |
| $\mu_0$ | initial shear modulus for hyper-elastic material |
| $\nu$ | Poison's ratio |
| $\nu_{12}$, $\nu_{23}$, $\nu_{13}$ | Poison's ratio in orthotropic elastic materials |
| $\rho$ | density |
| $\sigma_{ij}$, $\boldsymbol{\sigma}$ | stress components and strain tensor |
| $\bar{\sigma}_{ij}$ | reference stresses in damage material models |
| $\sigma_x$, $\sigma_y$ | normal stress in the x- or y-direction |
| $\sigma_0$ | yielding stress |
| $\sigma_{11}^{sw}$, $\sigma_{12}^{sw}$ | normal or shear stress incurred by swelling effect |
| $\sigma_{12}^{f}$ | shear stress incurred by friction |
| $\tau$ | shear stress |
| $\psi(x)$ | rotation angle |

# Chapter 1 Introduction

## 1.1 Background

Composite materials are engineered materials consisting of two or more constituents which have significantly different physical or chemical properties and remain separate and distinct on a macroscopic level in the finished structure. In the past several decades, composite materials have spread nearly everywhere in daily life. For example, all electrical appliances contain a circuit board that generally uses composite materials as substrate to mechanically support the electronic components, furniture and wall of dwelling houses are made of a common composite, wood fiberboard.

The constituents of composite materials could be divided into matrix and reinforcement. The reinforcements usually have special mechanical and physical properties, but are too small in size and lack of integrity. The matrix material serves as a support to hold the reinforcement materials together and a media to transfer load among individual reinforcement. Integration of matrix and reinforcements generates a new material that has properties unachievable by each constituent.

Fiber-reinforced composite materials (fiber composites for short) are the most commonly used, high performance composite materials, and generally contain continuous fiber as reinforcement and polymer as matrix. One of its applications is in the aeronautic and aerospace industries as a light, stiff and high-strength structural material to replace metallic alloys. The portion of fiber composites in the next generation of Boeing

passenger aircraft is expected to rise up to 50%. The major structural parts, such as the fuselage sections (main body of a plane) and wings, will be made of carbon fiber composites. In combat jets, the portion of composite materials is even higher. For example, composites weigh more than half of the total weight in contemporary EuroFighters [1].

Fiber composites often constitute a layered or laminated structure, with the fundamental unit being a unidirectional fiber layer (laminar). Unidirectional fiber layers could be arranged in different directions in fiber composites thus giving a lot of flexibility to build laminate with desirable mechanical properties. However, due to its special laminated structure, the failure mechanism of fiber composites is different from metallic materials. Shocks, low velocity impact or cyclic stress loading can cause fiber composites to separate at the interface between two layers, which is a failure mode known as delamination. Failure by delamination is hard to inspect from the surface since it is embedded within the fiber composites, much like fatigue in metals. Its effects on structure, however, are detrimental, including a dramatic loss in strength and effective service lifetime, making it a big safety concern. As a result, there is an imperative demand for thorough understanding of the delamination mechanism and generation of reliable means to predict the delamination occurrence and growth that lead to the final structural failure.

The study of delamination is beyond the scope of composites mechanics. Instead, as a type of crack, delamination is commonly studied in the context of fracture mechanics, which is a subject using analytical or numerical methods to calculate the driving force for crack growth and experimental methods to determine the critical driving force value as a

characteristic of material's resistance to fracture. The definition of driving force is not unique. For example the energy release rate, the stress intensity factor, and the *J*-integral all can serve as the driving force, but each has its limitation and restriction in applications. Among those, the energy release rate has been chosen as a suitable and adequate driving force for delamination in fiber composites. Consequently, the study of delamination usually is concerned about the characterization of delamination resistance in fiber composites by its critical energy release rate, and the prediction of delamination based on the driving force for delamination growth and composites' resistance to delamination.

## 1.2 Aims and scope

Aims and scope of thesis are illustrated in Figure 1.1. The ultimate goal of this study is to develop analytical and numerical methods to simulate the delamination development in fiber composites. The simulation will provide information such as the critical load to initiate delamination, the speed and extent of delamination crack growth and the impact of delamination on the strength, stiffness and serviceability of the components made of fiber composites. The information could facilitate the design of composite structures for preventing the initiation or suppressing the propagation of delamination, thereby offering reliable and safe fiber composite structures.

The accuracy of simulation results also depends on the input information on composites' properties, without which any simulation result is in vain. The most important parameter for delamination is obviously, as mentioned above, the critical energy release rate. Therefore, the measurement of the critical energy release rate, through appropriate testing methods, is another goal that this study should achieve. There are three basic fracture modes for delamination in fiber composites, i.e. the opening mode

(mode I), the shearing mode (mode II) and the tearing mode (mode III). The value of the critical energy release rate in each mode is generally different. The double cantilever beam (DCB) test, as shown in Figure 1.2(a), had been standardized by American Society for Testing and Materials (ASTM) [2] as the test method for mode I delamination toughness. The mixed mode bending (MMB) [3] test (see Figure 1.2(b)) has also been standardized for measuring the critical energy release rate of mixed mode I and II delamination. For pure mode II delamination, there are several mode II testing methods currently being considered, including the end-notched flexure (ENF) test (Figure 1.2(c)), the end-loaded split (ELS) test (Figure 1.2(d)) and the 4-point bending ENF (4ENF) test (Figure 1.2(e)). However, none of them has been accepted as the standard testing method due to some technical issues like unstable crack growth. The study on the mode III delamination has been very few, because this mode is not as common as mode I and II in real applications of fiber composites. Therefore, the part of this thesis on the critical energy release rate mainly focuses on pure mode II delamination.

The critical energy release rate is not a directly measurable term. It has to be derived from other variables that can be measured experimentally, such as crack length, force and displacement. Therefore, data reduction methods, usually based on analytical approach or finite element method (FEM), are needed to correlate the measurable quantities with the critical energy release rate of interest. This procedure, together with the development of testing methods for delamination, is known as characterization of delamination, which is the topic of the first part of thesis.

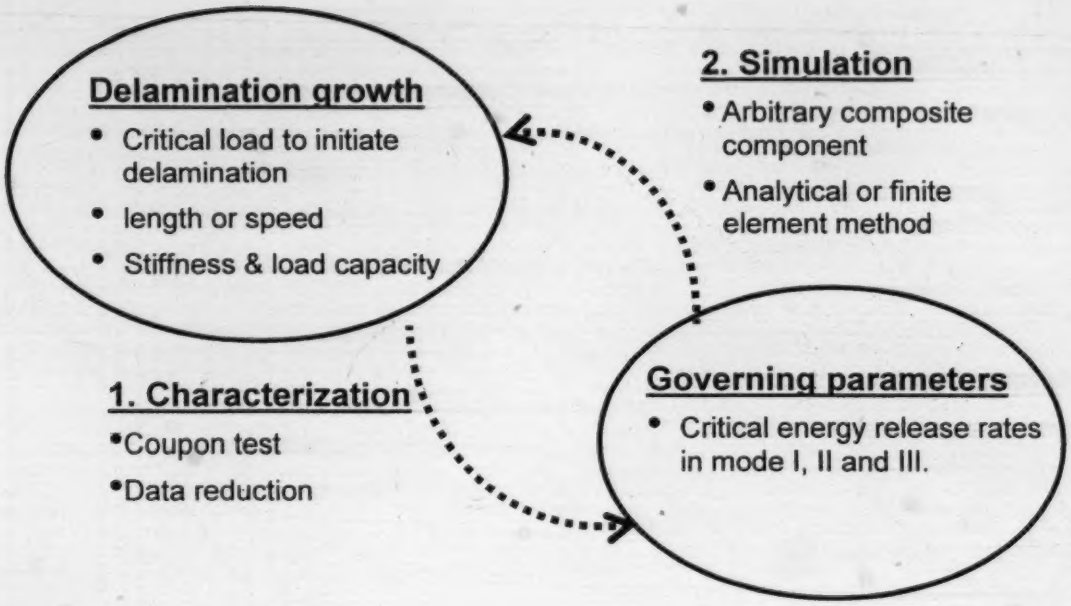
Delamination growth
• Critical load to initiate delamination
• length or speed
• Stiffness & load capacity
2. Simulation
• Arbitrary composite component
• Analytical or finite element method
Governing parameters
• Critical energy release rates in mode I, II and III.
1. Characterization
•Coupon test
•Data reduction

Figure 1.1 Scope of the thesis.

In the 2nd part of thesis, analytical approaches and FEM will be used to predict delamination in fiber composites for its initiation and propagation based on the critical energy release rates. This procedure, as shown in Figure 1.1, is the simulation of delamination. Great efforts have been devoted to simulate delamination using FEM. However, previous work either lacked of physically meaningful criteria for delamination development, missing some important stress components in determining the delamination onset, or involved applying inappropriate fracture mode in the mixed mode fracture scenarios. The FEM work presented in this thesis will be based on a different strategy to model delamination to address all of the above problems.

Overall, a framework is established in thesis to assess the resistance of fiber composites to delamination and to predict its occurrence and potential hazard before the failure happens in the application.

## 1.3 Structure of thesis

The first part of thesis is concerned with the characterization of delamination, comprising of

- Chapter 2, discussing the analytical approaches to prediction of the energy release rate which is used in Chapter 4 for the data reduction of the critical energy release rate;
- Chapter 3, introducing a new finite-element-based approach to predict the energy release rate which provides crosscheck of the analytical approaches in Chapter 2 and can also be used in the scenarios where the analytical approaches are not available; and
- Chapter 4, developing a new mode II testing method and the associated critical energy release rate reduction strategies based on the work in Chapters 2 and 3.

The second part of this thesis is concerned with the simulation of delamination, which consists of

- Chapter 5, introducing analytical methods to predict the delamination length and location, results from which are compared with experimental results; and
- Chapter 6, discussing the FEM work for the simulation of delamination, which is verified by the examples used in Chapters 2-4.

Each of Chapter 2 to 6 also contains necessary introduction and literature review regarding the main topic of that chapter.

The last chapter summarizes the whole work and identifies problems that could be considered for the future work.

mode I
DCB

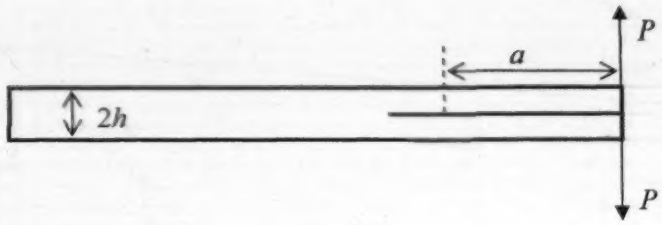


(a)

mixed mode I-
mode II, MMB

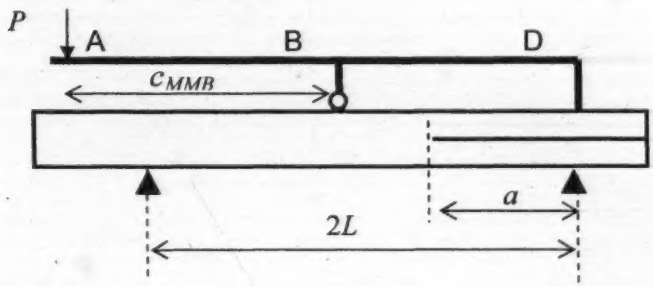


(b)

**mode II**
**ELS**

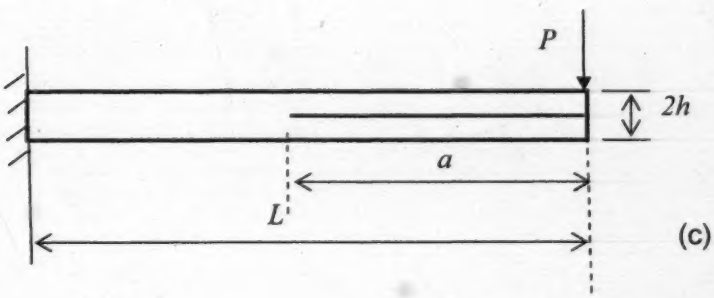


(c)

**mode II**
**ENF**

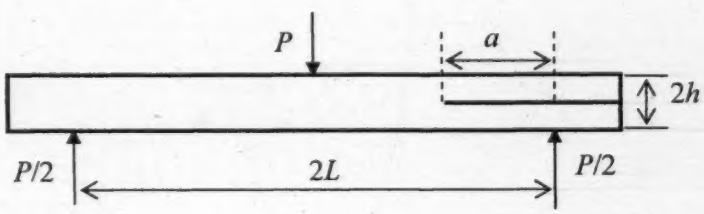


(d)

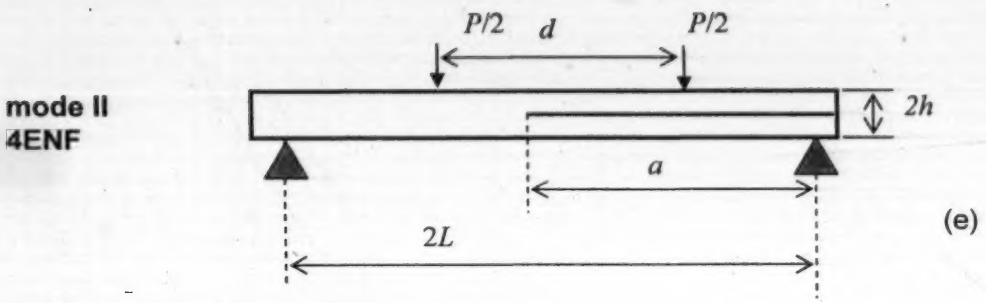


Figure 1.2 Configurations of the DCB, MMB, ENF, ELS and 4ENF tests.

# Chapter 2 Analytical Methods for the Calculation Energy Release Rate

## 2.1 Introduction

The calculation of the energy release rate is one essential step in the study of delamination. In a delamination test for the toughness measurement, the calculated energy release rate based on the experimentally determined critical loading conditions serves as the delamination resistance. In the simulation of delamination, the calculated energy release rate is compared with the delamination toughness to decide whether crack stays or advances. A closed-form expression of the energy release rate, which expresses the role of each parameter on the delamination development, is always the favorite solution. Although the closed-form solution is commonly derived based on beam or plate theories, taking advantage of the beam or plate structure of fiber composites, it is not available for most of practical composite components, let alone the analytical solutions by theory of elasticity. The difficulties may come from the irregular crack profile and complex boundary conditions. Only in the cases with simple geometry and boundary conditions, such as coupon tests for measuring delamination toughness, are the closed-form solutions possibly obtained.

A commonly used approach to derive the energy release rate is the compliance method, which is based on an equation in linear elastic fracture mechanics to correlate the derivative of compliance with respect to the crack length to the energy release rate. When

applying compliance method to fiber composites, the expressions of the compliance are often obtained using beam or plate theories that have been well established centuries ago. Even so, some concepts in the beam theories were still misused in recent literature, such as Refs. [4-6], which led to erroneous conclusions on the energy release rate of fiber composites. Thus, the following section of this chapter will briefly review the beam and plate theories and point out the errors in the literature. Some case studies of delamination growth in beams and plates will also be given.

Another analytical approach for the energy release rate is the crack tip element (CTE) analysis. The CTE analysis was invented by Schapery and Davidson [7], based on Irwin's virtual crack closure method and plate theory. The CTE analysis calculates the energy release rate from the forces and moments, incurred by stress concentration at the crack tip. In some cases, the CTE analysis could significantly simplify the procedure of deriving the energy release rate. In section 2.3, the formula of the CTE analysis will be re-derived in a clean matrix form. The CTE analysis will also be used to evaluate the frictional force effect in mode II delamination tests.

## 2.2 Compliance method

Denoted by $G$, the energy release rate in quasi-static fracture is defined as

$$GdA = dW - dU \tag{2.1}$$

where $dW$ is the external input energy, $dU$ the change of strain energy and $dA$ the change of crack area.

In linear elastic fracture mechanics, Eq. (2.1) could be rewritten as the product of the applied force $P$ and the derivative of compliance $C$ with respect to the crack area $A$:

$$G = \frac{P^2}{2}\frac{dC}{dA} \qquad (2.2)$$

The approach of using Eq. (2.2) to derive the energy release rate is known as compliance method. To use this method, the compliance has to be well-defined, i.e. only a single concentrated force or displacement is allowed to apply to a linear elastic system.

The key-point of using the compliance method is to obtain the expression of $C$ as a function of $A$. Sections 2.2.1 and 2.2.2 will focus on deriving the compliance in beam and plate structures, respectively, which contain a crack.

### 2.2.1 The energy release rate in cracked beams

#### 2.2.1.1 Euler-Bernoulli beam theory

*Basic assumptions*

Euler-Bernoulli beam theory has five assumptions that are applicable to most beams. They are:

1. The beam is long and slender, i.e. the length is much greater than the width and thickness;
2. Deformation remains small;
3. Cross-sections of the beam remain plane;
4. The beam cross-sections remain perpendicular to the neutral axis after deformation;
5. The beam is made of isotropic, linear elastic material.

*Geometric equations*

Let $x$ and $z$ denote the locations along and perpendicular to the beam axis (see Figure 2.1). Based on assumptions 2-4 above the displacement in the axial direction $u$ and that normal to the beam axis $w$ could be expressed as

$$\begin{cases} u(x,z) = u_0(x) - z\psi(x) \\ w(x,z) = w_0(x) \end{cases} \tag{2.3}$$

where $u_0(x)$ and $w_0(x)$ are the displacements on the neutral axis in the $x$- and $z$-directions, respectively, and $\psi(x)$ the rotation angle of the cross-section. From assumptions 2 and 4, the rotation angle $\psi(x)$ equals the slope of the deflection curve $w_0(x)$, thus,

$$\psi(x) = \frac{dw_0(x)}{dx} \tag{2.4a}$$

and the curvature of the deflection curve $\kappa$ is the first order derivative of $\psi(x)$:

$$\kappa(x) = \frac{d\psi(x)}{dx} \tag{2.5}$$

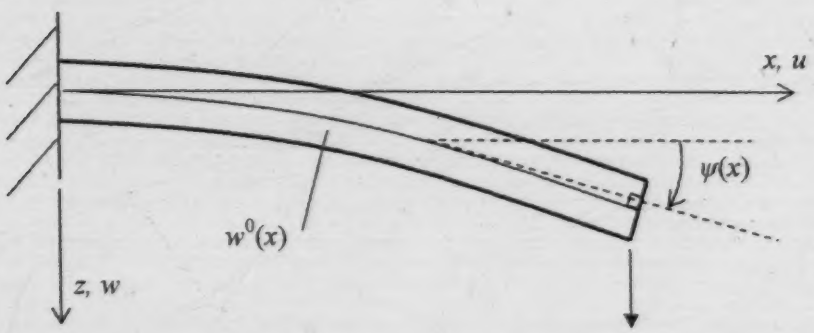


Figure 2.1 Sign conventions for displacements and rotation angle

*Constitutive equations*

From assumption 5, the bending moment $M(x)$ and the resultant axial force $N(x)$ on the cross-section are related to the curvature and axial strain, respectively, by

$$\kappa(x) = -\frac{M(x)}{EI} \tag{2.6}$$

$$\frac{du(x)}{dx} = \frac{N(x)}{EA} \tag{2.7}$$

where $E$ is elastic modulus of the beam, $I$ area moment of inertia, and $A$ cross-sectional area. The sign convention for $M$ is shown in Figure 2.2 and that for $N$ follows that $N$ is positive when it produces tension.

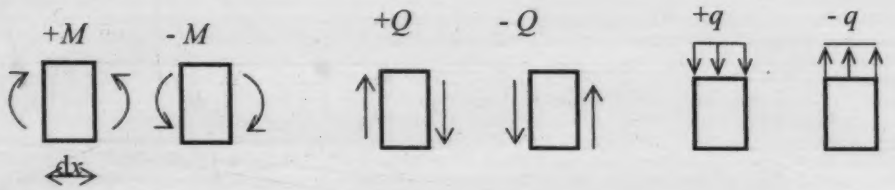


Figure 2.2 Sign conventions for bending moment $M$, shear force $Q$, and distributed shear force $q$ on an beam element.

*Equilibrium*

Equilibrium is from the free body diagram of an element of a beam shown in Figure 2.3:

$$\frac{dM}{dx} = Q \tag{2.8}$$

$$\frac{dQ}{dx} = -q \tag{2.9}$$

where $Q$ and $q$ are resultant shear force on the cross-section and the distributed transverse force, respectively, with the sign conventions depicted in Figure 2.2.

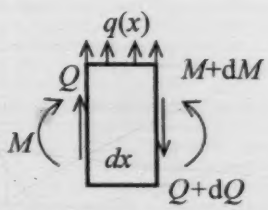


Figure 2.3 Free body diagram of a beam element for equilibrium.

Combining Eqs. (2.4-2.9), the following forms of governing equations yield for the Euler-Bernoulli beam,

$$EIw_0'' = -M \quad \text{or} \quad EIw_0''' = -Q \quad \text{or} \quad EIw_0'''' = -q \tag{2.10a, b, c}$$

$$EAu' = N \tag{2.11}$$

where the prime denotes the derivative with respect to $x$. Using Eq. (2.10) together with boundary conditions, the deflection curve of the beam can be obtained.

2.2.1.2 Timoshenko beam theory

The major improvement of the Timoshenko beam theory over the Euler-Bernoulli beam theory is that the former considers shear strain. That is, the 4th assumption of the Euler-Bernoulli beam is not required in the Timoshenko beam theory, and neither is Eq. (2.4a). In a Timoshenko beam, as shown in Figure 2.4, the slope of the deflection curve is the combination of the rotation angle $\psi$ and the shear strain $\gamma$,

$$\frac{dw_0(x)}{dx} = \gamma + \psi(x) \tag{2.4b}$$

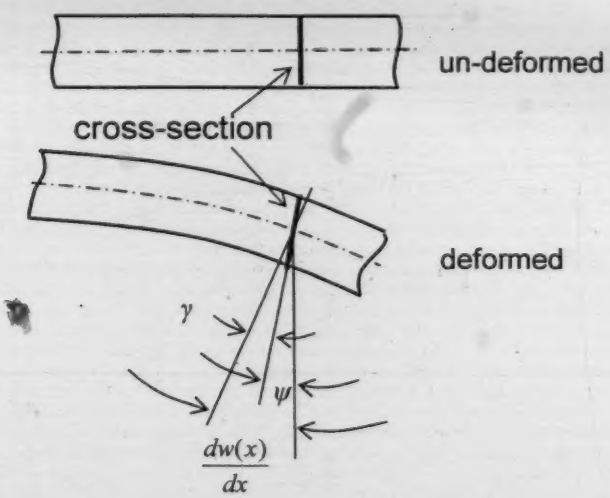


Figure 2.4 Illustration of the deformation in a Timoshenko beam.

The equilibrium and constitutive equations of the Timoshenko beam theory are exactly the same as those of the Euler-Bernoulli beam theory. Using Eqs. (2.4b) and (2.5-2.9), the differential equations for the Timoshenko beam are obtained:

$$EI(w'-\gamma)' = -M \quad \text{or} \quad EI(w'-\gamma)'' = -Q \quad \text{or} \quad EI(w'-\gamma)''' = -q \qquad \text{(2.10d, e, f)}$$

Another constitutive equation introduced to the Timoshenko beam theory is to relate $\gamma$ to the shear force $Q$ and the shear modulus $\mu$ by

$$\gamma = \frac{1}{k_{sh}} \frac{Q}{\mu A} \qquad (2.12)$$

where $k_{sh}$ is a correction factor taking into account the non-uniformly distributed shear stress. The value $k$ is generally determined by

$$\frac{1}{2}\int_A \frac{\tau^2}{\mu} dA = \frac{1}{2} Q\gamma \qquad (2.13)$$

where $\tau$ denotes the shear stress. The left hand side of Eq. (2.13) represents the strain energy due to shear force on a unit length of a beam element and the right hand side is the external work responsible for generating this amount of shear deformation. For instance, in a beam with rectangular cross-section ($h \times B$), $\tau$ can be expressed as [8],

$$\tau(z) = \frac{3}{2}\frac{Q}{A}\left(\frac{z^2}{4h^2} - 1\right) \qquad (2.14)$$

By substituting Eqs. (2.12) and (2.14) into Eq. (2.13), $k_{sh}$ is found to be 5/6.

2.2.1.3 Composite beams

Though a unidirectional fiber composite beam that has orthotropic property does not satisfy the assumption of isotropic material for the beam theory, the beam theories are still applicable if the beam axis is along one of the principal directions of the orthotropic material. In this case, the material constants $E$ and $\mu$ should be replaced by the modulus

in the corresponding directions, such as by changing $E \to E_1$ and $\mu \to \mu_{12}$ in the case that the local 1-direction of the material is along the beam axis.

The beam theories ignore the Poisson's ratio effect. When Poisson's ratio is taken into account, two types of beams could be distinguished according to the aspect ratio of width to thickness, which are referred to as narrow beams for small aspect ratio and wide beams for large aspect ratio. Considering a beam with rectangular cross-section under pure bending, as show in Figure 2.5, due to the Poisson's ratio effect, the upper half of the beam where compressive axial stress exists expands in the width direction, and the bottom half shrinks. In the case of a narrow beam the stress in the *y*-direction is free and the whole cross-section is distorted, as shown in Figure 2.5(a). But in a wide beam, which behaves more like a plate, the strain in the *y*-direction remains zero in most part of the width and only the portion near the edges is distorted. Mathematically, these two beams can be viewed as plane-stress and plane-strain models. Therefore, Young's modulus $E$ in Eqs. (2.6) and (2.10) should be modified to address the plane-strain or plane-stress condition, i.e.

$$E \to \begin{cases} \dfrac{E}{1-\nu^2} & \text{wide beam or plane - strain conditon} \\ E & \text{narrow beam or plane - stress condition} \end{cases} \tag{2.15}$$

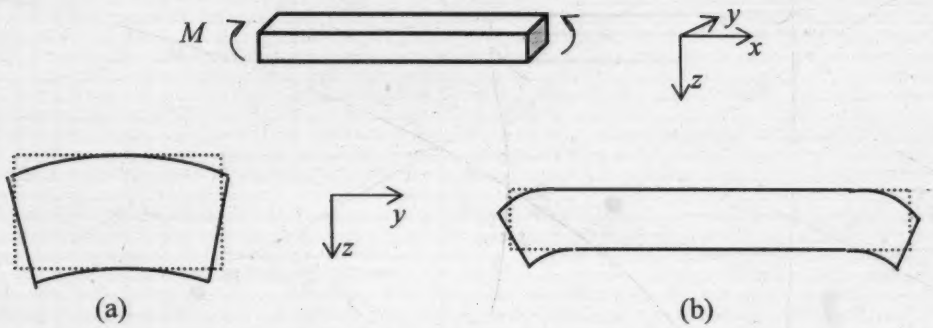


Figure 2.5 Poisson's ratio effect in (a) a narrow beam, and (b) a wide beam.

2.2.1.4 Example: a cracked beam subjected to 3-point bending.

An example of using the Timoshenko beam theory to determine the energy release rate for a crack at the mid thickness of a unidirectional fiber composite beam when subjected to 3-point bending is given below.

Assuming that the crack is not an edge crack, four possible scenarios, as illustrated in Figure 2.6, are considered here. The 1st scenario, Figure 2.6(a), has the delamination crack lying between the central loading point and one of the supports. The 2nd scenario, Figure 2.6(b), has the delamination crack extend beyond the central loading point, but lying between the two supports. The 3rd scenario, as shown in Figure 2.6(c), is similar to the 2nd scenario except that the delamination crack has extended beyond one of the supports. The 4th scenario is similar to the 1st scenario, but the crack extends over the support, as shown in Figure 2.6(d).

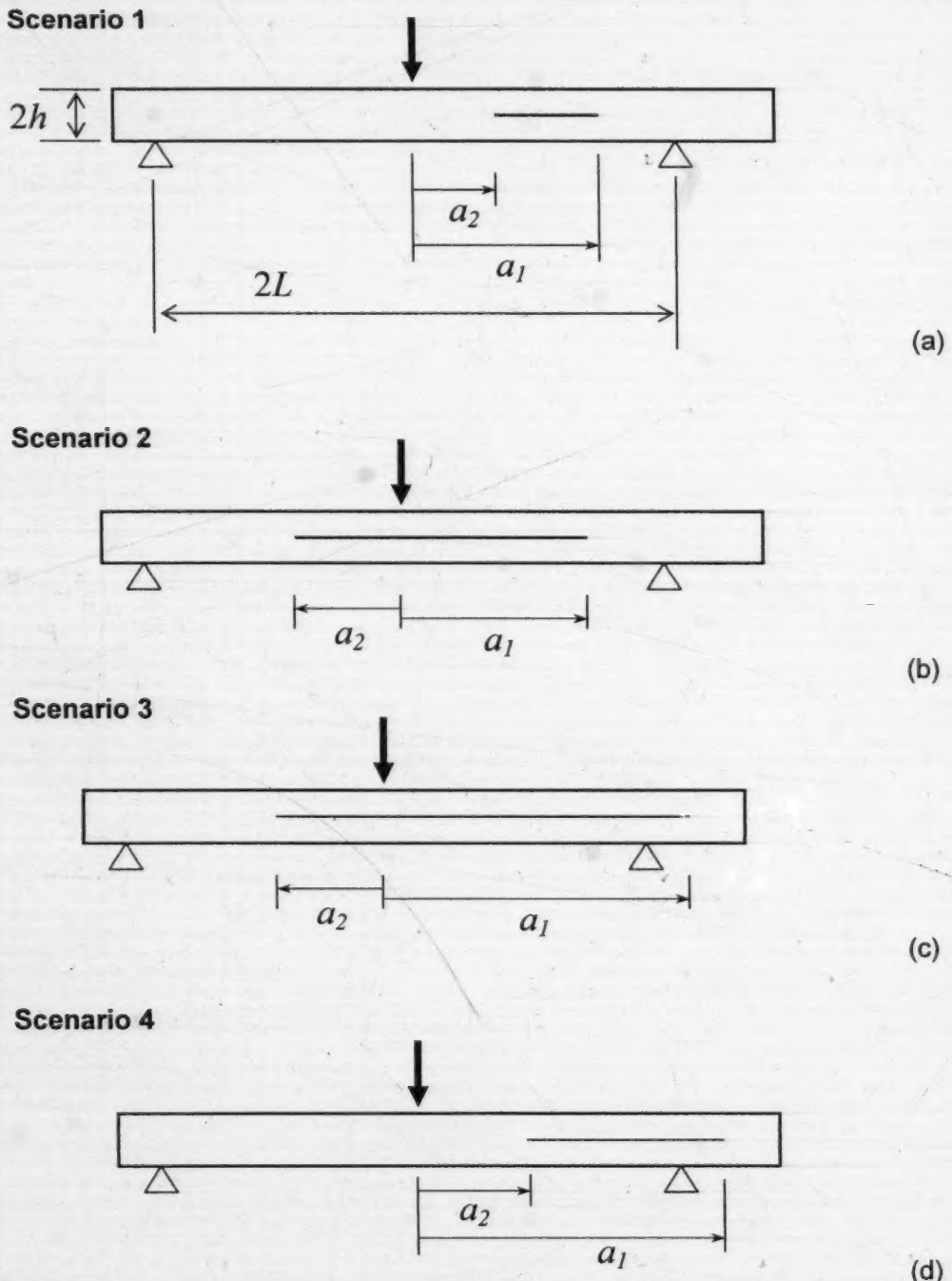


Figure 2.6 Crack configurations in a beam subjected to 3-point bending.

The scenario of Figure 2.6(a) is used to demonstrate the derivation of the expression for $G$ using the compliance method. The beam is divided into two halves, with each half carrying half of the load, as shown in Figure 2.7(a) for the top half. Free body diagram of the top half of the specimen is shown in Figure 2.7(b). According to Eq. (2.14), the internal shear stress $\tau$ on the cut boundaries is uniform and equal to $3P/(8hB)$. Two force components ($F_{C1}$ and $F_{C2}$) and two bending moments ($M_{C1}$, and $M_{C2}$) at the crack tips take into account the stress concentration. However, the moments $M_{C1}$ and $M_{C2}$ have to be equal to 0 to meet the compatibility between the 2 halves of the beam. The coordinate system for Figure 2.7(b) is set at the mid-plane of the upper half beam with the origin above the right crack tip, point O of Figure 2.7(b). Following the approach in ref. [4] for the convenience of the derivation and without losing the generality, it is assumed that the deflection and rotation angle are zero at the mid point of the upper half beam (point B), as depicted in Figure 2.7(c):

$$\begin{cases} w(-a_1) = 0 \\ \psi(-a_1) = 0 \\ u(-a_1) = 0 \end{cases} \tag{2.16}$$

Using the governing equation Eq. (2.10d) and the above boundary conditions, the deflection, $w(x)$, and rotational angle, $\psi(x)$, in section AC of Figure 2.7(b) is obtained,

$$w(x) = \frac{P(3L - x - a_1)(x + a_1)^2}{8h^3 BE} + \frac{P|x + a_1|}{4hB\mu} \tag{2.17}$$

$$\psi(x) = \frac{(x + a_1)[2L - (x + a_1)]}{8h^3 BE} \tag{2.18}$$

Substituting $x = (a_2 - a_1)$ to above equations, $w$ and $\psi$ at point C in Figure 2.7(b) can be expressed as:

$$w(a_2 - a_1) = \frac{P(3L - a_2)a_2^{\,2}}{8h^3 BE} - \frac{Pa_2}{4hB\mu} \tag{2.19}$$

$$\psi(a_2 - a_1) = \frac{a_2(2L - a_2)}{8h^3 BE} \tag{2.20}$$

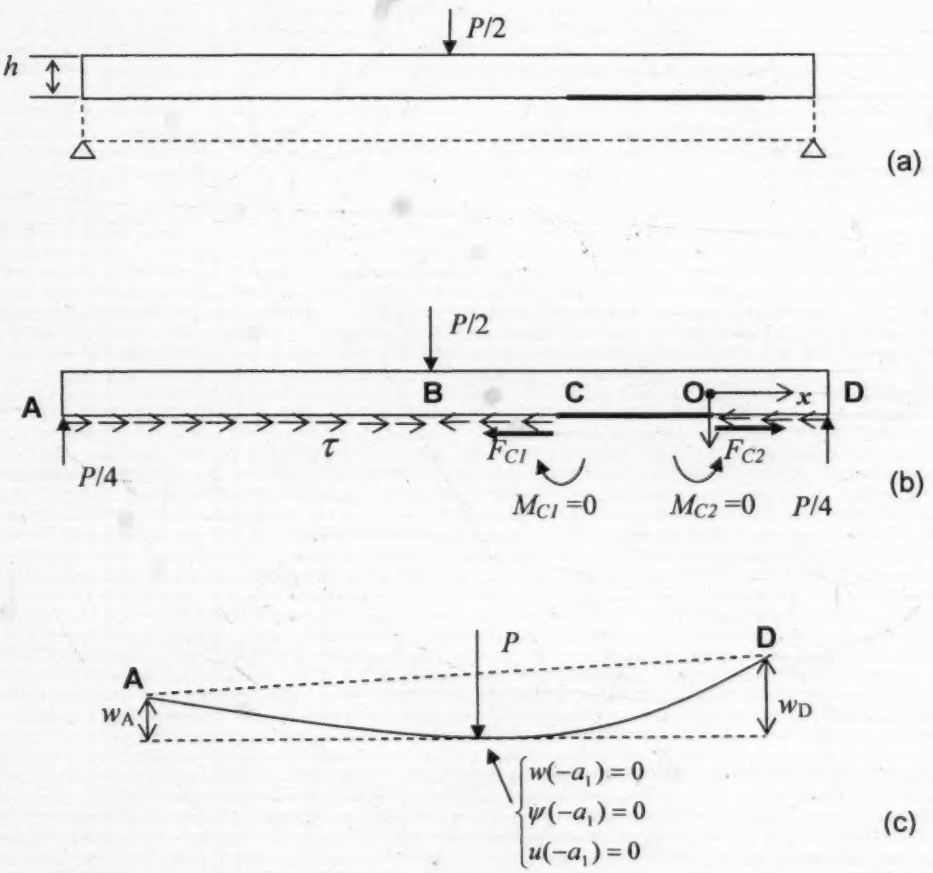


Figure 2.7 Diagrams for beam analysis: (a) upper beam model; (b) free body diagram of the upper beam; and (c) boundary conditions.

To obtain the deflection curve of part CO in Figure 2.7(b), the following compatibility equation is introduced due to the unknown concentrated forces $F_{C1}$ and $F_{C2}$ at the crack tips,

$$u(0,h/2)=u(a_2-a_1,h/2) \tag{2.21}$$

This equation states that the length CO in Figure 2.7(b) remains constant during the deflection, as elongation of CO in the top half should be compatible with the counterpart in the bottom half.

Again, by solving ordinary differential equations together with boundary conditions of $w$ and $\psi$ at point C (Eqs. (2.19) and (2.20)) and compatibility condition (Eq. 2.21), $F_{C1}$ and $F_{C2}$ were obtained as:

$$F_{C1}=F_{C2}=\frac{3P}{16Bh}(a_1-a_2) \tag{2.22}$$

Similarly, $w$ and $\psi$ in section OD are:

$$w(x)=\frac{P[2x^3+6(a_1-L)x^2+6(a_1^2-2a_1L)x-a_1^3+9a_1^2a_2-9a_1a_2^2-6a_1^2L+3a_2^3]}{16EBh^3}+\frac{P(x+a_1)}{4\mu Bh} \tag{2.23}$$

$$\psi(x)=\frac{3P(x+a_1)[2L-(x+a_1)]}{8EBh^3} \tag{2.24}$$

Eqs. (2.17) and (2.23) describe the deflection of the beam in Scenario 1 of Figure 2.16, and provide the information needed to determine compliance of the beam.

Following the same procedure, expressions of the deflection curve for the other scenarios of Figure 2.6 were derived. Thus, expressions for compliance $C$ were obtained and listed in Eq. (2.25).

For the 1st scenario, Figure 2.6(a), the expression for $C$ is:

$$C=\frac{L^3}{4h^3BE}+\frac{L}{4hB\mu}+\frac{3(a_1-a_2)^3}{32h^3BE} \tag{2.25a}$$

for the 2nd scenario, Figure 2.6(b)

$$C = \frac{L^3}{4h^3BE} + \frac{L}{4hB\mu} + \frac{3(a_1+a_2)^4 - 36a_1^2a_2^2}{32h^3BE(a_1+a_2)} \tag{2.25b}$$

for the 3rd scenario, Figure 2.6(c)

$$C = \frac{L^3}{4h^3BE} + \frac{L}{4hB\mu} + \frac{3\left[-3L^4 + 4a_1L^3 + 8a_2L^3 + 6a_2^2L^2 + 12a_1a_2L^2 - 12a_1a_2^2L + 4a_1a_2^3 + a_2^4\right]}{32h^3BE(a_1+a_2)} \tag{2.25c}$$

and for the 4th scenario, Figure 2.6(d)

$$C = \frac{L^3}{4h^3E} + \frac{L}{4h\mu} + \frac{3\left[-3L^4 + 4a_1L^3 + 8a_2L^3 - 6a_2^2L^2 - 12a_1a_2L^2 + 12a_1a_2^2L - 4a_1a_2^3 + a_2^4\right]}{32h^3BE(a_1-a_2)} \tag{2.25d}$$

The expressions for $G$ were obtained by substituting the above expressions for $C$ into Eq. (2.2), which are:

for the 1st scenario, Figure 2.6(a),

$$G_{a1} = G_{a2} = \frac{9P^2}{64EB^2h^3}(a_1 - a_2)^2 \tag{2.26}$$

for the 2nd scenario, Figure 2.6(b)

$$G_{a1} = \frac{9P^2}{64EB^2h^3(a_1+a_2)^2}(a_1^2 - a_2^2 + 2a_1a_2)^2 \tag{2.27}$$

$$G_{a2} = \frac{9P^2}{64EB^2h^3(a_1+a_2)^2}(a_1^2 - a_2^2 - 2a_1a_2)^2 \tag{2.28}$$

for the 3rd scenario, Figure 2.6(c)

$$G_{a1} = \frac{9P^2}{64EB^2h^3(a_1+a_2)^2}(a_2^2 - 2a_2L - L^2)^2 \tag{2.29}$$

$$G_{a2} = \frac{9P^2}{64EB^2h^3(a_1+a_2)^2}(a_2^2 + L^2 - 2a_1L + 2a_1a_2)^2 \tag{2.30}$$

and for the 4th scenario, Figure 2.6(d)

$$G_{a1} = \frac{9P^2}{64EB^2h^3(a_1 - a_2)^2}(a_2^2 - 2a_2L + L^2)^2 \tag{2.31}$$

$$G_{a2} = \frac{9P^2}{64EB^2h^3(a_1 + a_2)^2}(-a_2^2 + L^2 - 2a_1L + 2a_1a_2)^2 \tag{2.32}$$

Each of the above $G$ expressions represents the energy release rate for the increase of crack length in the direction that is designated by the subscript ($a_1$ or $a_2$).

2.2.1.5 Shear deformation effect

Shear flexibility was suspected to be a factor that influences the determination of $G$. Some researchers gave equations to quantify this effect, including the work by Carlson et al. [4], Zhou et al. [5] and Corleto et al. [6]. However, in the above example of cracked beam the shear modulus does not appear in the expressions of $G$, Eqs. (2.26-2.32), though the shear deformation was considered in the derivation. The expressions of compliance, Eqs. (2.25a-2.25d), however contain the term for the shear deformation, but show independence of the crack length. Thus, these terms vanish when taking derivative with respect to the crack length.

Following the same procedure used in the previous example, the expressions of $C$ and $G$ of the common mode II delamination tests, i.e. the ENF test, the ELS test and the 4ENF test, were derived and listed in the following.

For the ENF tests (Figure 1.2(d)),

$$C^{ENF} = \frac{2L^3 + 3a^3}{8h^3BE_1} + \frac{3L}{10hB\mu} \tag{2.33}$$

$$G^{ENF} = \frac{9P^2a^2}{16E_1h^3B^2} \tag{2.34}$$

for the ELS test (Figure 1.2(c))

$$C^{ELS} = \frac{L^3 + 3a^3}{2h^3 BE_1} + \frac{3L}{10hB\mu} \tag{2.35}$$

$$G^{ELS} = \frac{9P^2 a^2}{4h^3 B^2 E_1} \tag{2.36}$$

and for the 4ENF test (Figure 1.2(e))

$$C^{4ENF} = \frac{9(L-d/2)^2 a}{8h^3 BE_1} + \frac{(L-d/2)^2[3L-5(L-d/2)]}{4h^3 BE_1} + \frac{3(L-d/2)}{10Bh\mu} \tag{2.37}$$

$$G^{4ENF} = \frac{9P^2(L-d/2)^2}{16h^3 B^2 E_1} \tag{2.38}$$

All results show the independence of $G$ from the shear modulus. However, Refs. [4-6] concluded that shear modulus affects the $G$ value, which was actually caused by an erroneous assumption in the derivation that created an unnecessary term in the expression of $G$ related to the shear modulus. The erroneous assumption is that the shear strain in the un-cracked section of a beam introduces rotation of the adjacent cracked section, thus generating extra terms in $G$. The schematic description of the deformation with shear strain is illustrated in Figure 2.8 which shows that the shear strain $\gamma$ does not cause any rotation of the cross-section. The rotation at the end is entirely due to the bending deformation.

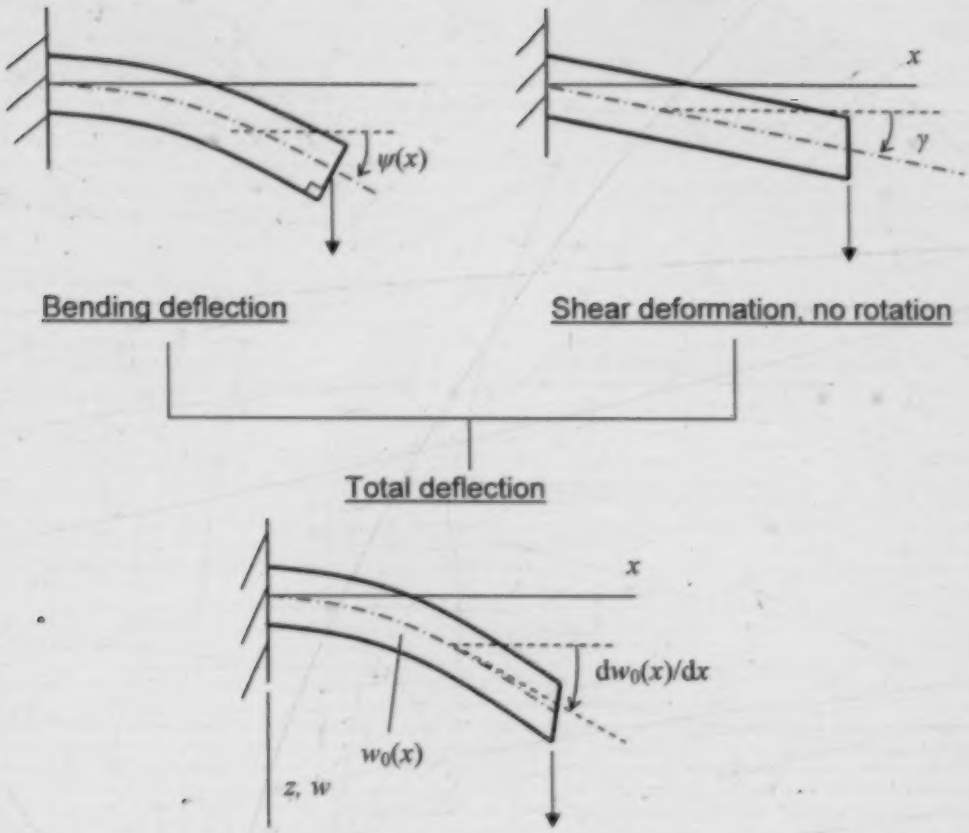


Figure 2.8 Deformation mechanism of a beam with shear force.

### 2.2.2 Energy release rate in cracked plates

2.2.2.1 Plate theory

The classical plate theory is a 3D version of beam theory, and is established based on similar assumptions:

1. The plate is thin, i.e. in plane dimensions are much greater than the thickness;

2. Deformation remains small;

3. Material is isotropic and linear elastic;

4. A straight line normal to the mid-plane remains the same length after the deformation and is still normal to the mid plane (Kirchoff's hypothesis).

Based on the above assumptions, the displacements $u$, $v$ and $w$ could be expressed as

$$\begin{cases} w = w(x,y) \\ u = u_0(x,y) - zw_{,x} \\ v = v_0(x,y) - zw_{,y} \end{cases} \tag{2.39}$$

The kinematics, constitutive, force resultant, and equilibrium equations of the classical plate theory are summarized here.

*Kinematics*

$$\begin{pmatrix} \varepsilon_{xx} \\ \varepsilon_{yy} \\ \gamma_{xy} \end{pmatrix} = z \begin{pmatrix} -w_{,xx} \\ -w_{,yy} \\ -2w_{,xy} \end{pmatrix} = z \begin{pmatrix} \kappa_x \\ \kappa_y \\ 2\kappa_{xy} \end{pmatrix} \tag{2.40}$$

*Resultants*

$$\begin{pmatrix} M_x \\ M_y \\ M_{xy} \end{pmatrix} = \int_h^h z \begin{pmatrix} \sigma_x \\ \sigma_y \\ \sigma_{xy} \end{pmatrix} dz \tag{2.41a}$$

$$\begin{pmatrix} Q_{xz} \\ Q_{yz} \end{pmatrix} = \int_h^h \begin{pmatrix} \sigma_{xz} \\ \sigma_{yz} \end{pmatrix} dz \tag{2.41b}$$

*Constitutive equations*

$$\begin{pmatrix} \varepsilon_{xx} \\ \varepsilon_{yy} \\ \gamma_{xy} \end{pmatrix} = \frac{1}{E} \begin{bmatrix} 1 & -\nu & 0 \\ -\nu & 1 & 0 \\ 0 & 0 & 2(1+\nu) \end{bmatrix} \begin{pmatrix} \sigma_x \\ \sigma_y \\ \sigma_{xy} \end{pmatrix} \tag{2.42}$$

*Equilibrium*

$$Q_{xz} = \frac{\partial M_x}{\partial x} + \frac{\partial M_{xy}}{\partial y}$$
$$Q_{yz} = \frac{\partial M_y}{\partial y} + \frac{\partial M_{xy}}{\partial x} \qquad (2.43)$$
$$\frac{\partial Q_{xy}}{\partial x} + \frac{\partial Q_{xy}}{\partial y} = -qz$$

The governing differential equation of the deflection $w$ can be obtained by the combination of Equations (2.39-2.43) with Hooke's law, that is,

$$\nabla^2(D\nabla^2 w) = q \qquad (2.44)$$

where $q$ is the distributed load acting along the plate normal, $\nabla^2$ is the Laplacian differential operator which equals to $\frac{\partial^2}{\partial x^2} + \frac{\partial^2}{\partial y^2}$ in a Cartesian coordinate system and $D$ is the bending rigidity.

2.2.2.2 Example: penny-shaped crack in a plate

This section presents the derivation of the energy release rate in a plate structure shown in Figure 2.9. The plate contains a penny-shaped crack in the mid-thickness and is simply supported along a circumference of radius $R$ with concentrated force $P$ at the center of the top surface.

First two basic solutions of circular plates without any crack but subjected to a force loading at the center are presented, one with simply supported and the other with clamped boundary conditions.

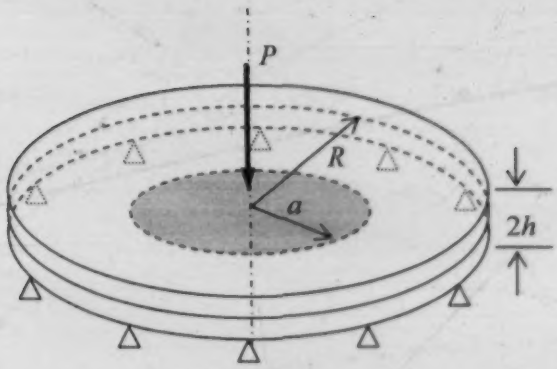


Figure 2.9 Penny-shaped crack embedded in a plate.

A cylindrical coordinate system is set at the center of the circular plate. Since it is an axisymmetrical problem, all derivatives with respect to $\theta$ are zero. The governing equation (2.44) in the cylindrical system is:

$$\frac{\partial^3 w}{\partial r^3}+\frac{1}{r}\frac{\partial^2 w}{\partial r^2}-\frac{\partial w}{r^2\partial r}+\frac{V}{D}=0 \tag{2.45}$$

where $V$ is the shear force per unit length, equal to $P/(2\pi r)$, and $D$ is equal to

$$D=\frac{2Eh^3}{3(1-\nu^2)} \tag{2.46}$$

The bending moments in $r$ and $\theta$ directions are,

$$\begin{cases} M_r=-D(w_{,rr}+\nu w_{,r}/r) \\ M_\theta=-D(\nu w_{,rr}+w_{,r}/r) \end{cases} \tag{2.47}$$

The boundary conditions for simply supported circular plate are

$$\begin{cases} w|_{r=R}=0 \\ M_r|_{r=R}=0 \\ w_{,r}|_{r=0}=0 \end{cases} \tag{2.48}$$

The first boundary condition specifies zero displacement at $r = R$, the second denotes zero bending moment at $r = R$, and the last one is the symmetrical condition at the center. By solving Eq. (2.45) with the boundary conditions, we have

$$w(r) = \frac{P[(3-\nu)(R^2 - r^2) - 2(1+\nu)r^2 \ln(R/r)]}{16\pi D(1+\nu)} \tag{2.49a}$$

For the case with clamped boundary, the second equation of Eq. (2.48) should be changed to $w_{,r}|_{r=R} = 0$ to represent zero rotation on the clamped boundary. The deflection curve for this case is

$$w(r) = \frac{P[R^2 - r^2 - 2r^2 \ln(R/r)]}{16\pi D} \tag{2.49b}$$

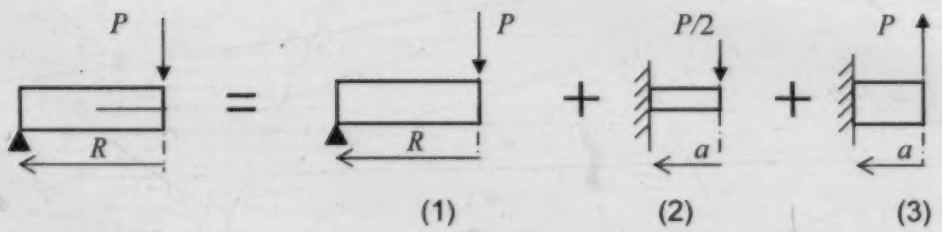


Figure 2.10 Schematic illustration of the superposition

The problem defined in Figure 2.9 could be solved by decomposing it into 3 simple sub-problems as shown in Figure 2.10. It is easy to find that the superposition of the solutions of problems (1~3) in Figure 2.10 satisfies all boundary conditions of the original problem and the three sub-problems share the same governing equation. Therefore, the summation of these three problems must be the unique solution of the cracked circular plate. Thus, the displacement at the loading point can be expressed as

$$w|_{r=0} = \frac{P}{32\pi E h^3}[9a^2(1-\nu^2) + 9R^2 - 6\nu R^2 + 3\nu^2 R^2] \tag{2.50}$$

Dividing the above equation by $P$ yields the expression of compliance $C$

$$C = \frac{9a^2(1-\nu^2)}{32\pi Eh^3} + \frac{9R^2 - 6\nu R^2 + 3\nu^2 R^2}{32\pi Eh^3} \tag{2.51}$$

Based on Eq. (2.2), note $dA = 2\pi da$ in this case, the corresponding $G$ for crack growth, is:

$$G = \frac{9P^2(1-\nu^2)}{64\pi^2 Eh^3} \tag{2.52}$$

## 2.3 Crack tip element analysis

### 2.3.1 Crack tip element theory

A brick element containing a crack tip is taken out from a delaminated laminate plate as shown in Figure 2.11(a). The width of the crack tip element is assumed to be so small that the crack front is straight and along the $y$-direction, though the entire crack front may be curved. It is also assumed that the length ($x$-direction) of this element is small, thus the forces and moments on the front and back surfaces can be ignored.

Extending from the crack, the element is divided into two parts. Three concentrated forces, $N_C$, $S_C$ and $M_C$, at the crack tip are exposed and illustrated in the free body diagram of the top part of the element, as shown in Figure 2.11(b). Based on the equilibrium, we have

$$N_C = N'_1 - N_1 \tag{2.53a}$$

$$S_C = S'_1 - S_1 \tag{2.53b}$$

$$M_C = M'_1 - M_1 - N_C t_1/2 \tag{2.53c}$$

or in the matrix form

$$\begin{pmatrix} N_1 - N'_1 \\ S_1 - S'_1 \\ M_1 - M'_1 \end{pmatrix} = [\mathbf{C}^{(1)}] \begin{pmatrix} N_C \\ S_C \\ M_C \end{pmatrix} \tag{2.54}$$

where $[\mathbf{C}^{(1)}]$ denotes a 3×3 matrix of constants.

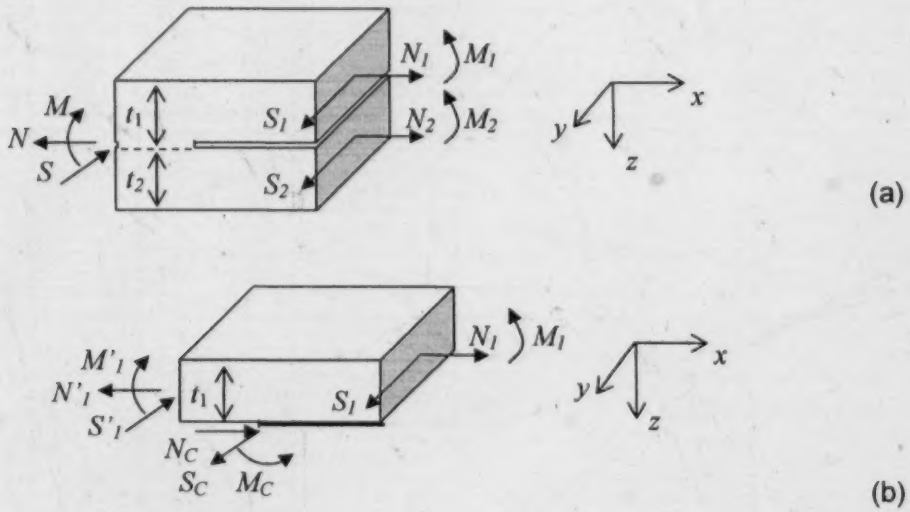


Figure 2.11 Free body diagrams for (a) crack tip element, and (b) half crack tip element

According to the laminate theory, strains $\varepsilon_x^{(1)}$ and $\gamma_{xy}^{(1)}$, and curvature $\kappa_x^{(1)}$ of the upper arm are linear functions of the external loads,

$$\begin{pmatrix} \varepsilon_x^{(1)} \\ \gamma_{xy}^{(1)} \\ \kappa_x^{(1)} \end{pmatrix} = [\mathbf{A}^{(1)}] \begin{pmatrix} N_1 \\ S_1 \\ M_1 \end{pmatrix} \quad \text{and} \quad \begin{pmatrix} \varepsilon_x'^{(1)} \\ \gamma_{xy}'^{(1)} \\ \kappa_x'^{(1)} \end{pmatrix} = [\mathbf{A}^{(1)}] \begin{pmatrix} N'_1 \\ S'_1 \\ M'_1 \end{pmatrix} \tag{2.55}$$

where, $[\mathbf{A}^{(1)}]$ is a 3×3 matrix and the variables with prime denote the quantities in the un-cracked portion.

Assuming crack advances a length $\Delta a$, according to Irwin's virtual crack closure method [9], $G$ can be calculated based on the work required to close this crack length increment. Thus,

$$G = [N_C(u_2 - u_1) + M_C(\psi_2 - \psi_1) + S_C(v_2 - v_1)]/2\Delta a \tag{2.56}$$

where $u_1$, $v_1$ and $\psi_1$ are the displacements and rotation angle of the crack front on the upper arm after the crack growth, $u_2$, $v_2$ and $\psi_2$ are for the bottom arm. $u_1$, $v_1$ and $\psi_1$ can be expressed as

$$u_1 = \Delta a[(\varepsilon_x^{(1)} + \kappa_x^{(1)} t_1/2) - (\varepsilon_x'^{(1)} + \kappa_x'^{(1)} t_1/2)] \tag{2.57a}$$

$$v_1 = \Delta a[\gamma_x^{(1)} - \gamma_x'^{(1)}] \tag{2.57b}$$

$$\psi_1 = \Delta a[\kappa_x^{(1)} - \kappa_x'^{(1)}] \tag{2.57c}$$

By rewriting Eq. (2.57) into a matrix form and using Eqs. (2.54-2.55), we have

$$\begin{pmatrix} u_1 \\ v_1 \\ \psi_1 \end{pmatrix} = \Delta a[\mathbf{B}^{(1)}] \begin{pmatrix} \varepsilon_x^{(1)} - \varepsilon_x'^{(1)} \\ \gamma_{xy}^{(1)} - \gamma_{xy}'^{(1)} \\ \kappa_x^{(1)} - \kappa_x'^{(1)} \end{pmatrix} = \Delta a[\mathbf{B}^{(1)}][\mathbf{A}^{(1)}][\mathbf{C}^{(1)}] \begin{pmatrix} N_C \\ S_C \\ M_C \end{pmatrix} \tag{2.58}$$

Similarly, $u_2$, $v_2$ and $\psi_2$ for the bottom arm can be written as,

$$\begin{pmatrix} u_2 \\ v_2 \\ \psi_2 \end{pmatrix} = \Delta a[\mathbf{B}^{(2)}][\mathbf{A}^{(2)}][\mathbf{C}^{(2)}] \begin{pmatrix} N_C \\ S_C \\ M_C \end{pmatrix} \tag{2.59}$$

Substituting Eqs. (2.58-2.59) into (2.56) gives the expression of $G$,

$$G = [([\mathbf{B}^{(2)}][\mathbf{A}^{(2)}][\mathbf{C}^{(2)}] - [\mathbf{B}^{(1)}][\mathbf{A}^{(1)}][\mathbf{C}^{(1)}])[\mathbf{N}]^T[\mathbf{N}]/2 \tag{2.60}$$

where $[\mathbf{N}] = [N_C, S_C, M_C]^T$. Eq. (2.60) indicates that $G$ can be fully determined by the concentrated forces **[N]**, material constants **[A]** and constant coefficient matrices **[B]** and **[C]**. The expressions of **[B]** and **[C]** are given as follows,

$$\mathbf{C}^{(1)} = \begin{bmatrix} -1 & 0 & 0 \\ 0 & -1 & 0 \\ -t_1/2 & 0 & -1 \end{bmatrix}, \mathbf{C}^{(2)} = \begin{bmatrix} 1 & 0 & 0 \\ 0 & 1 & 0 \\ -t_2/2 & 0 & 1 \end{bmatrix} \tag{2.61a,b}$$

$$\mathbf{B}^{(1)} = \begin{bmatrix} 1 & 0 & t_1/2 \\ 0 & 1 & 0 \\ 0 & 0 & 1 \end{bmatrix}, \qquad \mathbf{B}^{(2)} = \begin{bmatrix} 1 & 0 & -t_2/2 \\ 0 & 1 & 0 \\ 0 & 0 & 1 \end{bmatrix} \tag{2.62a,b}$$

*Example: cracked beam under bending*

The example discussed in Section 2.2.1.4, with $G$ derived using the compliance method, is re-analyzed here using the CTE analysis. As to be shown here, the CTE analysis takes much less effort for the derivation.

In the case of unidirectional composite beams, with the absence of shear force $S_C$, Eq. (2.60) could be further simplified as

$$G = (\frac{2}{E_1' t_1} + \frac{2}{E_1' t_2}) F_C^2 + (\frac{6}{E_1' t_1^3} + \frac{6}{E_1' t_2^3}) M_C^2 + (\frac{6}{E_1' t_1} - \frac{6}{E_1' t_2}) F_C M_C \tag{2.63}$$

where $E_1'$ the equivalent Young's modulus in the longitudinal direction that is equal to $E_1$ for narrow beams (plane-stress condition) and $E_1/(1-\nu_{12}\nu_{21})$ for wide beams (plane-strain condition), with $\nu_{12}$ and $\nu_{21}$ being the corresponding Poisson's ratios.

The previous analysis has shown that $F_{C1} = F_{C2} = 3P(a_1 - a_2)/(8hB)$ and $M_{C1} = M_{C2} = 0$ for Scenario 1 of Figure 2.6. Thickness for the two parts of beam is the same $h$, i.e. $t_1 = t_2 = h$. By substituting these expressions into Eq. (2.63), it gives

$$G_{a1} = G_{a2} = (\frac{4}{E_1' h}) \left[ \frac{3P(a_1 - a_2)}{16hB} \right]^2 \tag{2.64}$$

which is the same as Eq. (2.26). The same conclusion can also be found for other scenarios.

*Example: penny-shaped crack in a plate*

The free body diagram for a sector of the bottom part of a circular plate is depicted in Figure 2.12. Similar to the shear stress distribution in the mid plane of a beam (Eq. (2.14)), the shear stress $\tau(r)$ at the mid-thickness of the non-cracked portion is

$$\tau(r) = \frac{3P}{8\pi rh} \tag{2.65}$$

and the resultant force of the shear stress in the $r$-direction is

$$F_{C\tau} = \int_0^{\theta} \int_a^R \tau(r) \cdot r dr d\theta = \frac{3P\theta}{8\pi h}(R-a) \tag{2.66}$$

The normal stress has a linear variation along the thickness direction. This normal stress is zero at $z$=0 and maximum at $\pm h$. Therefore, the average normal stress in the bottom half of the plate is $\sigma_{max}/2$, where $\sigma_{max}$ is the maximum stress which can be related to the bending moment $M_\theta$ with respect to the $\theta$-axis by

$$M_\theta = \int_{-h}^{h} \frac{z^2}{h} \sigma_{max} dz = \frac{2}{3} h^2 \sigma_{max} \tag{2.67}$$

The component in the $r$-direction of this normal stress is (see Figure 2.12),

$$F_{CM} = \theta \int_0^R \sigma_{max}/2 dr = \theta \int_0^R \frac{3M_\theta}{4h^2} dr \tag{2.68}$$

The expression of $M_\theta$ for the cracked ($r > a$) or un-cracked ($r < a$) portion can be determined using Eq. (2.47). Thus, $F_C$ is obtained by equilibrium as

$$F_C = F_{C\tau} - F_{CM} = \theta \frac{3P}{16\pi h} \tag{2.69}$$

For unit length of crack, $F_C$=$3P/16\pi h$, by substituting above equation into Eq. (2.63), the same $G$ expression as Eq. (2.52) is obtained.

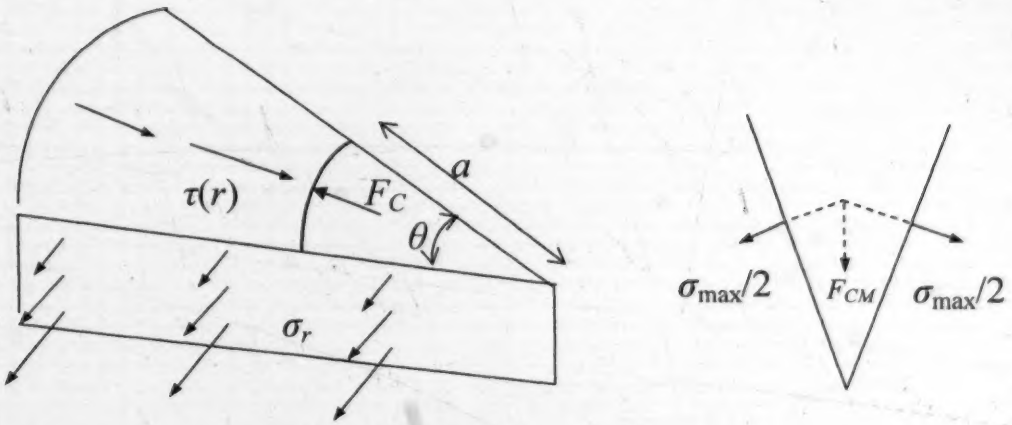


Figure 2.12 Free body diagram for determining $F_C$.

### 2.3.2 Frictional force effect on *G* in mode II delamination tests

Mode II delamination tests generally use beam-type specimens that contain an initial crack. Due to the nature of the mode II fracture, crack surfaces slide on each other during the crack growth. The compressive load on the cracked surface may generate a frictional force on the sliding surfaces. However, the $G$ expressions derived in section 2.2.1.5 ignored the effect of friction. CTE analysis is used here for explicitly quantifying the frictional force effect in the ENF, the ELS and the 4ENF tests.

A generalized free body diagram of a half beam, cut by virtually extending the initial crack, is shown in Figure 2.13. The forces, $F_C$ and $M_C$, acting on the crack surface at the crack tip are exposed, as depicted in Figure 2.13. The distributed compressive load on the cracked surface $p(x)$ generates a frictional force valued $\mu_f p(x)$, where $\mu_f$ is coefficient of friction. Due to the presence of the frictional force, $F_C$ at the crack tip is alleviated and becomes,

$$F_C = F_{C0} - \int \mu_f \cdot p(x) dA = F_{C0} - \mu_f P_C \tag{2.70}$$

where $P_C$ is the resultant of the distributed compressive load on the fracture surface, and $F_{C0}$ the concentrated force for the same external loading but with $\mu_f = 0$.

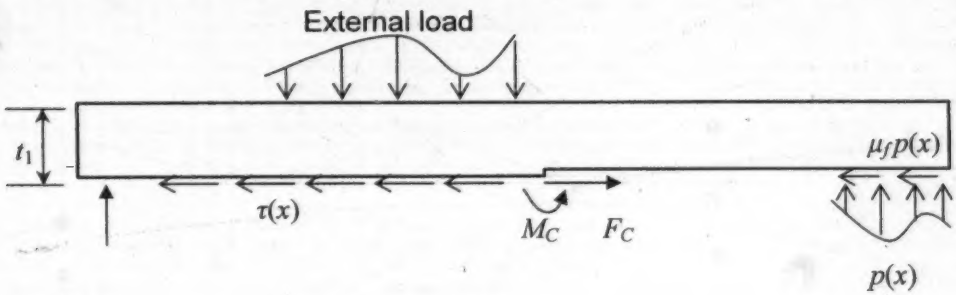


Figure 2.13 Schematic free body diagram of a half beam.

The effect of the frictional force could be evaluated using a non-dimensional parameter $e_f$, defined as

$$e_f = (G_0 - G_f)/G_0 \tag{2.71}$$

where $G_0$ is the energy release rate of the beam specimen with frictionless contact and $G_f$ the corresponding energy release rate with frictional contact under the same loading condition.

Using the special form of $G$ from CTE analysis, Eq. (2.63), and assuming $t_1 = t_2 = h$ and $M_C = 0$, $G$ can be expressed as

$$G = (2F_C)^2/(E_1'h) \tag{2.72}$$

With Eqs. (2.70) and (2.72), $e_f$ can be expressed as a 2nd order polynomial function of $f$, defined as:

$$f = \mu_f P_C / F_{C0} \tag{2.73}$$

That is,

$$e_f = \frac{(F_{C0})^2 - (F_C)^2}{(F_{C0})^2} = (2f - f^2) \times 100\% \tag{2.74}$$

Eq. (2.74) suggests that $f$ is the single parameter for quantifying the frictional force effect on the $G$ value.

According to the above analysis, the key issue to quantify the frictional force effect on the mode II delamination resistance is to determine $f$ from the corresponding $P_C$ and $F_{C0}$ values for each mode II test. Expressions of $P_C$ and $F_{C0}$ for the delamination tests can be obtained from the free body diagrams of the half beam. The ENF test is used here as an example to demonstrate how to determine the expression for $f$.

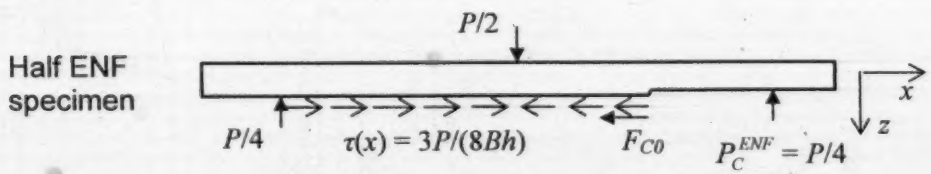


Figure 2.14 The free body diagram of upper half of an ENF specimen.

Setup of the ENF test is depicted in Figure 1.1(c) and the corresponding free body diagram for the upper half of the specimen is shown in Figure 2.14. The internal shear stress along the mid-plane of the beam, $\tau(x)$, is $3P/(8Bh)$. Considering equilibrium in the $x$-direction, we have the expression of $F_{C0}$ in the frictionless contact as:

$$F_{C0}^{ENF} = \frac{3Pa}{8h} \tag{2.75}$$

The compressive force on the surface of the starting defect in Figure 2.14, $P_C^{ENF}$, is equivalent to the reaction force at the right support. That is

$$P_C^{ENF} = \frac{P}{4} \tag{2.76}$$

Thus, the expression of $f$ (Eq. (2.73)) for the ENF specimen, $f^{ENF}$, is

$$f^{ENF} = \frac{2\mu_f}{3}\frac{h}{a} \tag{2.77}$$

and the corresponding expression for $e_f$ is

$$e_f^{ENF} = \frac{4\mu_f}{3}\frac{h}{a} - \frac{4\mu_f^2}{9}\left(\frac{h}{a}\right)^2 \tag{2.78}$$

The above equation suggests that the frictional force effect in the ENF test can be fully characterized by the product of $\mu_f$ and the ratio of half thickness $h$ to crack length $a$.

Using the same approach, the expression of $f$ for the 4ENF test is

$$f^{4ENF} = \frac{8\mu_f}{3}\frac{h}{2L-d} \tag{2.79}$$

and for the ELS test

$$f^{ELS} = \frac{2\mu_f}{3}\frac{h}{a} \tag{2.80}$$

in which the geometrical parameters are defined in Figure 1.2.

The validity of the above derivation can be verified by comparing the analytical expressions for the frictional force effect by other methods in the literatures. Carlsson et al. [4], using Griffith's crack growth criterion, estimated the upper bound of the frictional force effect in the ENF test and a similar expression was provided. However, due to the misuse of shear deformation in the expression for the beam deflection, the second order term in their expression is different from that in Eq. (2.78). Kageyama et al. [10] derived the expression for the 4ENF test, but the second order term was missing. In Chapter 3, these analytical expressions will be further verified using FEM.

## 2.4 Concluding remarks

This chapter introduces two analytical methods, the compliance method and the CTE analysis, for deriving the analytical expressions of the energy release rate. Examples are given to demonstrate the derivation of $G$ in beam and plate structures. Specifically, the compliance method has been used successfully in mode II delamination tests, i.e. the ENF, ELS and 4ENF tests, and has proven the irrelevancy of shear deformation to the energy release rate. CTE analysis was used to assess the frictional force effect in the mode II delamination tests by a simple formula.

The drawback of the analytical approaches is that they may not be applicable to problems that involve complex geometry, loads or boundary conditions. In addition, both the compliance method and the CTE analysis are within the scope of linear elastic systems that limits the scope of their applications.

# Chapter 3 FEM Based Techniques for the Calculation of Energy Release Rate

The previous chapter introduces the analytical methods for deriving energy release rates and demonstrates their applications in cracked beam and plate structures. It also points out that the analytical approaches are generally restricted to simple problems within linear elastic regime. In this chapter FEM based techniques will be employed to evaluate the energy release rate. The FEM-based methods are more proficient than the analytical methods in dealing with nonlinear material properties, complicated geometries or multiple cracks. This chapter firstly reviews the existing FEM-based methods for calculating $G$ in the literature and summarizes their application limitations; secondly introduces a new approach, named energy derivative technique (the EDT), which has no restrictions in applying to any quasi-static fracture problems; and thirdly gives case studies using the EDT in composite and non-composite structures that may involve large deformation, complex loading or path-dependent processes (e.g. cases with friction and plastic deformation).

## 3.1 Review of the existing FEM-based methods

Existing FEM-based techniques in the literature, such as compliance derivative technique (CDT) [11, 12], virtual crack closure technique (VCCT) [11-15] and the $J$-integral [16-18] have been successfully demonstrated for the prediction of $G$, and the results suggest

that these FEM-based techniques can provide benchmark values to evaluate the accuracy of the analytical expressions for $G$. The principles behind these methods and their limitation in applications are briefly reviewed in the following content.

### 3.1.1 Compliance derivative technique

The CDT has been widely used to determine $G$ for the delamination in fiber composites. This technique is indeed the FEM version of the compliance method discussed in the previous chapter, as both acquire $G$ using the derivative of $C$ (see Eq. (2.2)). Since FEM cannot give explicit expression of $C$, numerical algorithms are needed to provide the derivative of $C$ with respect to $A$ using discrete $C$ and $A$ values from the output of FEM, among which finite differential approach was most often used [11]. The application of compliance derivative technique is limited to a linear elastic system.

### 3.1.2 Virtual crack closure technique

The VCCT is based on Irwin's virtual crack closure method [9] which is also the basis of the CTE analysis (see Section 2.3). The VCCT was first developed by Rybicki and Kanninen [13] using 2D 4-node linear elements, as depicted in Figure 3.1. Assuming that element size is vanishingly small and material behaves linearly, $G$ for crack growth can be calculated from the product of nodal forces at the crack tip and the relative displacements between the adjacent nodes on the crack faces,

$$G = \frac{1}{2}[(u_{1,a} - u_{1,b})F_{c1} + (u_{2,a} - u_{2,b})F_{c2}]\frac{1}{\Delta a} \tag{3.1}$$

where $u_a$ and $u_b$ are the displacements of the node pair in front of the crack tip in the local 1-direciton perpendicular to crack extend direction, $v_a$ and $v_b$ the displacements in the 2-direction, $F_{c1}$ and $F_{c2}$ the nodal forces in the 1- and 2-directions, respectively, and $\Delta a$ the length of the four crack tip elements (Elements 1-4 of Figure 3.1) in 1-direction.

The VCCT calculates $G$ from the quantities in the crack tip region, thereby not restricted to complicated loading condition. The original VCCT [13] can be easily extended to higher order [19] and 3D [20] elements. The VCCT was also used to separate fracture modes [19] by assuming that the first term in the bracket of Eq. (3.1) is corresponding to the opening component of $G$ and the second term corresponding to the shear fracture.

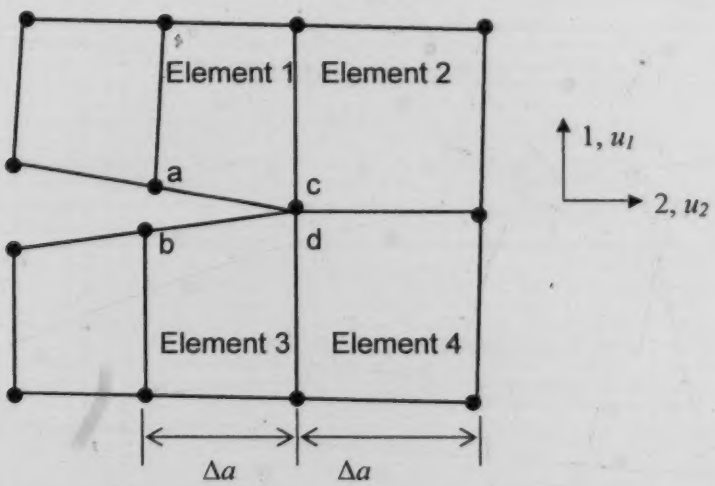


Figure 3.1 Mesh at the crack tip for the VCCT.

The nodal forces in the VCCT are determined by placing very stiff spring elements between the node pairs at the crack tip, thus elaborate manipulation on the mesh at the crack tip is required to build the proper FEM model. In practice, this method suffers from tedious modeling processes that include the regeneration of mesh when $G$

values for a range of crack lengths are needed. Besides, the VCCT is applicable to linear elastic materials only.

### 3.1.3 The *J*-integral

The *J*-integral is defined as [21],

$$J = \lim_{\Gamma \to 0} \int_{\Gamma} \mathbf{n} \cdot (U\mathbf{I} - \boldsymbol{\sigma} \cdot \mathbf{u}\nabla) \cdot \mathbf{q} d\Gamma \tag{3.2}$$

where $\Gamma$ is an arbitrary contour from the top surface of a crack to the bottom surface of the same crack, as shown in Figure 3.2, $\mathbf{n}$ is the unit vector normal to $\Gamma$ and pointing outwards, $\boldsymbol{\sigma}$ the Cauchy stress tensor, $\mathbf{u}$ the displacement vector, $\mathbf{q}$ a unit vector in the crack advancement direction, $\mathbf{I}$ the unit 2nd order tensor and $U$ the strain energy density defined as $\int \boldsymbol{\sigma} : d\boldsymbol{\varepsilon}$, where $\boldsymbol{\varepsilon}$ denotes the strain tensor. The numerical evaluation of the *J*-integral in FEM generally uses its equivalent form which is converted to domain integration by divergence theorem. Detailed explanations and FEM formulations were given by Shin [21].

The *J*-integral does not require the material to be linear elastic, but prohibits unloading when applying to elastic-plastic materials. That is, the crack advance must be infinitesimally small to avoid large scale unloading. Body force is not allowed in the *J*-integral to ascertain a constant value along different contours. In addition, the *J*-integral is based on the assumption of small deformation. Therefore, it cannot be applied to situations that involve large deformation with significant crack propagation.

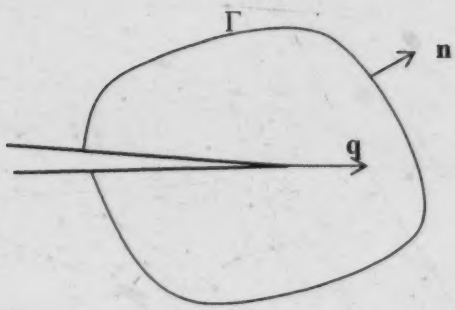


Figure 3.2 Definition of the *J*-integral.

## 3.2 Energy derivative technique

### 3.2.1 Principle of the energy derivative technique

The energy derivative technique (the EDT) is based on the original definition of $G$ (Eq. (2.1)). It deduces the $G$ values by analyzing the change of energies from the output of a FEM model. In Eq. (2.1), the energies $W$ and $U$ can be determined by implementing subroutines in the FEM codes. In some commercial codes, such as ABAQUS, functions are already available to determine these energies.

the EDT requires calculation of derivatives of energies with respect to the crack area $A$. A three-point parabolic segment algorithm is chosen here to perform this calculation. Explicitly, the energy quantity, $Y$ (representing $W$ or $U$), is written as a function of $A$ by a 2nd order Lagrange interpolating polynomial

$$Y(A) = Y_i \frac{(A-A_{i-1})(A-A_{i+1})}{(A_i-A_{i-1})(A_i-A_{i+1})} + Y_{i+1} \frac{(A-A_i)(A-A_{i-1})}{(A_{i+1}-A_i)(A_{i+1}-A_{i-1})} + Y_{i-1} \frac{(A-A_i)(A-A_{i+1})}{(A_{i-1}-A_i)(A_{i-1}-A_{i+1})} \tag{3.3}$$

which passes through 3 consecutive data points $(Y_{i-1}, A_{i-1})$, $(Y_i, A_i)$ and $(Y_{i+1}, A_{i+1})$. The derivative is given by the gradient of the above equation at $A=A_i$. Note that the

derivatives at the first and last data points are simply based on the slopes of their associated parabolas at those points.

The EDT requires that all the energy values come from one FEM model in which the change of the crack length has been incorporated in the simulation to reflect the true history of the energy variation. Therefore, the EDT can determine $G$ of path-dependent problems such as large-scaled crack growth in structures involving extensive plastic deformation, even when friction exists between the contact surfaces.

Another advantage of the EDT is that the energy quantities in FEM are easy to converge without mesh refinement. For example, for a crack in a linear elastic material, the stress field in the vicinity of the crack tip has $r^{-1/2}$ singularity, where $r$ is the distance from the crack tip. The strain energy density, proportional to $\sigma^2$, has $r^{-1}$ singularity. When multiplying strain energy density by the area which is proportional to $r^2$ to represent the energy of the crack tip region, the singularity is removed. As a result, fine mesh in the vicinity of the crack tips is not necessary.

Moreover, applications of the EDT are not limited to small deformation that is prerequisite for the $J$-integral, the VCCT and the CDT methods.

As an intrinsic drawback of the total energy approach, the EDT cannot distinguish the energy dissipated in each fracture mode from the total energy change, thereby not being able to determine the fracture mode. Table 3.1 summarizes the application conditions of the EDT and those discussed in the previous section.

Table 3.1 FEM-based techniques for the energy release rate and their application conditions ("Y" means applicable while "-" means not applicable)

| | CDT | *J*-integral | VCCT | the EDT |
|---|---|---|---|---|
| Complex loading | - | Y | Y | Y |
| Nonlinear elasticity | - | Y | - | Y |
| Large deformation | - | - | - | Y |
| Friction | - | - | Y | Y |
| Plastic deformation | - | - | - | Y |
| Mode separation | - | - | Y | - |

### 3.2.2 Special forms of the *G* expression

*Constant displacement*

When subjected to constant displacement, $dw = 0$. Thus, Eq. (2.1) can be simplified as

$$G = -\frac{\mathrm{d}U}{\mathrm{d}A} \tag{3.4}$$

*Constant force in linear elastic fracture*

When subjected to constant force in linear elastic fracture, d$W$ equals two times of d$U$. Therefore, Eq. (2.1) becomes

$$G = \frac{\mathrm{d}U}{\mathrm{d}A} \tag{3.5}$$

*With friction*

When friction exists during crack propagation, the work consumed by the friction should be excluded from the $G$ calculation. In this case, d$W$ in Eq. (2.1) should be replaced by (d$W$ – d$F$), where $F$ is the total energy dissipated by the friction. Thus the corresponding $G$ expression becomes,

$$G = \frac{dW}{dA} - \frac{dF}{dA} - \frac{dU}{dA} \tag{3.6}$$

### 3.2.3 Example: *G* of a penny-shaped crack in a plate

The penny-shaped crack example in section 2.3.1 is studied to demonstrate the application of the EDT.

The FEM model of the cracked plate was built in the commercial software ABAQUS. Because both the geometry and load are axisymmetric, only the rectangular revolving cross-section of the plate was modeled, consisting of 760 axisymmetric elements with incompatible mode (CAX4I). Figure 3.3(a) shows the mesh pattern and prescribed condition of the finite element model that is simply supported at $r = R$ with a unit force loading at the center.

Crack is assumed to develop in the radial direction within the mid-plane. The crack growth is simulated using a "debonding" technique that is available in ABAQUS for a pre-set path, as indicated by a thick line in Figure 3.3(a). The crack length increases automatically as a function of an artificial time that controls the crack growth rate. Frictionless contact was assigned to the crack surfaces. Material was assumed to be linear elastic. Dimensions and material properties are listed in Table 3.2. Note that the values are dimensionless, as this example only serves as a guide to performing the EDT.

Table 3.2 Material and geometrical properties used in the penny-shaped crack model.

| $E$ | $v$ | $2h$ | $R$ | $a$ | $P$ |
|---|---|---|---|---|---|
| $2E+10^5$ | 0.3 | 5 | 50 | 2.5~50 | 1 |

The convergence of mesh density is checked based on the relative change of total strain energy $U$ with the refinement of the mesh, because Eq. (3.5) is used for constant force condition. Values of $U$ for each crack growth increment were given by the variable "ALLSE" of the output database of ABAQUS. The $U$ values from the baseline model and another model with refined mesh, a total of 1590 elements, are plotted in Figure 3.3(b) as a function of crack radius $a$. Difference of the values between the two models is less than 0.005%, suggesting that fine mesh is not necessary to reach the converged $U$ values.

$G$ values determined from the EDT based on the regular mesh (the one with 760 elements) are presented in Figure 3.3(c) by dot symbols, and those from the finer mesh model by cross symbols. For the crack with radius $a$ in the range from 5 to 45, a difference of up to 0.4% exists, showing the good convergence of the $G$ values. The noticeable difference at crack lengths shorter than 5 or longer than 45 is because of the abrupt change of $G$ in these regions. The finer mesh with more data points, obviously, captures the detailed variation of $G$, thereby giving slightly different $G$ values from those from the model with the regular mesh. The theoretical prediction of the energy release rate (Eq. (2.52)) is also plotted in Figure 3.3(c) as a straight solid line that shows good agreement with the EDT solutions. Some discrepancy exists at small crack size, especially for $a$ being shorter than 25. The discrepancy is probably due to the limitation of the analytical solution that is based on the assumption of the in-plane dimensions being much larger than the plate thickness.

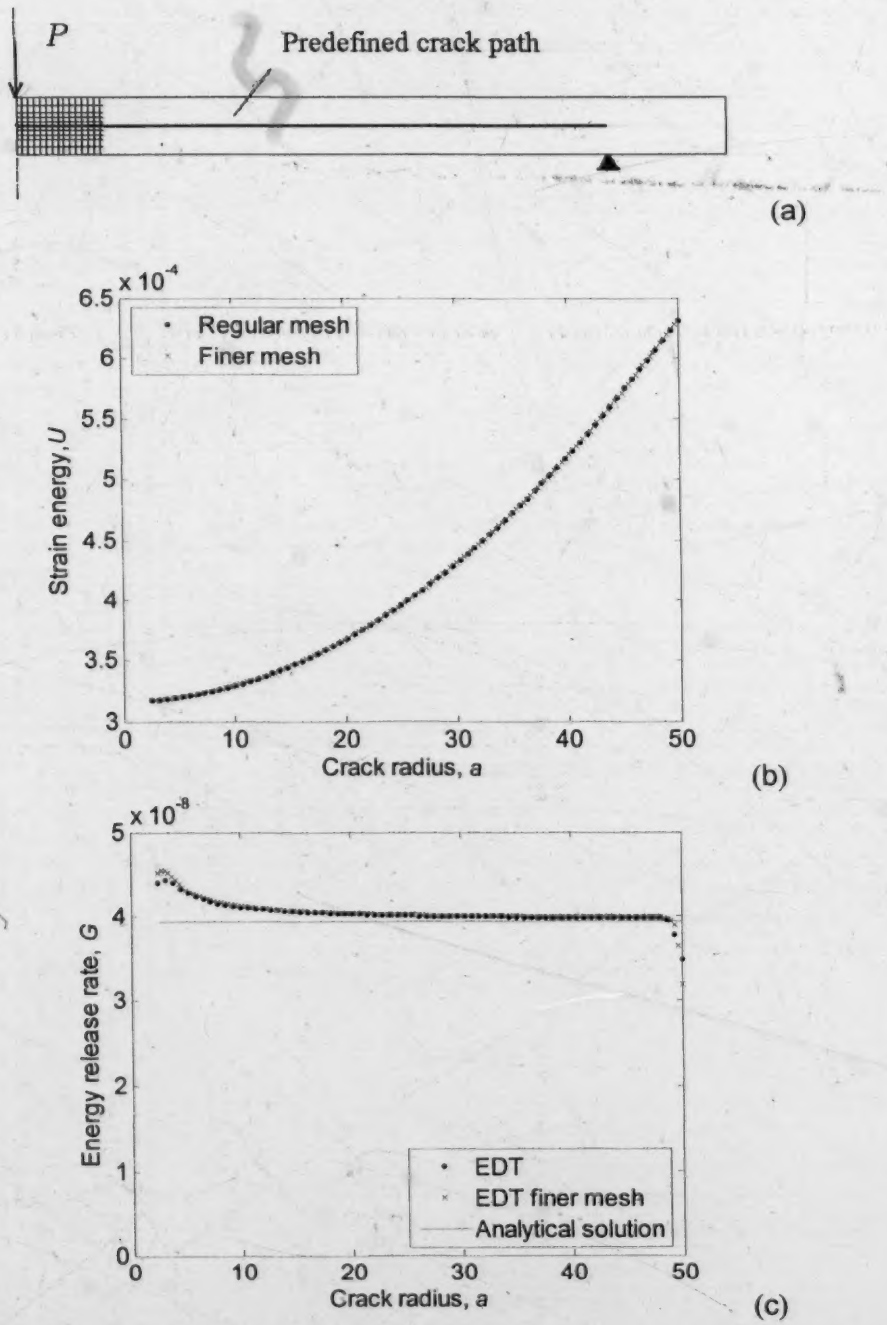


Figure 3.3 Penny-shaped crack in a plate: (a) the FEM model, (b) plot of $U$ versus $a$ for two different meshes, and (c) $G$ by the EDT and the analytical solution.

### 3.2.4 Example: *G* of a cracked beam under 3-point bending

The EDT is applied to the example discussed in Section 2.2.1.4 to verify the analytical expressions of *C* (Eq. 2.25) and *G* (Eqs. (2.26-2.32)) in a beam with an internal crack.

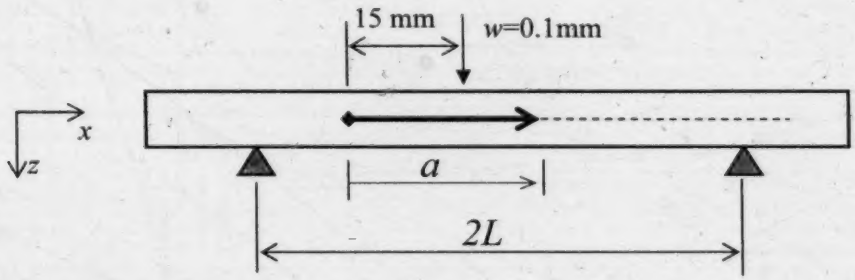


Figure 3.4 Predefined crack path in the cracked beam.

The FEM model of the cracked beam is built using two-dimensional plane-stress elements (CPS4I) with incompatible mode in ABAQUS. The beam is subjected to a constant displacement of 0.1 mm at the central loading point. Contact conditions between the newly formed fracture surfaces were specified using frictionless and small sliding contact formulation. The nodal points at the two supports were restricted from any vertical motion during the crack growth. Material properties for the FEM model are given in Table 3.3, based on unidirectional glass fiber/polyester with fiber volume fraction 45%.

To verify the *C* and *G* expressions in different scenarios of Figure 2.6, a fictitious crack growth was made up, by assuming that the crack initiates in the left half of the span section, at a distance 15 mm away from the central loading point, as shown by the diamond symbol in Figure 3.4, and the crack grows in the right direction only. The crack grows firstly towards the central loading point (Scenario 1 of Figure 2.6), and then through the right half of the span section (Scenario 2) with the final arrest after passing

over the right support (Scenario 3), as depicted in Figure 3.4. Similar to the previous example, the crack growth was implemented by "debonding".

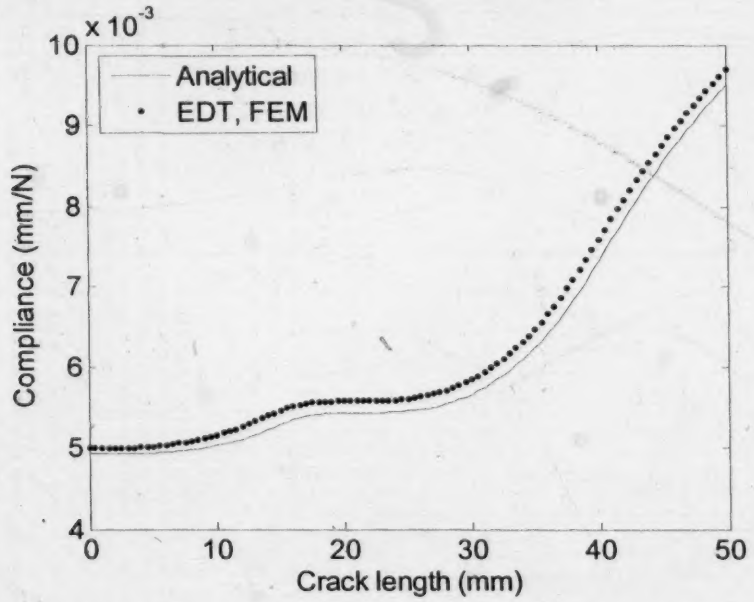


Figure 3.5 Comparison between FEM and analytical solution: (a) compliance and (b) the energy release rate, $G$.

Figure 3.5(a) compares the FEM compliance with the analytical prediction and shows that they match each other well. The EDT-determined $G$ values are plotted in Figure 3.5(b), compared with the analytical solution. The good correlation between the plots gave confidence on both the analytical approach and the EDT. The relatively large discrepancy, occurring when the crack tip passed the loading and right support position, is because the ideal conditions used by the analytical derivation, such as the sudden change of the shear force direction but otherwise the same magnitude (see Figure 2.7), are not realistic, thus not reflected by the FEM model.

Table 3.3 Material properties of the cracked beam

| | $E_{11}$ (GPa) | $E_{22} = E_{33}$ (GPa) | $G_{13} = G_{12}$ (GPa) | $\nu_{23}$ | $\nu_{12} = \nu_{13}$ |
|---|---|---|---|---|---|
| Glass/polyester composite | 28.6 | 6.0 | 6.0 | 0.3 | 0.3 |

## 3.3 Frictional force effect on $G$ using the EDT

Analytical approach on the frictional force effect in mode II tests using beam type specimens has been given in Section 2.3.2. Here, numerical analysis will be carried out by the EDT to perform the same evaluation.

### 3.3.1 Expression of $G$ with friction and constant force loading

The general expression of the energy release rate when friction is involved in fracture is given in Eq. (3.6). In a linear elastic system subjected to constant forces, with the frictional force being proportional to the external load, Eq. (3.6) can be further simplified to be

$$G = \frac{dU}{dA} \tag{3.7}$$

This equation takes the same form as the expression for the linear elastic fracture without friction (Eq. (3.4)). This equation, as to be proved in the following paragraphs, not only simplifies the data reduction procedure by reducing 3 quantities in Eq. (3.6) into one, but also serves as the basis for some analysis on the effect of friction [22].

Due to the non-conservative nature of the frictional force, the variables in the numerator of Eq. (3.6) must be determined based on the loading situation depicted in State 1 of Figure 3.6, for crack growth with initial crack length $a_0$. Let crack advance start when the force reaches $P_1$, and the crack length increase from $a_0$ to $a_1$ at the same loading level, as illustrated in state 1 to point A of Figure 3.6. Strain energy at point A, $U_A$, is equal to that at point A′, $U_{A'}$, of State 2 which is subjected to the same loading but the initial crack length is $a_1$. In State 2, the expression for $U_{A'}$ (equal to $U_A$) could be easily obtained as:

$$U_{A'} = \frac{1}{2}\left(\sum P_i \delta_i\right)\Big|_{a=a1} - \frac{1}{2}\left(\sum f_i \eta_i\right)\Big|_{a=a1} = U_A \tag{3.8}$$

where $P_i$ and $f_i$ are external and frictional forces, respectively, and $\delta_i$ and $\eta_i$ are the associated displacements of $P_i$ and $f_i$. Similarly, the strain energy at point B, where the crack length is $a_1+da$, is,

$$U_B = \frac{1}{2}\left(\sum P_i \delta_i\right)\Big|_{a=a1+da} - \frac{1}{2}\left(\sum f_i \eta_i\right)\Big|_{a=a1+da} = U_B \tag{3.9}$$

The change of strain energy from A to B in State 1 is:

$$\begin{aligned} dU_{AB} &= U_B - U_A \\ &= \frac{1}{2}\left[\left(\sum P_i \delta_i\right)\Big|_{a=a1+da} - \left(\sum P_i \delta_i\right)\Big|_{a=a1}\right] - \frac{1}{2}\left[\left(\sum f_i \eta_i\right)\Big|_{a=a1+da} - \left(\sum f_i \eta_i\right)\Big|_{a=a1}\right] \end{aligned} \tag{3.10}$$

Since $P_i$ and $f_i$ are constant, the above equation becomes

$$dU_{AB} = \frac{1}{2}\sum P_i \cdot d\delta_i - \frac{1}{2}\sum f_i \cdot d\eta_i \tag{3.11}$$

Also,

$$dW_{AB} = \sum P_i \cdot d\delta_i \tag{3.12}$$

and

$$dF_{AB} = \sum f_i \cdot d\eta_i \tag{3.13}$$

By substituting Eqs. (3.11-3.13) into Eq. (3.6), it yields

$$G = (\frac{1}{2}\sum P_i \cdot d\delta_i - \frac{1}{2}\sum f_i \cdot d\eta_i)/da = \frac{dU_{AB}}{da} \tag{3.14}$$

Therefore, even with the consideration of friction in the circumstance of constant force, the expression of $G$ is still taking a simple form, same as that without the friction.

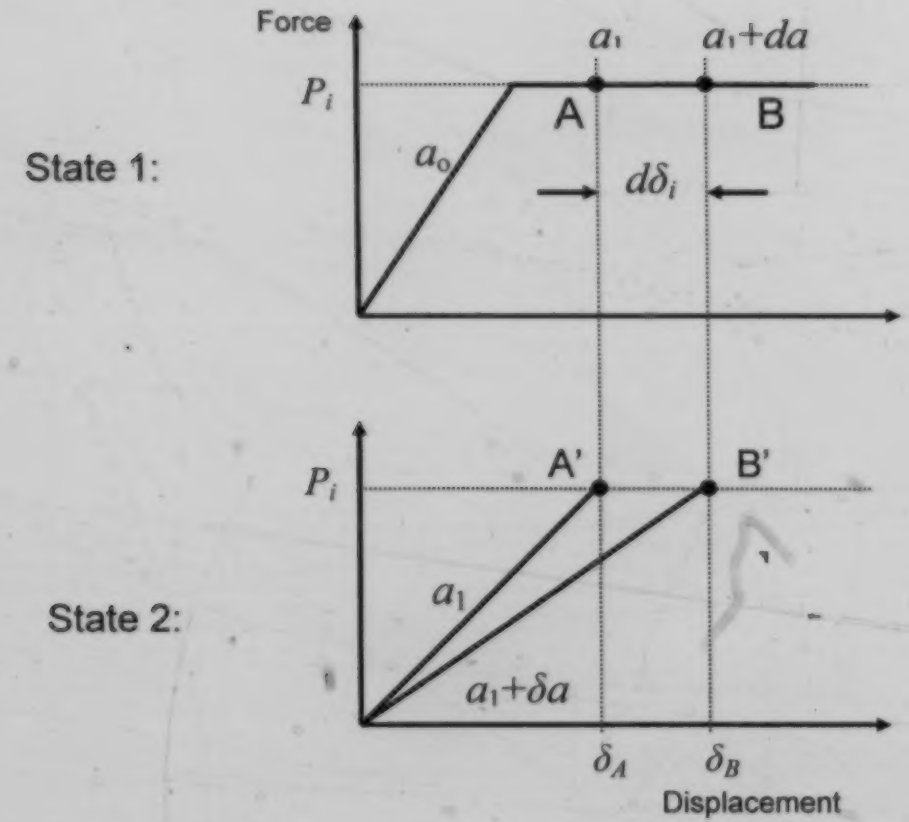


Figure 3.6 Monotonic load-displacement curves for crack growth with friction.

### 3.3.2 Frictional force effect in the ENF and 4ENF tests

Applying the EDT to the ENF and the 4ENF tests and assuming friction exists on the crack surfaces, the frictional force effect on the energy release rate are studied by the EDT and the results are compared here with the analytical solution obtained in Section 2.3.2.

Two similar FEM models of ENF specimens were built in ABAQUS to calculate $G_0$ ( the energy release rate with frictionless condition, defined in Section 2.3.2) and $G_f$

(with friction) using the EDT. The only difference between these two models is that the coefficient of friction $\mu_f$ between the fracture surfaces was either 0 or 0.5. For the comparison with existing results in literatures, dimensions and material constants followed those used in "model set 2" of Ref. [23]. The FEM model of the ENF specimen is shown in Figure 3.7. A unit force was applied at the top central node of the model and remained constant during the delamination growth, which was the same loading condition as that used in Ref. [23]. The nodes on the supports were constrained from any vertical movement, and the central nodal point at the bottom was constrained from any horizontal movement, to remove the rigid body motion. Crack growth was confined to be along a pre-defined path in the mid-thickness, with $a/L$ in the range from 0.45 to 0.95, which covers the range commonly used in the experimental studies.

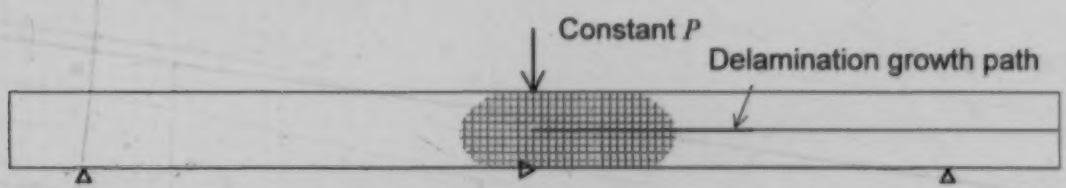


Figure 3.7 FEM model of the ENF test for studying the frictional force effect.

Energy release rates $G_0$ and $G_f$ of the ENF specimens were calculated by the EDT using Eq. (3.7). The difference of $G_f$ and $G_0$ was then normalized by $G_0$, to represent the frictional force effect $e_f$ (Eq. (2.71)). Values of $G_0$ and $G_f$ were also calculated using a more general expression of energy release rate (Eq. (3.6)), and their difference from those determined using Eq. (3.7) was found to be less than 0.1%, further confirming the validity of the simplified expression of Eq. (3.7) for determining $G$ when subjected to the constant-force loading condition.

When investigating the 4ENF test by the EDT, $e_f$ was found to be a constant by changing the crack length because the factor $f$, i.e. the determinant of $e_f$, is independent of the crack length according to Eq. (2.79). As a result, several $\mu_f$ values were used to vary $f$ in the study of the 4ENF test.

Figure 3.8 summarizes the variation of $e_f$ with respect to $f$ in the ENF and 4ENF tests. The $e_f$ values are from the analytical solution (Eq. (2.74)), the EDT and Ref. [23] by the VCCT. The figure shows that these three solutions match each other perfectly. By comparing $(G_0 - G_f)/G_0$ values of two data points, indicated by the arrows in Figure 3.8 to represent results for specimens with the most common dimensions and setup configurations of the ENF and 4ENF tests, the 4ENF test has apparently more significant frictional force effect than the ENF test. It should be noted that the frictional force for the ENF and 4ENF tests only exist in regions where the crack is generated by a Teflon or waxed aluminum film, and thus the possible $\mu_f$ is unlikely to be more than 0.5, as supported by the experimentally determined coefficient of friction of 0.374 [24] or 0.35 [25]. Therefore, the realistic $e_f$ values to represent the effect of the frictional force in both tests should be even less than those pointed by the arrows in Figure 3.8.

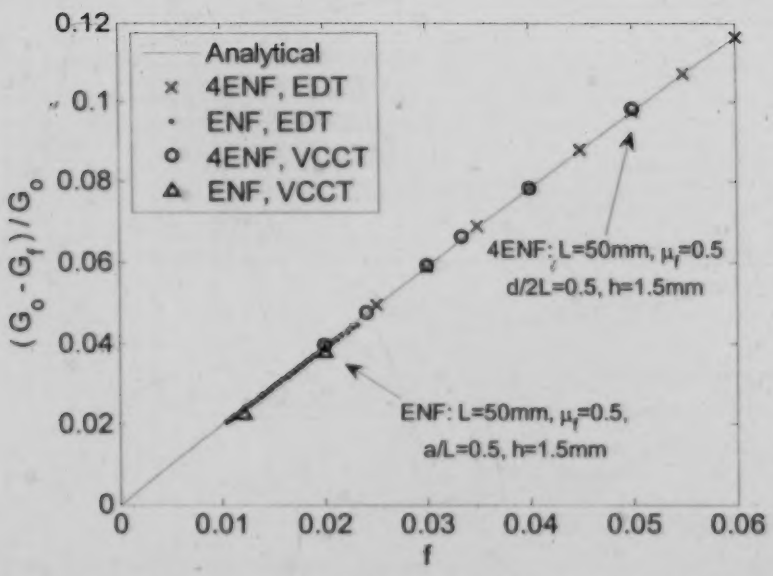


Figure 3.8 The frictional force effect in the ENF and 4ENF tests, predicted by analytical solution, the EDT and the VCCT.

## 3.4 Applications of energy derivative technique in nonlinear fracture

In this section, the EDT will be applied to nonlinear fracture problems which are beyond the capabilities of the *J*-integral, the CDT, and the VCCT. Two problems will be discussed: (1) a rubber sheet with a central crack and (2) large crack propagation in double-edge-notched tensile (DENT) test. Material nonlinearity, large and irrecoverable deformation, and long crack propagation are involved in the studies.

### 3.4.1 Central crack in a rubber sheet

This case study is to demonstrate the use of the EDT to calculate *G* for large deformation in a nonlinear elastic system. Consider a thin rubber sheet with a central crack subjected to simple tension as shown in Figure 3.9(a). Dimensions of the rubber sheet in the stress-

free condition are $2L$ for the width and the length and $2a$ for the initial crack length. Opening of the crack in the centre is $2b$ when subject to tensile loading.

Due to symmetry of the specimen and the loading conditions, a FEM model equivalent to quarter of the rubber sheet was used for the analysis. The model contains 2400 plane-stress elements (CPS4), with the mesh pattern shown in Figure 3.9(b). Values of the half crack length ($a$), the half width ($L$), the initial shear modulus ($\mu_0$) and the extension ratio ($\lambda_y$) are listed in Table 3.4. Symmetric boundary conditions were applied along the two axes of symmetry, and a constant displacement of 2 for $\lambda_y$ was applied along the top edge. The half crack length was set to grow from 0 to $L$ using the technique similar to that used for Section 3.2.3.

Table 3.4 Material and geometrical properties used in the rubber sheet model.

| $\mu_0$ | $\lambda_y$ | $L$ | $a/L$ |
|---|---|---|---|
| 100 | 2 | 20 | 0~1 |

Since the deformation is subjected to constant displacement, $G$ values from the FEM model were determined using Eq. (3.5), in which $U$ is the recoverable strain energy, and equals the value for the output variable "ALLSE" in ABAQUS.

Figure 3.9(c) compares the FEM results with those from an analytical expression reported by Yeoh [26] that was derived for a crack in a square rubber sheet with size much larger than the crack length. In Yeoh's case [26],

$$G = \pi \sigma_y b / 2 \tag{3.15}$$

where $b$ is the maximum crack opening width, determined using finite element analysis, and $\sigma_y$ the normal stress in the far field. For the loading scenario given in Figure 3.9(b),

with $\lambda_y$ equal to 2, value of $\sigma_y$ in Eq. (3.15) was determined from the following equation [27]:

$$\sigma_y = 2(\lambda_y - \lambda_y^{-3})\left(\frac{\partial W_I}{\partial I_1} + \frac{\partial W_I}{\partial I_2}\right) \tag{3.16}$$

where $W_I$ is a strain energy density function for hyperelastic material that can be expressed in terms of the first invariant $I_1$ of the left Cauchy-Green strain tensor [27]:

$$W_I = C_{10}(I_1 - 3) + C_{20}(I_1 - 3)^2 + C_{30}(I_1 - 3)^3 \tag{3.17}$$

where the constants are: $C_{10} = \mu_0 / 2$, $C_{20} = -\mu_0 / 20$, and $C_{30} = \mu_0 / 100$.

Since Eq. (3.15) is only valid when the crack length is much shorter than the width and the length of the rubber sheet, $G$ values obtained from the equation is only plotted in Figure 3.9(c) for $a/L$ less than 0.1. The comparison suggests that $G$ values from the EDT match very well with $G$ values from Eqn. (3.15). The figure also suggests that the EDT has the advantage over the analytical solution in that the former is not limited to small crack size.

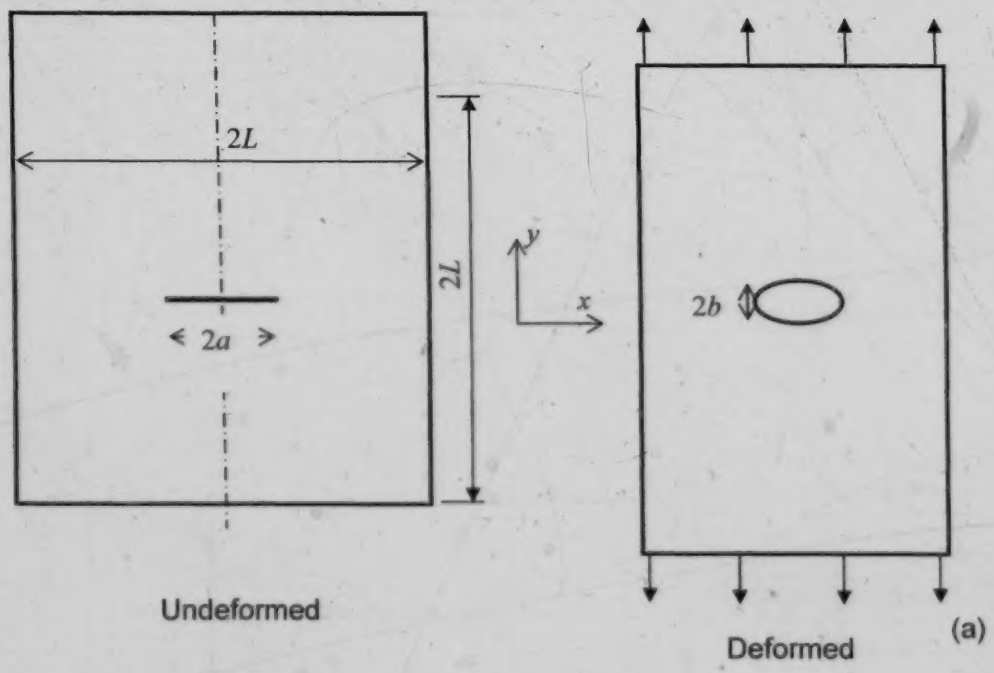
2L
2L
2a
y
x
2b
Undeformed
Deformed
(a)

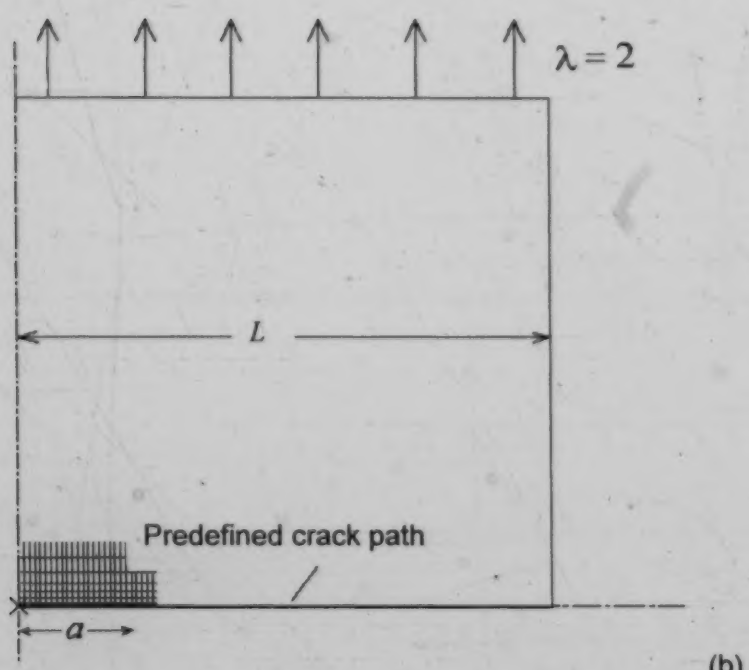
λ = 2
L
Predefined crack path
a
(b)

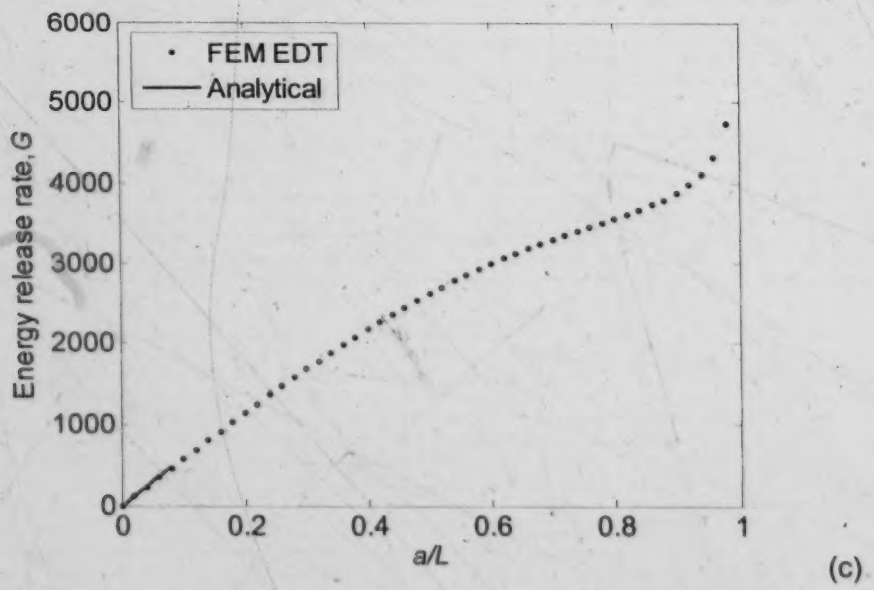


Figure 3.9 Rubber sheet with a central crack in tension: (a) geometries, (b) FEM model, and (c) comparison of $G$ values from the EDT and Eq. (3.15).

### 3.4.2 Double-edge-notched tensile test

This case study is to illustrate the use of the EDT for the evaluation of $G$ for crack growth in elastic-plastic materials. As shown in Figure 3.10(a), a double-edge-notched specimen is subjected to uniform tensile loading, of which dimensions and material properties are listed in Table 3.5. Again, due to symmetry of specimen geometry and loading condition, only one quarter of the specimen is modeled using FEM.

Table 3.5 Material and geometrical properties used in the DENT model.

| $E$ | $\nu$ | $\sigma_0$ | $\alpha$ | $n$ | $L$ | $a/L$ |
|---|---|---|---|---|---|---|
| $3\times10^7$ | 0.3 | $4\times10^4$ | 0.5 | 5 | 20 | 0~0.8 |

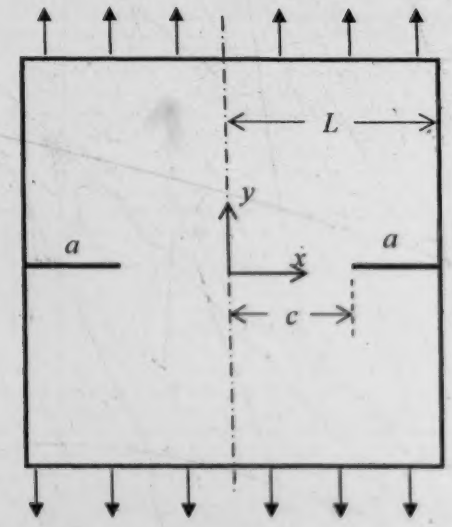


(a)

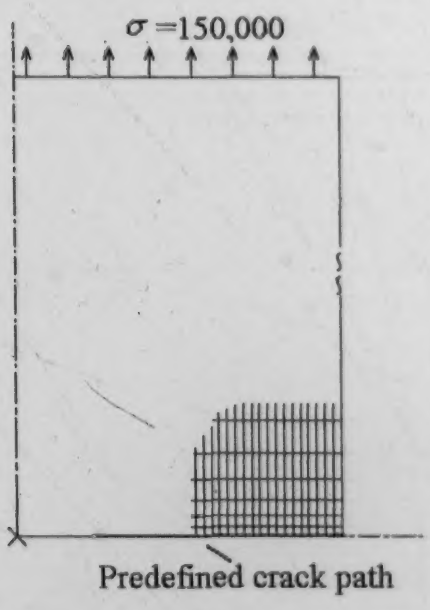


(b)

Figure 3.10 Plastic deformation of DENT test: (a) specimen configuration, and (b) FEM model.

The model contains 1480 2D hybrid plane-strain 4-node elements (CPE4H) with the mesh pattern shown in Figure 3.10(b). A constant tensile stress of 150,000 that is 3.75

times the yield stress ($\sigma_0$ in Table 3.5) is applied along the top edge of the model as far-field loading. The crack length $a$ increased from 0 to 80% of the half specimen width $L$ using the "debonding" technique, similar to that used in the previous case studies.

The FEM analyses were conducted using two material models that are based on either deformation plasticity theory or incremental plasticity theory. Typical stress-strain curves of the two material models are presented in Figure 3.11, which are essentially the same in the loading phase when the stress increases monotonically. However, during the unloading phase, the two material models show different stress-strain relationships, as the incremental plasticity theory considers linear elastic unloading while the deformation plasticity theory assumes the same stress-strain relationship as that for the loading phase.

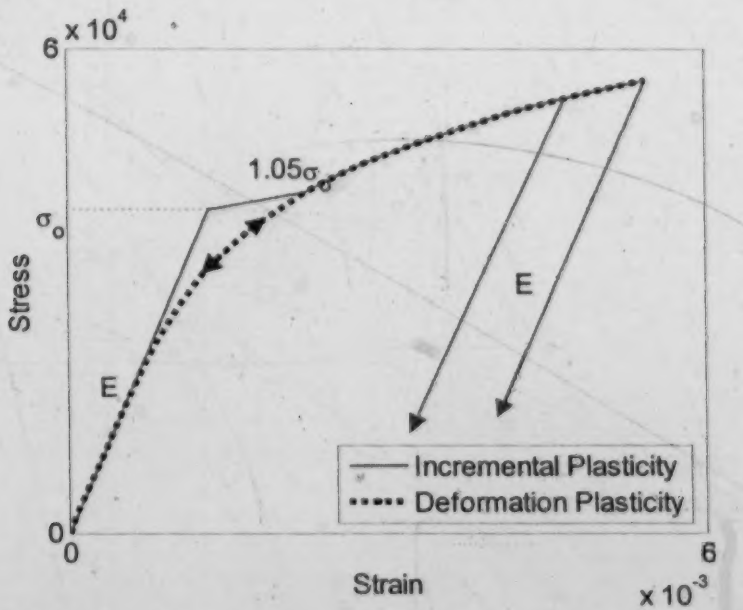


Figure 3.11 Stress-strain curves based on the incremental plasticity theory and the deformation plasticity theory.

Since the case study considers a large range of crack propagation, involving significant unloading behind the crack tip, different results are expected for $G$ based on the two plasticity theories.

*Deformation plasticity theory*

Based on Ramberg-Osgood model [16], stress and strain involving plastic deformation have the following relationship:

$$E \cdot \varepsilon = \sigma + \alpha \left( \frac{|\sigma|}{\sigma_0} \right)^{n-1} \sigma \tag{3.18}$$

where $\alpha$ is the "yield" offset, and $n$ (>1) the hardening exponent for the plastic deformation.

$G$ values were determined based on Eq. (3.3) using the EDT. It should be noted that in this case, $U$ in Eq. (3.3) consists of the dissipated energy for the plastic deformation (output variable ALLPD in ABAQUS) and the recoverable strain energy (ALLSE in ABAQUS). The $G$ values were then converted to a dimensionless quantity $h_1$, as explained below, for comparison with results published in the literature.

Kumar et al. [28] proposed that within the framework of the deformation plasticity theory, the following $J$-integral expression can be applied to a DENT specimen when subject to fully plastic deformation:

$$J = \alpha \sigma_0 \varepsilon_0 c \left( \frac{P}{P_0} \right)^{n+1} h_1 \tag{3.19}$$

where $\varepsilon_0$ is equal to $\sigma_0 / E$, $P$ the applied load, $c$ half of the ligament length between the two notches at the load $P$, and $P_0$ the limiting load for the plane-strain condition that can be expressed as a function of $c$, $\sigma_0$, and half of the specimen width $L$:

$$P_0 = (0.72 + 1.82\frac{c}{L})\sigma_0 L \qquad (3.20)$$

Since the $J$-integral value is equal to $G$ for material models with a path-independent stress-strain relationship, the $G$ values determined in this study using the EDT were converted to the non-dimensional $h_1$ values using Eq. (3.19). The results are summarized in Figure 3.12 as a function of $a/L$. Figure 3.12 compares the $h_1$ values so determined with those using different approaches, reported in references [16, 28]. These values are in fairly good agreement.

*Incremental plasticity theory*

Figure 3.13 summarises results based on the incremental plasticity theory, after converting the $G$ values to $h_1$ using Eq. (3.19). Since no $h_1$ values based on the incremental plasticity theory are available in the literature, the $h_1$ values in Figure 3.13 cannot be verified through comparison with the published work. Nevertheless, by comparing $h_1$ values between Figures 3.12 and 3.13, it is clear that the latter (from the incremental plasticity theory) are much smaller than the former (from the deformation plasticity theory). This is consistent with the rationale that the incremental plasticity theory considers the energy dissipated through permanent plastic deformation behind the crack tip, thus the amount of energy available for forming new crack surfaces must be smaller than that based on the deformation plasticity theory.

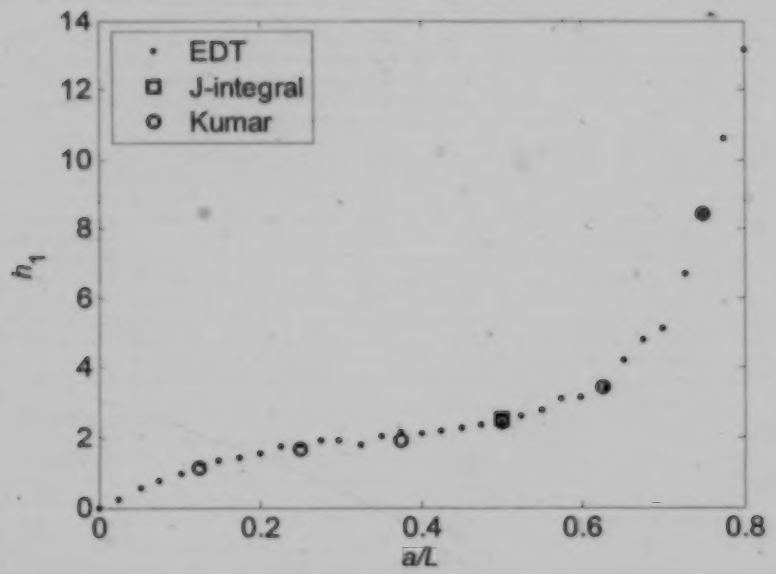


Figure 3.12 Values of $h_1$ for the DENT model using the EDT based on the deformation plasticity theory, and the comparison with those in the literature.

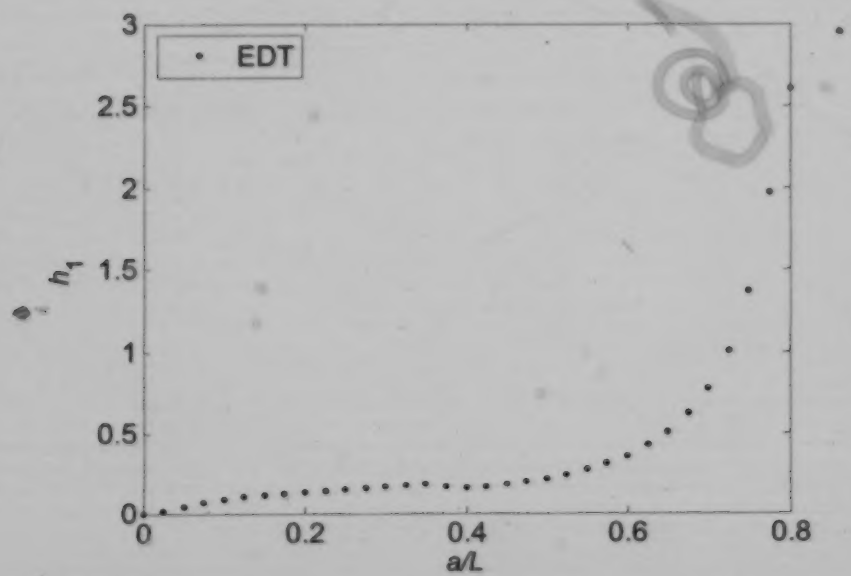


Figure 3.13 Values of $h_1$ for the DENT model using the EDT, based on the incremental plasticity theory.

## 3.5 Concluding remarks

This chapter reviewed the FEM-based methods for assessing the energy release rate in static or quasi-static crack propagation with a given crack growth pattern, and pointed out the application restrictions for each method. Then, the EDT was introduced as an alternative to the existing ones. The EDT is based on the original definition of the energy release rate without any further assumptions. Thus it is able to apply to complicated fracture problems including large and plastic deformation, which are beyond the capability of the existing techniques. Since the EDT is based on FEM, complicated geometry or crack profile, which might be intolerable for analytical methods, is not an obstacle for the EDT to determine accurate $G$ values.

Applied to fiber composites, the EDT verifies the analytical $G$ expressions for a beam with an internal crack (given in Section 2.2.1.4) by comparing the $G$ values of a fictitious crack growth pattern. The EDT is also used for numerical verification of the friction effect obtained by the CTE analysis. It is confirmed using the EDT that the frictional force effect in the ENF or 4ENF test is smaller than 8% with regular setup geometry and even reasonably large coefficient of friction.

Two more applications other than in composite materials are presented to demonstrate the use of the EDT in complex situations, such as complex loading, material nonlinearity, large deformation or rotation, and path-dependent deformation processes. The case studies show excellent consistency with the data in the literature that were obtained using either analytical or other FEM-based techniques. Results also suggest that the EDT is very efficient and versatile, with the potential to deal with complex crack propagation problems that are non-linear and involve extensive plastic deformation.

# Chapter 4 Delamination Tests for Measuring the Critical Energy Release Rates

## 4.1 Introduction

As mentioned in Chapter 1, the delamination resistance of fiber composites is characterized by the critical energy release rates ($G_C$) in three pure fracture modes, i.e. mode I, mode II and mode III. These values are generally different because the fracture mechanisms and fracture surface topography differ in each circumstance. For example, the mode I fracture surface, as shown in Figure 4.1(a) (courtesy of T. Kuboki [29]), is clean and smooth, much like a cleavage fracture. However the mode II fracture surface in Figure 4.1(b) (taken from an INF test specimen as to be discussed later) contains many matrix hackles formed through severe plastic deformation. The existence of matrix hackles also increases the net area of the fracture surface [30]. Consequently the energy required to generate unit mode II fracture surface will be more than that for mode I.

Even in pure mode fracture, the critical energy release rate may vary with crack length. This variation is probably because of the change of the number of bridging fibers [30], the level of the bluntness of the crack tip [31], or the development of the plastic zone in the vicinity of the crack tip [31]. The plot of the critical energy release rate with crack growth length is known as the resistance curve or *R*-curve.

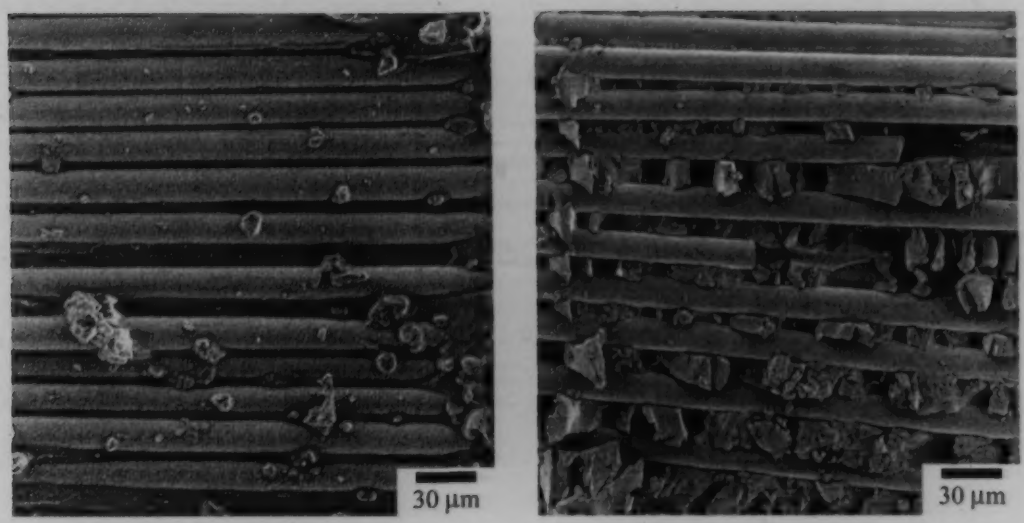


Figure 4.1 Typical fracture surface topographies of (a) mode I fracture and (b) mode II fracture.

In mixed mode fracture, the critical energy release rate $G_C$ is believed to be enveloped by the critical energy release rates in the pure fracture modes. Some empirical equations [32, 33] were used to describe the mixed mode $G_C$ as a function of $G_{IC}$, $G_{IIC}$ and mode mixing ratio. Note that $G_{IIIC}$ for the tearing mode is not often involved in the formula of $G_C$. This is because delamination in mode I and mode II is more likely to occur than mode III in composite structures, such as the delamination induced by lateral low velocity impact.

In the past 20 years, researches have devoted great efforts to develop reliable tests for the accurate measurement of $G_{IC}$ and $G_{IIC}$. This is because firstly $G_{IC}$ and $G_{IIC}$ are the most important parameters to evaluate the performance of fiber composites' resistance to fracture and secondly they are essential input quantities for simulating delamination growth using FEM (to be discussed in Chapter 6).

The accurate measurements of $G_{IC}$ and $G_{IIC}$ depend on appropriate testing methods that generate pure mode of delamination, as well as reliable data reduction strategies to extract the critical energy release rate from the measured quantities. The DCB test and its associated compliance calibration (CC) method have been standardized [2] as the mode I delamination toughness testing method. However for mode II delamination, no agreement has been reached due to some technical issues. One of the major difficulties, is the stability of delamination growth. The pioneer ENF test with the typical setup has an inherently unstable crack growth and thus making it impossible to generate an *R*-curve. Later on, the ELS test [34] was proposed to determine the *R*-curve. Theoretically, the ELS test generates stable crack growth pattern under displacement control [34], but in reality its delamination growth is not always stable [35, 36]. The 4ENF test has become a promising candidate as the standard, which can generate relatively stable delamination growth, though "stick-slip" crack growth pattern does occur occasionally [37], thus raising concerns about its growth instability.

The trend of the stability of these tests can be reflected by their load-displacement curves. With the assumption of a constant $G_{IIC}$ value during the delamination growth, the schematic load-displacement curves generated by the *G* expressions for the ENF, ELS and 4ENF tests (Eqs. (2.33-2.38)) are presented in Figure 4.2 in which the delamination growth commences where the initial slope of the loading curve is reduced. An interesting trend, as indicated in Figure 4.2, is that the stability of delamination, which is in the order of the ENF, ELS and 4ENF tests, increases with the decrease of the rate of load drop after critical point for delamination.

The next section of this chapter will introduce a new delamination test, named internal notched flexure (INF) test. The INF test does not generate any load drop after the delamination initiation, as schematically shown in Figure 4.2, indicating that the delamination growth is more stable than any of the above delamination tests. The theoretical analysis will show that the INF test generates pure mode II delamination and several data reduction methods will be proposed for the INF test to establish the *R*-curve.

In the last section of this chapter, another mode II delamination test, named "Beam test" will be introduced. The Beam test was originally developed by Kuboki *et al.* [29, 38-40] for the measurement of $G_{IIC}$. Though the "Beam test" has unstable crack growth, thereby not suitable for the $G_{IIC}$ measurement, it serves as a good example for evaluating the accuracy of the prediction of delamination onset and propagation, which will be discussed in detail in Chapters 5 and 6.

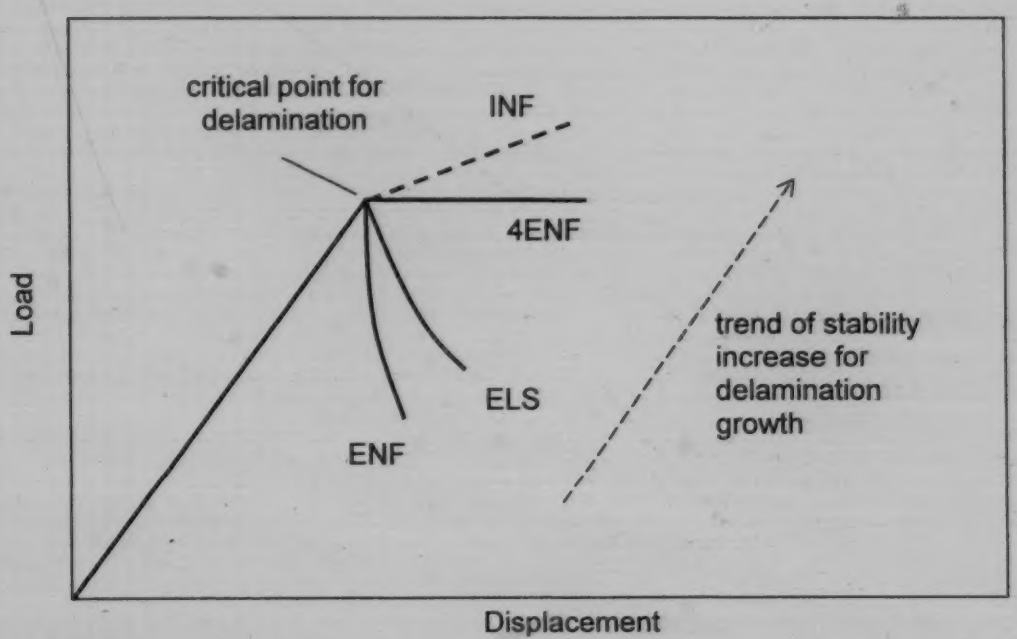


Figure 4.2 Schematic load displacement curves of the ENF, ELS, 4ENF and INF tests.

## 4.2 The internal notched flexure test

### 4.2.1 Test setup

The setup of the INF test is shown in Figure 4.3. The test applies symmetric 3-point bending to a beam specimen that has an insert film embedded in the mid-thickness. The specimen is aligned asymmetrically on the 3-point bending rig with respect to the insert film, with one end of the insert film being much closer to the loading pin than the other end, at a distance of $a_2$ and $a_1$, respectively. Also shown in the figure, $a_1$ is slightly longer than the half span length $L$. This is to ensure that compression from the loading or the supporting pins only acts on the starting film surfaces where the coefficient of friction should be very low. Such setup arrangement is expected to minimize the effect of friction on the measured delamination resistance.

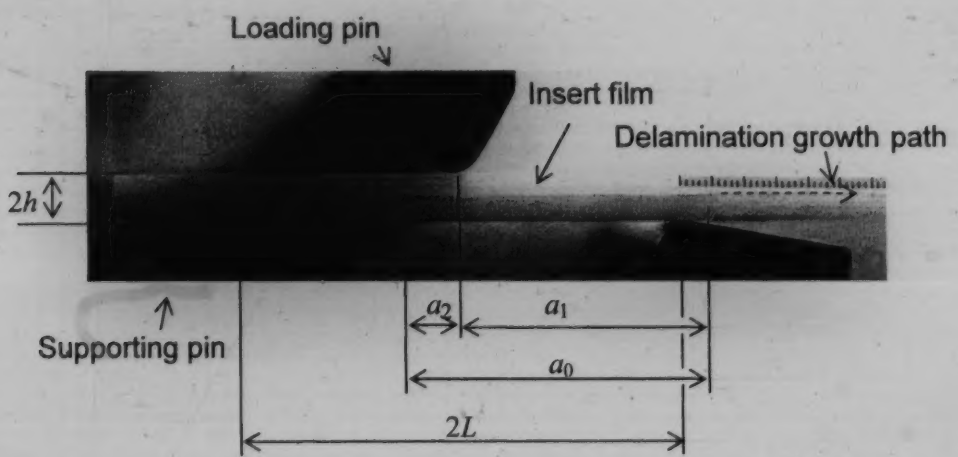


Figure 4.3 The INF test setup.

Delamination growth in the INF test is expected to be in the direction of $a_1$, that is, in the overhanging section outside the span length, in which the specimen is free from

any transverse loading. This, however, requires the INF specimen to have a sufficiently long overhanging section to provide the space for the delamination growth.

The INF test applies load under the displacement control, and records load, displacement and the change of $a_1$ during the delamination growth. The load-displacement curve is expected to be bilinear, with the transition point occurring when the delamination is initiated, as schematically presented in Figure 4.4.

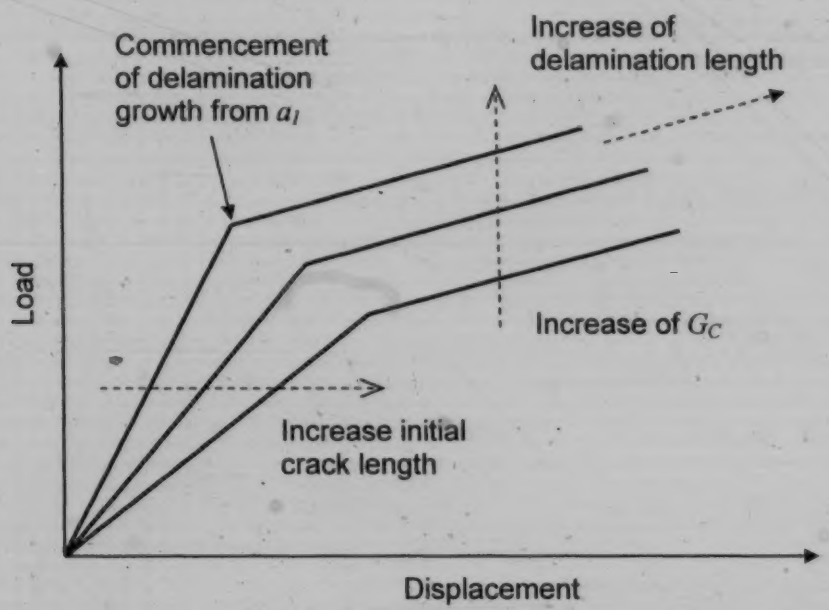


Figure 4.4 Schematic load-displacement curve of the INF test, with varied initial crack length and $G_C$.

### 4.2.2 Analysis on the INF test

*The energy release rate*

It should be noted that the setup shown in Figure 4.3 is identical to the configuration of scenario 3 in Figure 2.6. Hence, the compliance of the INF test can be determined using

Eq. (2.25c) and the $G$ expressions for delamination growth in the two directions, $G_{a1}$ and $G_{a2}$, using Eqs. (2.29-2.30). The total energy release rate with crack growth in both directions could be expressed as [41],

$$G^{INF} = \frac{da_1}{da_1 + da_2} G_{a1} + \frac{da_2}{da_1 + da_2} G_{a2} \tag{4.1}$$

The embedded starting defect in the INF specimen provides two directions for the delamination growth. In order to ensure that the delamination growth is always in the $a_1$ direction, i.e. from the right end of the insert film of Figure 4.3, the value of $G_{a1}$ (Eq. 2.29) has to be greater than $G_{a2}$ (Eq. 2.30), which requires the following condition to be met [41]:

$$L \le a_1 \le \frac{L + a_2}{L - a_2} L \tag{4.2}$$

The above condition allows the delamination growth solely in the $a_1$ direction for a length of $[L(L+a_2)/(L-a_2)-a_1]$ before the start of the crack growth in the $a_2$ direction. In other words, under the condition of Eq. (4.2), crack growth never occurs in the $a_2$ direction. Therefore Eq. (4.1) becomes

$$G^{INF} = G_{a1} = \frac{9P^2}{64EB^2h^3(a_1 + a_2)^2}(a_2^2 - 2a_2L - L^2)^2 \tag{4.3}$$

Expressions for $G_{a1}$ and $G_{a2}$ can also be derived using the CTE analysis. Following the analysis given in Section 2.2.1.4, the concentrated forces at both crack fronts, $F_{C1}$ and $F_{C2}$, and the moments, $M_{C1}$ and $M_{C2}$, could be obtained as

$$F_{C1} = \frac{3P}{16hB(a_1 + a_2)}(a_2^2 - 2a_2L - L^2) \tag{4.5}$$

$$F_{C2} = \frac{3P}{16hB(a_1 + a_2)}(a_2^2 + L^2 - 2a_1L + 2a_1a_2) \tag{4.6}$$

$$M_{C1} = M_{C2} = 0 \tag{4.7}$$

Substituting Eqs. (4.5-4.7) to Eq. (2.63), it yields the same expressions of $G_{a1}$ and $G_{a2}$ as Eqs. (2.29-2.30).

*Fracture mode*

In addition to deriving the energy release rate, the CTE analysis can also determine the mode mixing ratio for the delamination growth in the INF specimen. Eqs. (4.5-4.7) indicate that the delamination crack in the INF specimen is subjected to concentrated forces $F_C$ only, which is the same condition as that for the 4ENF test [37]. Therefore, the fracture mode introduced in the INF test should be the same as that in the 4ENF test, and according to the analysis in Ref. [40] the two tests should be subjected to a pure shear mode of fracture. Therefore, the corresponding critical energy release rate in the INF test should represent $G_{IIC}$.

*Stability of delamination growth*

A stable crack growth requires the following conditions,

$$\begin{cases} G = G_C \\ dG/da \le dG_C/da \end{cases} \tag{4.8}$$

If $G_C$ is regarded as a constant, a negative value of $dG/da$ indicates stable delamination growth and a positive one unstable delamination growth. Using Eq. (4.3), it can easily be found that the value of $dG/da$ for the INF test is always negative under both testing conditions, thereby enabling the generation of unconditionally stable delamination growth. This is because that crack growth under the displacement control should be more stable than that under the load control.

The stability for other mode II delamination tests is also assessed in the same way and the results are summarized in Table 4.1. The INF test is the only one that generates stable delamination growth under load control.

Under displacement control, d$G$/d$a$ of all tests could be negative if the crack length is properly chosen. The reason for the unstable crack growth in the ENF and ELS tests could be attributed to the variation of $G_C$ (e.g. because of the inhomogeneity of material). For instance, for the ENF test subjected to constant displacement, $G$ values reach the maximum at $a/L$ = 0.7, but drops less than 5% at $a/L$ = 0.8 with the same displacement. On the other hand, experiments have shown that the variation of $G_C$ in mode II fracture can easily be as high as 50% [36]. Hence, the value of $dG/da$ could be greater than $dG_C/da$, resulting in unstable crack growth.

Table 4.1 Predicted stabilities in mode II delamination tests.

| | Displacement control | Load control |
|---|---|---|
| INF | Stable<br>$dG/da_1 < 0$ | Stable<br>$dG/da_1 < 0$ |
| 4ENF | Stable<br>$dG/da < 0$ | Unstable<br>$dG/da = 0$ |
| ELS | Conditionally stable<br>$dG/da \leq 0$ when $a/L \geq 0.55$ | Unstable<br>$dG/da > 0$ |
| ENF | Conditionally stable<br>$dG/da \leq 0$ when $a/L \geq 0.7$ | Unstable<br>$dG/da > 0$ |

*Load-displacement curve*

The load $P$ and the corresponding displacement $\delta$ of the INF test can be expressed explicitly as a function of critical energy release rate $G_C$ and $a_1$. The expression for $P$ is simply through the rearrangement of Eq. (4.3) with $G_C$ replacing $G^{INF}$:

$$P = \frac{8(a_1 + a_2)B\sqrt{E_1 h^3 G_C}}{3(L^2 + 2La_2 - a_2^2)} \tag{4.9}$$

The expression for the displacement is obtained by converting the above expression using Eq. (2.25c):

$$\delta = \frac{\sqrt{G_C}(20L^3 a_1 + 36a_2 L^2 a_1 - 36La_2^2 a_1 + 12a_2^3 a_1 - 16a_2 L^3 - 9L^4 + 18a_2^2 L^2 + 3a_2^4)}{12(L^2 + 2La_2 - a_2^2)\sqrt{E_1 h^3}} \tag{4.10}$$

The above two equations suggest that both $P$ and $\delta$ are linear functions of $a_1$.

Using Eq. (2.25c) for the relationship between $P$ and $\delta$ before the onset of delamination and Eqs. (4.9-4.10) after, the trend of the change for the load-displacement curve from the INF test with respect to the increase of $a_1$ and $G_C$ is schematically illustrated in Figure 4.4. Note that the curves in the figure are constructed based on the assumption of stress-free fracture surfaces that do not impose any barrier to the delamination growth. With this assumption, the slope of the $P$-$\delta$ curve during the delamination growth should be a constant for a given $G_C$ value.

*Delamination growth rate*

Since $\delta$ is a linear function of $a_1$, with $a_2$ and $G_C$ being constant, the time derivative of Eq. (4.10) suggests that the delamination growth rate $\dot{a}$ is a linear function of the crosshead speed $\dot{\delta}$, that is,

$$\dot{a}_1 = \frac{12(L^2 + 2La_2 - a_2^2)\sqrt{Eh^3}}{\sqrt{G_C}(20L^3 + 36a_2 L^2 - 36La_2^2 + 12a_2^3)}\dot{\delta} \tag{4.11}$$

Therefore, by controlling the cross-head speed $\dot{\delta}$, the INF test can be used to reveal the effect of crack growth speed on the delamination resistance.

### 4.2.3 Experimental details

Based on the above analysis, a test program was conducted to measure mode II delamination resistance in fiber composites.

*INF specimens*

The specimens had isophthalic polyester as the matrix, and unidirectional weft glass fiber fabric of 305 g/m$^2$ (9-oz/yd$^2$) as the reinforcement, provided by Triple M Fiberglass and ZCL Composites in Edmonton, respectively. A wet hand-lay-up technique was used to fabricate flat composite panels of 220×220 mm$^2$, with fiber lay-up of $[0_{10}/F/0_{10}]$ where F represents an aluminum insert film of 25 μm thick and 42 mm long, acting as a starting defect for the delamination growth. Stitching threads, shown in Figure 4.5, that held the fiber bundles together were removed in the middle 4 layers, i.e. from 9$^{th}$ to 12$^{th}$ layers, to reduce mechanical interlocking between the fracture surfaces during the delamination growth. These panels were cured at room temperature for 24 hours and then post-cured at 70°C for 20 hours to accelerate and complete the resin curing, resulting in a nominal thickness of 6.2 mm and fiber volume fraction of 38%. Strip specimens of 20 mm wide were then machined from the panels for testing, with 0-degree fiber aligned in the longitudinal direction.

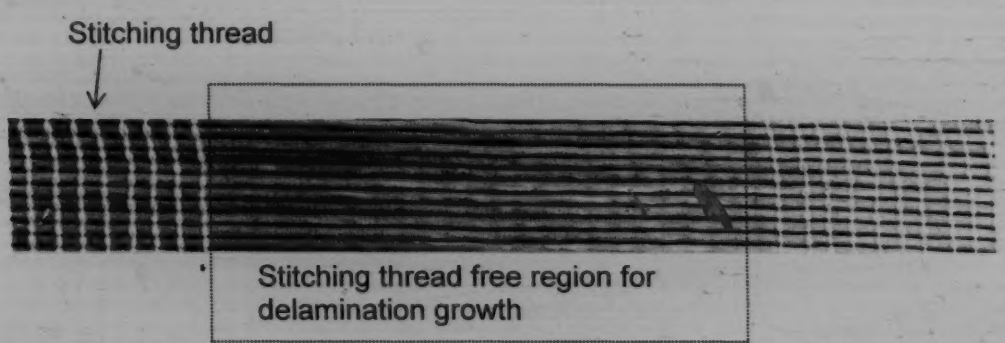


Figure 4.5 Glass fiber with/without stitching threads.

*Delamination test setup and procedure*

INF tests were conducted using an INSTRON® Universal Testing Machine. The crosshead speed ($\dot{\delta}$) was 0.254 mm/min. The half span length, $L$, for the INF tests was 30 mm. The load was recorded using a load-cell attached to the central loading pin. The displacement was determined based on the cross-head speed and the loading time. Both loading and supporting pins had diameter of 5.08 mm. Values of $a_1$ and $a_2$ in Figure 4.3 were chosen to be 30 and 12 mm, respectively, which based on Eq. (4.2) allowed delamination growth for a distance of 40 mm in the $a_1$ direction before any delamination growth could occur in the $a_2$ direction.

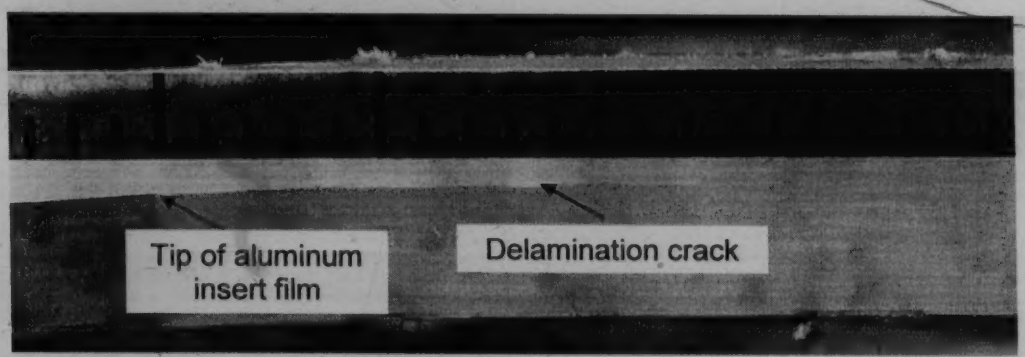


Figure 4.6 Photograph of an INF specimen taken during testing.

Taking advantage of the translucent appearance of the specimen, crack propagation was recorded using a digital camera (Nikon D70) at a sampling rate of 0.2 Hz, i.e. 1 picture for every 5 seconds. As shown in Figure 4.6, a paper strip with 1-mm marks was attached to the specimen edge so the crack growth length could be read directly from the photographs.

*Observation*

A typical load-displacement curve from the INF test and the corresponding change of crack growth are presented in Figure 4.7. The figure shows that a tiny

delamination crack was initiated at displacement of about 1.25 mm, which is equivalent to a loading level of about 2000 N. Delamination growth at this stage was found to be very slow and its occurrence barely changed the slope of the load-displacement curve. The crack growth speed increased significantly, at the displacement corresponding to 1.7 mm. The fast delamination growth lasted for about 0.2 mm of the cross-head displacement, as marked by two dash lines in Figure 4.7 and generated a peak on the load-displacement curve (point A). Further increase of the cross-head displacement resulted in a reduced delamination growth speed that remained relatively constant till the end of the test, with total delamination growth length of around 30 mm. It should be noted that all specimens showed delamination growth that occurred in the $a_1$ direction only, and the load-displacement curves were very reproducible.

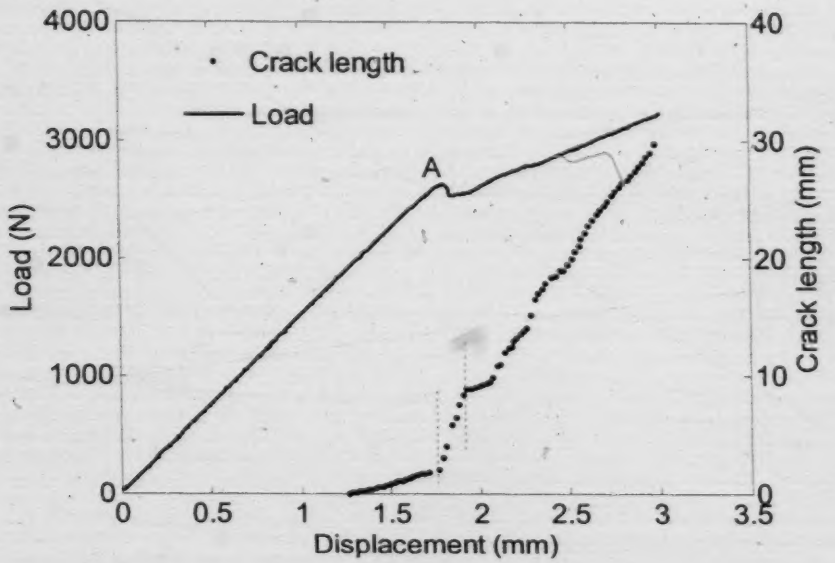


Figure 4.7 The INF test results, load-displacement curve and crack growth against displacement.

### 4.2.4 Data reduction methods

#### 4.2.4.1 Direct method

In Figure 4.8 two sets of straight lines are plotted with the load-displacement curve. The lines from the origin are the $P$-$\delta$ response constructed using Eqs. (4.9-4.10), with constant increment of $a_1$, $\Delta a_1$. For the other parameters on the right-hand side of Eqs. (4.9-4.10), $a_2$, $L$ and $h$ were measured prior to conducting the tests and $E$ determined using the linear part of the experimental load-displacement curve.

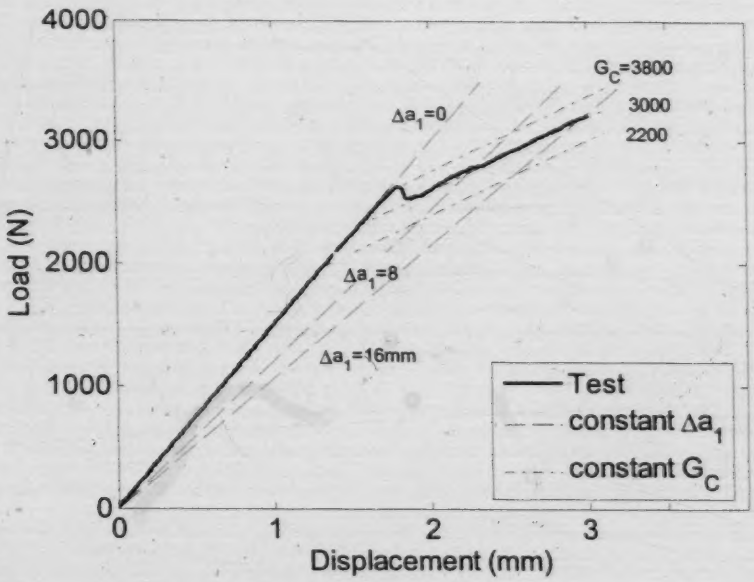


Figure 4.8 Determine $G_{IIC}$ by direct method.

The parallel lines are the $P$-$\delta$ response with constant $G_C$. The experimental load-displacement curve (the solid line in Figure 4.8) followed the straight line with constant crack length ($\Delta a_1$=0) first, and afterwards followed one of the parallel lines with $G_C$ = 3000 J/m$^2$. Each point on the load-displacement curve from the INF test has corresponding $\Delta a$ and $G_{IIC}$ values that could be determined from the lattice formed by the two sets of straight lines, or calculated using Eqs. (4.9-4.10) based on the load and

displacement values at that point. Plotting $G_{IIC}$ against $\Delta a$ directly calculated from Eqs. (4.9-4.10) yields an R-curve. The method itself is thus named *direct method* (DM).

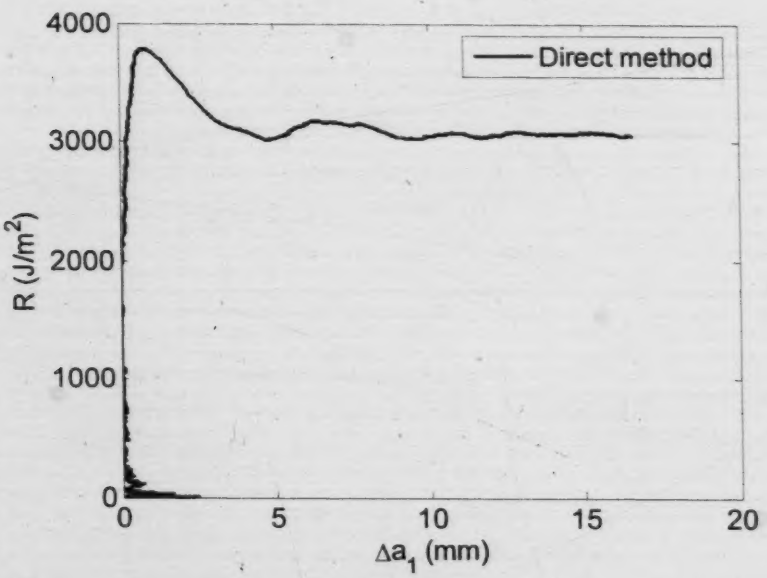


Figure 4.9 *R*-curve obtained by direct method.

Figure 4.9 shows the *R*-curve obtained by DM. This method could easily establish the relationship between $G_C$ and $\Delta a$ without measuring the crack length during the test. However, it was found that the maximum crack length (17 mm) in Figure 4.9 is shorter than the visual crack length (30 mm) shown in Figure 4.7. This difference is because the assumptions behind Eqs. (4.9-4.10) are not fully met, one of which requires the facture surface to be stress-free. In the INF specimens, bridging fibers were found entangling between the top and bottom fracture surfaces, as shown in Figure 4.10, which may generate significant shear force interaction, thereby invalidating the analytical expressions. The bridging fibers were known to exist and were studied extensively in mode I DCB test [42-44], but they were not recognized as an issue in mode II tests

probably because they were not visible in the mode II tests as much as in mode I test in which the opening cracks was generated.

Besides bridging fibers, the mode II fracture surfaces contained matrix hackles, as shown in Figure 4.1(b), which is another factor that may introduce interaction between the fracture surfaces. Figure 4.11 is a side view of the matrix hackles on the fracture surfaces. In mode II fracture, shear force generated by the zigzag-shaped hackles is expected to introduce resistance to crack growth because they interlock each other during the sliding motion. But the hackles may not generate any resistance when the fracture surfaces separate in their normal directions (mode I fracture).

Consequently, due to the shear force induced by bridging fibers and matrix hackles, the compliance did not increase as much as it should according to Eqs. (4.9-4.10), or equivalently, the calculated crack length by the DM is underestimated.

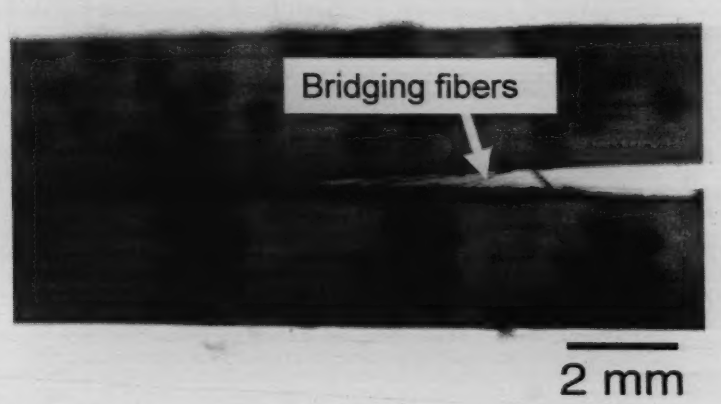


Figure 4.10 Photograph of a post-tested INF specimen showing bridging fibers between the fracture surfaces.

Figure 4.11 Side view of the matrix hackles on the crack surfaces from SEM.

4.2.4.2 Direct method with final crack length correction

Because of the substantial difference between the measured crack length and that determined from DM, the *R*-curve in Figure 4.9 cannot be correct. Therefore, a strategy was developed to determine the correct R-curve by horizontally stretching the plot in Figure 4.9 to the final visual crack length of 30 mm and compressing the curve vertically with the area underneath unchanged. Mathematically this procedure is a mapping process using the following formulas,

$$\begin{cases} \Delta a_1 \rightarrow \Delta a_1 \cdot k \\ R \rightarrow R \cdot k^{-1} \end{cases} \tag{4.12}$$

where $k$ is the ratio of the maximum visual crack on the INF specimen to the maximum crack length calculated using Eqs. (4.9-4.10). Using this method for building *R*-curve is

named *direct method with correction* (DMC). The *R*-curve from the DMC is presented in Figure 4.12. It keeps all peaks and valleys of the R-curve generated by DM, but with $1/k$ times the original magnitude.

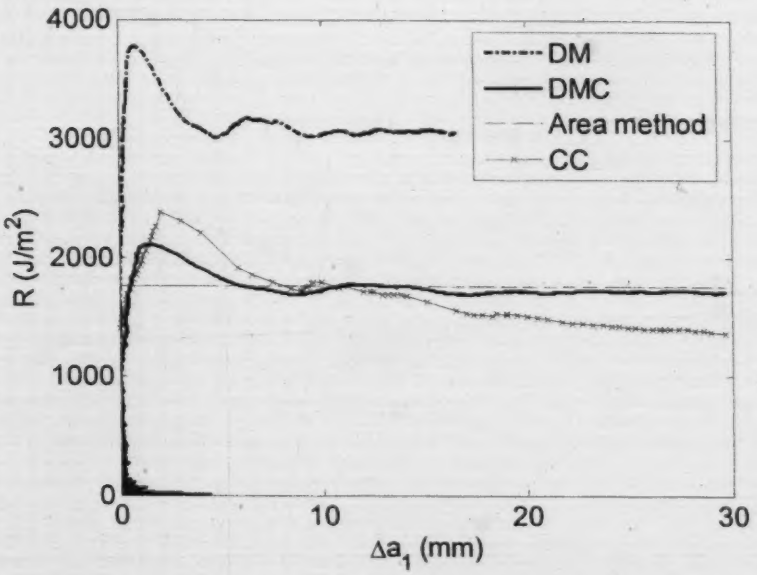


Figure 4.12 Comparison of R-curves by DM, DMC, CC method and area method.

DMC is actually based on the principle of conservation of energy, as the areas below the *R*-curves by the DMC and the DM in Figure 4.12 represent the total energy consumed by crack growth. Eq. (4.12) also assumes that the calculated crack length is proportional to the visual crack length, which is to be verified in Figure 4.13. Figure 4.13 presents the calculated crack length against the visual crack length, marked by "×", which shows good linearity. The curve of the calculated crack length after the mapping versus visual crack length, marked by "·", appears nearly diagonally, showing that the crack length after the mapping and the measured crack length are approximately the same.

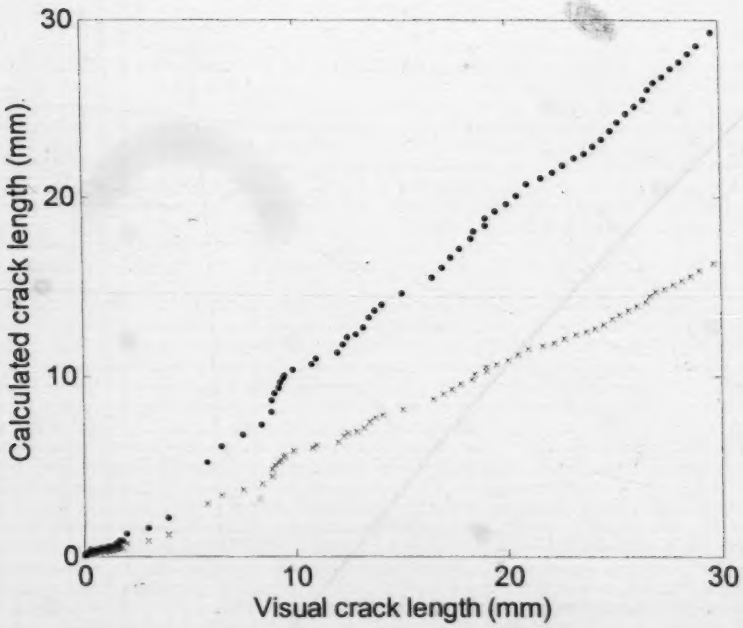


Figure 4.13 Calculated crack length versus visual crack length for verifying the linear mapping, "×" represent calculated crack lengths without mapping and "•" representing those with mapping.

4.2.4.3 Area method for the average $G_{IIC}$

Because of the stable crack growth and the slow loading rate, the kinetic energy in the INF test can be ignored. Thus, the area method [45] that assumes zero kinetic energy can be used to quantify the $G_C$ value using the following formula:

$$G_C = \frac{\Delta W - \Delta U}{\Delta A} \tag{4.13}$$

where $W$ is the external work, $U$ the strain energy, $\Delta A$ the increment of delamination area. When choosing $\Delta A$ as the total delaminated area and assuming that the system is linear elastic, Eq. (4.13) can be rewritten as:

$$G_C = \frac{\int_0^{\delta \max} P(\delta) d\delta - P|_{\delta \max} \delta_{\max}/2}{A} \tag{4.14}$$

where $\delta_{max}$ is the maximum displacement and $P|_{\delta max}$ its corresponding force. The average value of $G_C$ by this method is plotted as a horizontal line in Figure 4.12. The area method is essentially identical to the average value of the *R*-curve by DMC, because both are based on the load-displacement curve and the energy conservation.

4.2.4.4 Compliance calibration method

Compliance calibration (CC) method has been widely used in 4ENF and ELS tests to generate *R*-curves. CC method is based on Eq. (2.2), but not using the analytical expression of d*C*/d*a*. Instead, this derivative is obtained by curve-fitting of the experimentally determined *C* and *a*, thus requiring the in-situ crack length measurement. CC method was also adopted in the INF test, as discussed in the following.

The expression of the compliance *C* for the INF test, Eq. (2.25c), could be rewritten as

$$C = C_0 + \frac{C_1}{a_1 + a_2} \tag{4.15}$$

with $C_0$ and $C_1$ being constants. Substituting Eq. (4.15) into Eq. (2.2) yields

$$G = -\frac{P(a_1)^2}{2w}\frac{C_1}{(a_1 + a_2)^2} \tag{4.16}$$

The CC method for INF builds R-curve using the above equation, where $a_1$ and $P(a_1)$ are the measured crack length and force, respectively, and $C_1$ is to be determined by fitting the plot of *C* versus $(a_1 + a_2)^{-1}$ with a straight line, based on Eq. (4.15).

The *R*-curve established by the CC method is also plotted in Figure 4.12. This *R*-curve however has a declining trend which is different from the one by the DMC that shows nearly constant resistance with the increase of crack length *a*. To investigate the

reason for the decreasing trend of the R-curve, the linear curve fitting for compliance is presented in Figure 4.14. Though majority of the data points do not scatter much from the fitting curve, the data in the range of small and large crack lengths, as circled in the figure, deviate considerably from the straight line. This deviation is because the compliance may not inherently be a linear function of $(a_1 + a_2)^{-1}$ due to the shear force interaction on the crack surfaces, as mentioned in Section 4.2.3.1. As a result, the CC method may not be a desirable method to derive $G$ of the INF test.

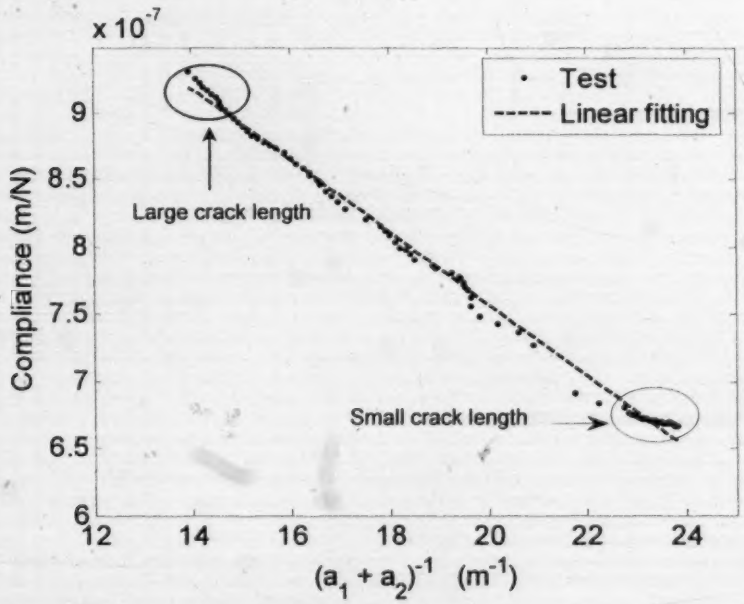


Figure 4.14 Linear curve fitting for the INF test.

4.2.4.5 Discussions

Four data reduction methods are discussed for extracting $G_{IIC}$ from the INF test. The DM (Section 4.2.4.1) is the simplest and most straightforward one. It generates the $R$-curve based on the load-displacement curve and has no requirement for the history of the crack growth length. However, it overestimates the mode II delamination resistance because in

the glass fiber composites material used in this study, the interaction between the fracture surfaces is so significant that the stiffness does not drop as much as it is expected from the analytical expressions. For carbon fiber composites which are the materials most commonly used in the study of the 4ENF test, it is possible that fracture surfaces do not have as much interaction as the glass fiber composites, since this phenomenon was never reported in the literature. If this is true, the calculated crack length for carbon fiber specimens should be consistent with the measured crack length in the 4ENF test thus the DM should work well. However, to our knowledge, the DM has never been applied to the 4ENF test results.

DMC corrects the *R*-curve obtained by the DM using the final true crack length, based on the energy conservation principle. In this study, visual crack length is regarded as the true crack length. For opaque composites, such as carbon fiber composites, visual location of the crack tip may not be obvious. But there are many other ways to accurately measure the final crack length, such as X-ray [46] or ultrasonic C-scan [47]. The *R*-curve by DMC, as shown in Figure 4.12, gives the $G_{IIC}$ over 2100 J/m$^2$ at small crack length ($\Delta a_1 < 3$mm) but quickly drops to 1700 J/m$^2$ at $\Delta a_1$=6mm and oscillates slightly around this value for the rest of the crack propagation. The high $G_{IIC}$ at the beginning might be due to thick aluminum foil (25 μm) which was much thicker than the suggested thickness of 8 μm [48] to avoid the initially high $G_{IIC}$ value.

The CC method is more complicated than the DM and DMC. The former needs in-situ crack length measurement. For semi-transparent specimens, it is possible to use the change of translucency to monitor of the crack growth during the test. But for opaque materials, tests have to be run in a repetitive loading-unloading mode to monitor the

crack growth [49]. This is because the crack length needs to be measured using ultrasonic scan, X-ray or microscopy, thus requiring removal of the specimen from the test fixture. Such measurement procedure could be tedious and time-consuming. The loading-unloading manner may also complicate the test, such as misalignment of specimen on the fixture or possible damage in the specimen by cyclic loading, thus creating additional problems.

Area method provides the average $G_{IIC}$ value of the *R*-curve, and requires the same information as that for DMC, i.e. the load-displacement curve and final delamination length. The average $G_{IIC}$ value will be used as the reference to evaluate the performance of composites' delamination resistance in the next section.

### 4.2.5 The effect of fiber volume fraction on $G_{IIC}$

#### 4.2.5.1 Testing details

*INF test*

The INF specimens used in this study are unidirectional *glass/epoxy* composites that are comprised of 300 g/m$^2$ layers of E-glass fibers impregnated in epoxy by hand lay-up. The initial crack at the mid-thickness was built by inserting an *8 μm polypropylene film* during the fabrication. The glass fiber layers contain 90-degree polyester stitching threads every 15 mm in glass fiber direction, as shown in Figure 4.15. Note that the specimens discussed here are different from those in Section 4.2.3, where the specimen had the matrix of polyester and glass fiber with stitching threads removed in the crack propagation region. Also note that stitching threads used to maintain the

integrity of the unidirectional glass fibers are often included in the glass fiber composites in real applications to facilitate easy handling during the manufacturing.

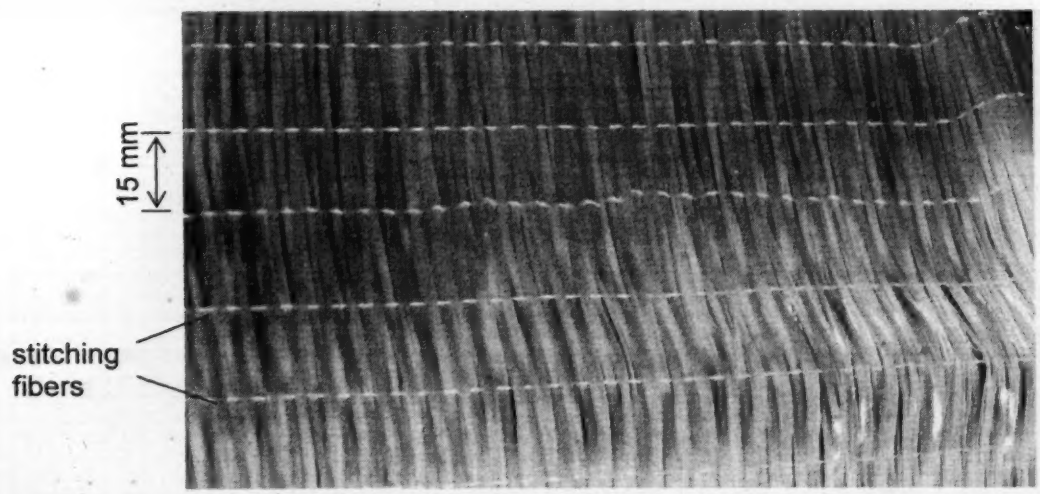


Figure 4.15 Glass fiber preform with stitching fibers.

The specifications of the INF specimens are listed in Table 4.2. The name of each type of coupon specimens contains the information of the number of plies and crack length. For example, "P30-*a*42-L30" means that it contains 30 layers with initial crack length $a_0$=42mm and half span length $L$=30mm. All quantities listed in Table 4.2 are nominal and the true values for every single specimen will be measured before conducting the test.

The tests were carried out using Quasar 100 universal testing machine under displacement control at a crosshead speed of 1 mm/min. The specimen was unloaded at the same crosshead speed after the visual crack had grown over 20 mm. Both loading pin and supporting pins had a diameter of 5.08 mm.

Table 4.2 The specifications of the INF specimens and test setup

| Name | Number of layers | $2h$ (mm) | $a_0$ ($a_2$,$a_1$) (mm) | $L$ (mm) | $w$ (mm) | Nominal fiber content (%) |
|---|---|---|---|---|---|---|
| P30-*a*42-L30 | 30 | 7.5 | 42(8,34) | 30 | 20 | 46 |
| P30-*a*47-L35 | | 7.5 | 47(8,39) | 35 | 20 | 46 |
| P30-*a*47-L40 | | 7.5 | 47 (7,40) | 40 | 20 | 46 |
| P30-*a*52-L35 | | 7.5 | 52(8,44) | 35 | 20 | 46 |
| P30-*a*52-L40 | | 7.5 | 52(8,44) | 40 | 20 | 46 |
| P30-*a*57-L40 | | 7.5 | 57(10,47) | 40 | 20 | 46 |
| P24-*a*47-L35 | 24 | 7.5 | 47(8,39) | 35 | 20 | 37 |
| P36-*a*46-L35 | 36 | 7.5 | 47(8,39) | 35 | 20 | 55 |

Typical load-displacement and crack length history curves are plotted in Figure 4.16. It shows that there were two slow crack growth stages at $\Delta a$ = 7 and 22 mm. This is due to the stitching threads which worked as pins holding together the adjacent two layers after the delamination crack front had passed through the position. Figure 4.17 shows two scanning electron micrographs that are examples of how a stitching thread prevents the sliding motion. Figure 4.17(a) was taken from the edge of a specimen. The end of a stitching thread is perpendicular to the picture. Figure 4.17(b) shows fracture surface where a stitching thread bundle is in the vertical direction. The stitching thread could incur massive shear force to prohibit the relative sliding motion of the upper and lower crack surfaces. Therefore, higher driving force was needed for the crack to bypass the stitching thread than that in the stitching-thread-free region. Consequently, a bump was created on the load-displacement curve, as shown in Figure 4.16. The corresponding *R*-curves by the DM and DMC are plotted in Figure 4.18, compared to the average $G_{IIC}$ value from the area method. The one by DMC shows a peak at crack length of 7 mm,

where the crack front encountered a stitching thread, and a valley at crack length of about 20 mm just before the interference with the next stitching thread.

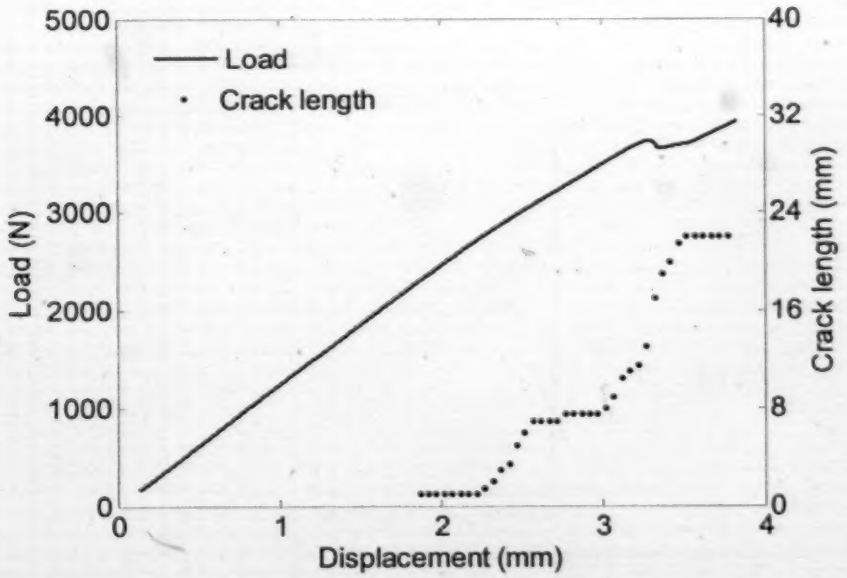


Figure 4.16 Typical load-displacement curve and crack length history of the INF test with stitching threads on the delamination growth path.

(a)

(b)

Figure 4.17 SEM pictures of stitching fiber: (a) side view and (b) front view.

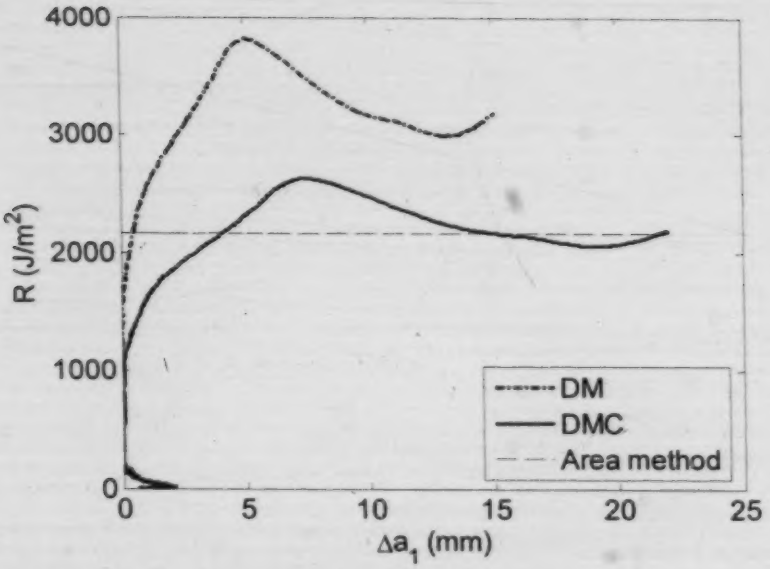


Figure 4.18 *R*-curves obtained by DM, DMC and area method.

*4ENF test*

4ENF tests were carried out to provide crosscheck of the INF test results using specimens of the same materials. The 4ENF test setup configures followed those in Ref. [50]. Similar to the INF test, load-displacement curve shows oscillation at the crack propagation stage, as shown in Figure 4.19. The shear force interaction was also found on the crack surfaces of the 4ENF specimen, due to the stitching fibers, bridging fibers and matrix hackles. Thus, instead of using CC method, area method, the DM and DMC were used for the average $G_{IIC}$ and *R*-curve. Figure 4.20 shows that R-curves by the DM and DMC have similar peaks and valleys as those from the INF test (see Figure 4.18).

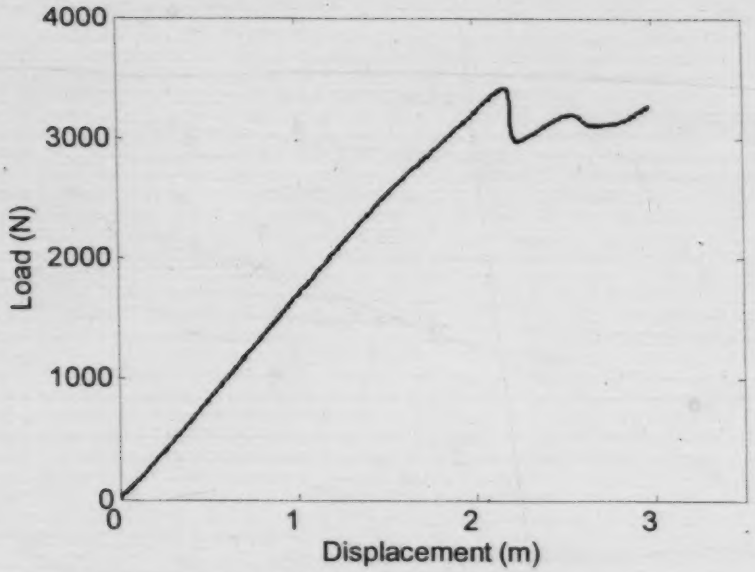


Figure 4.19 Typical load-displacement curve of 4ENF test.

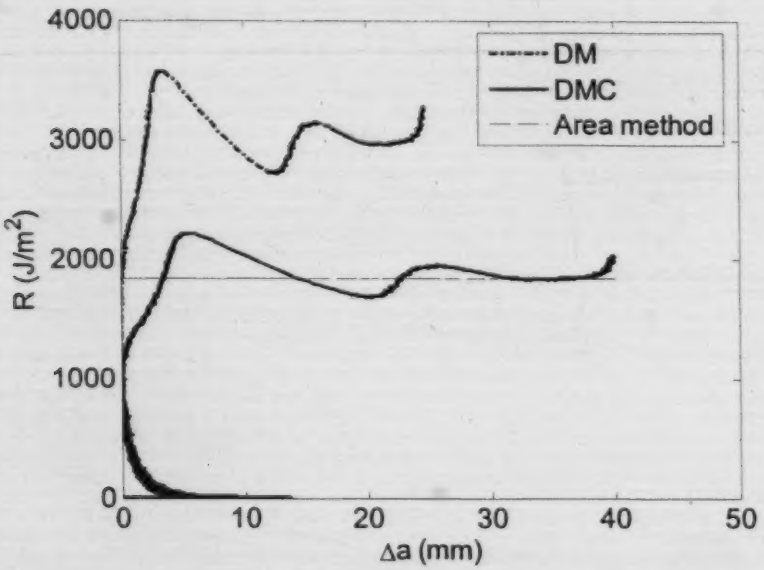


Figure 4.20 Typical *R*-curves built by the DM and DMC base on the 4ENF test.

4.2.5.2 Results and discussion

Figure 4.21 plots all average $G_{IIC}$ values by area method from the INF and 4ENF tests with respect to the fiber volume fraction that was determined based on the number of plies and the thickness of each specimen. Though the nominal fiber volume fraction was 37%, 46% or 57%, the true fiber content varies from 38% to 54% due to the scattering of specimen thickness. The figure shows that fiber content has a strong influence on $G_{IIC}$, that is, the higher the fiber content the lower the $G_{IIC}$ value. The mean $G_{IIC}$ value for specimens of low fiber content, with 24 layers, is 40% higher than those with high fiber content, with 36 layers. This trend is probably because more energy is required for delamination propagation by breaking a relatively thicker interfacial resin-rich region in specimens of low fiber content. Figure 4.21 also shows the data points from the 4ENF test using solid circles. These data are mingled with the INF data points, indicating a good correlation between these two types of tests.

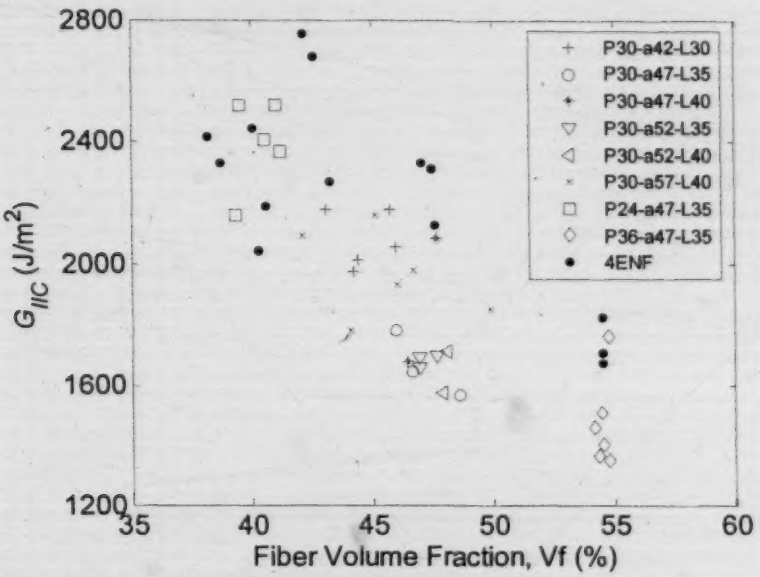


Figure 4.21 Average $G_{IIC}$ versus fiber volume fraction.

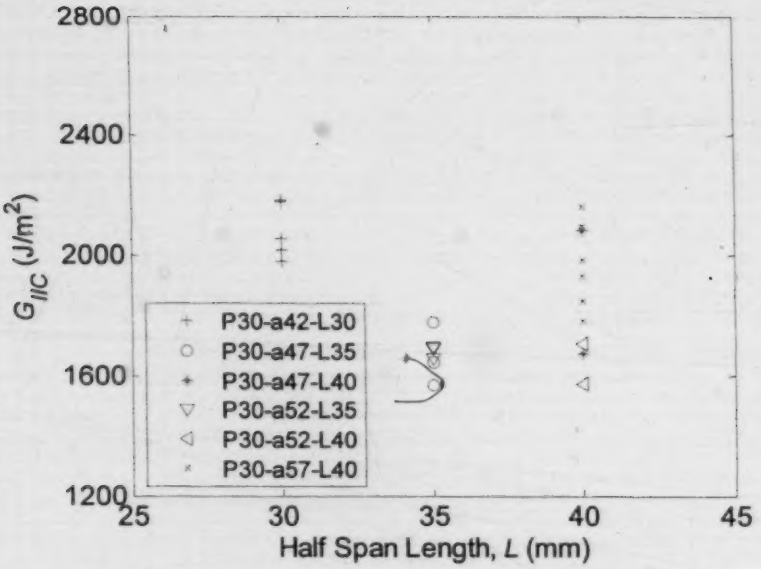


Figure 4.22 Average $G_{IIC}$ versus half span length, $L$.

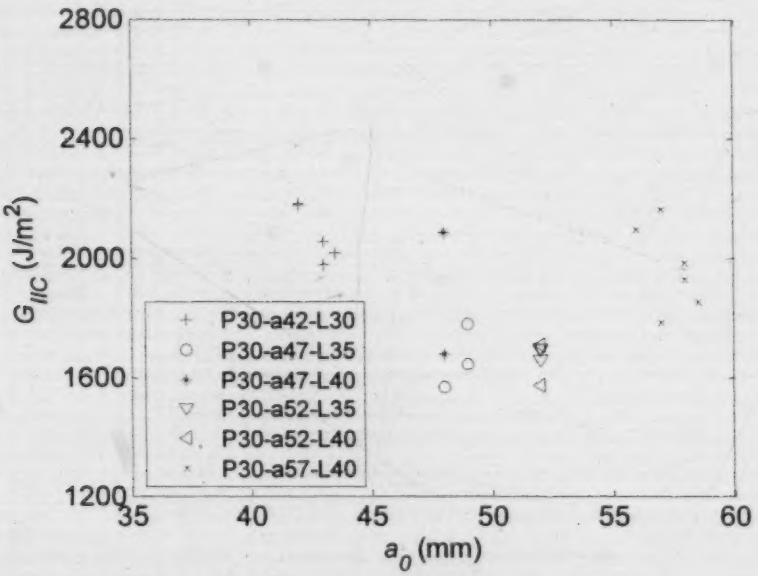


Figure 4.23 Average $G_{IIC}$ versus initial crack length, $a_0$.

In Figures 4.22 and 4.23, $G_{IIC}$ for specimens with 30 fiber layers is plotted against the initial crack length and half span length, respectively. Results do not show a clear

trend of $G_{IIC}$ as a function of $L$ or $a_0$, suggesting that the $G_{IIC}$ values are irrelevant to the test configurations used in the study.

## 4.3 Beam test

### 4.3.1 Introduction to the beam test

"Beam test" [29, 38-40] is a test method originally designed to quantify delamination resistance between fiber layers with different orientations. The Beam test adopts 3-point bending as the loading mode. Specimens for the beam test contain one 90 degree fiber layer with all the other layers aligned in the 0-degree direction, such as $[0_{12}/90_1/0_{12}]$.

The Beam test usually has an unstable crack growth, making it impossible to generate an $R$-curve. Therefore, Beam test can only give one average $G_{IIC}$ value, based on the area method (see Section 4.2.4.5). The unstable crack growth also causes specimen vibration, thereby introducing kinetic energy to the fracture process which may invalidate the area measured for the calculation of $G_{IIC}$. A remedy will be introduced to correct the error on the average $G_{IIC}$ caused by the specimen vibration.

Despite the above disadvantages, the Beam test could generate delamination without any additional damages [29, 38-40], such as indentation around the loading point or fiber buckling. Compared to other types of delamination tests, such as the 4ENF and INF tests, the Beam test generates delamination without a pre-existing crack. Thus, the Beam test can be used to verify the criteria for delamination growth as well as delamination initiation in the fiber composites.

### 4.3.2 Test details and results

The specimens were made by similar material and technique as those for the INF specimen described in Section 4.2.3. However, instead of having an insert film acting as initial crack, the Beam test specimens have a 90-degree fiber layer in the middle of a stack of 24 0-dgeree fiber layers, i.e. $[0_{12}/90_1/0_{12}]$. The nominal thickness of the specimens was 6.2 mm and the fiber volume fraction 45%.

Beam tests were conducted using an INSTRON® Universal Testing Machine. Span lengths used for the testing ranged from 30 to 60 mm at an increment of 5 mm. Diameter of the loading and supporting pins were 20.5 and 5.08 mm, respectively.

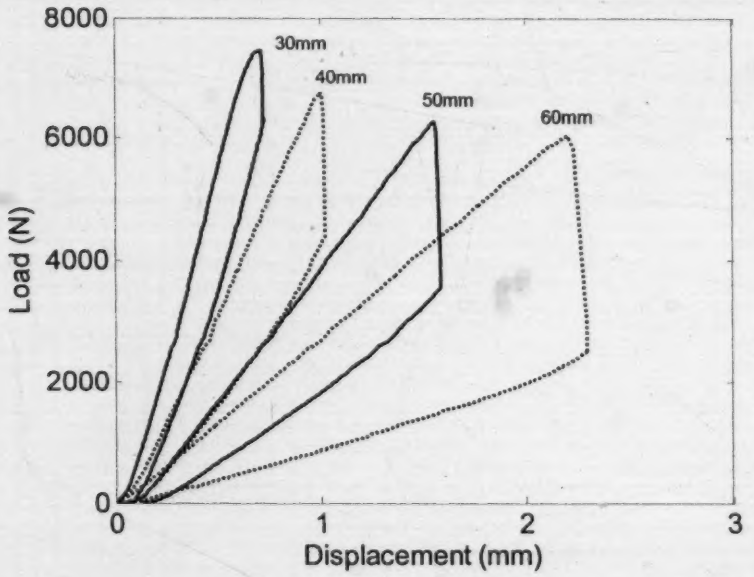


Figure 4.24 Typical load displacement curves of the Beam test with span length 30, 40, 50 and 60 mm.

Typical load-displacement curves of the Beam test for various span lengths are presented in Figure 4.24. The specimen of the Beam test was loaded under displacement control at a crosshead speed of 1.27 mm/min. When displacement is big enough, matrix

cracking is initiated within the 90-degree insert layer, which leads to delamination in the adjacent interlaminar regions. The delamination growth in the beam test is very fast, completed almost at constant deflection, and after that the specimen is unloaded immediately.

Figure 4.25 Matrix cracking (pointed by a white arrow) and delamination (black arrows) in a beam specimen.

An example of the Beam test is given in Figure 4.25 in which the white arrow indicates the location where the delamination was initiated, in this case, from a matrix cracking within the 90-degree layer. The delamination grew in both directions, one to the left passing under the central loading point, and the other to the right passing over the support, as pointed out by black arrows. The delamination area was measured from specimen surface, as the delamination incurred a significant change of the translucency of the specimen when viewed from the specimen surface, as shown in Figure 4.26.

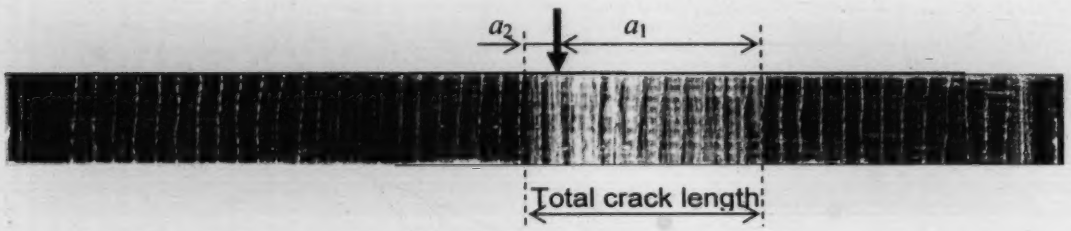


Figure 4.26 Crack length and location measurement.

Table 4.3 summarizes results of the Beam tests. The second column lists the average maximum force, $P_{max}$, on specimens with the same span length. Values of $P_{max}$

decrease with the increase of the span length, but it has a lower limit about 6000 N. The lower limit is actually related to the material shear strength, which will be further discussed in Chapter 6. The total delamination crack length, listed in column 3, increases more than 5 times from 17.3 mm for 30 mm span length to 96 mm for 60 mm span length. Location of the crack is measured by the distance of the crack tips to the loading pin, denoted as $a_1$ and $a_2$, as listed in the 4$^{th}$ and 5$^{th}$ columns of Table 4.3. Chapter 5 will give explanations for the length and location of the crack in the Beam test. The last column lists the $G_C$ values determined by the area method. As mentioned in Section 4.2.4.5, the area method assumes no kinetic energy involved in the fracture process. The following section will demonstrate how to experimentally quantify kinetic energy to correct the $G_C$ value.

Table 4.3 Results the Beam test with varied span lengths.

| $2L$ (mm) (Number) | $P_{max}$ (kN) (std. dev) | Total crack length (mm) (std. dev) | $a_2$ (mm) (std. dev.) | $a_1$ (mm) (std. dev.) | $G_C$ (J/m$^2$) (std. dev) |
|---|---|---|---|---|---|
| 30 (4) | 7.3 (0.32) | 17.3 (0.5) | 0 (0.0) | 2.3 (0.5) | 2263(173) |
| 35 (5) | 6.8 (0.17) | 22.6 (1.6) | 0.6 (0.5) | 4.5 (1.7) | 2279(214) |
| 40 (4) | 6.6 (0.30) | 30.0 (4.5) | 1.25 (0.5) | 8.8 (5.0) | 2431(207) |
| 45 (5) | 6.0 (0.48) | 34.0 (4.4) | 2.2 (1.3) | 9.3 (5.1) | 2395(298) |
| 50 (5) | 6.0 (0.32) | 42.5 (6.1) | 3.3 (0.9) | 14.3 (6.8) | 2513(119) |
| 55 (4) | 6.0 (0.31) | 51.0 (2.3) | 3.7 (0.5) | 19.8 (2.6) | 2504(109) |
| 60 (5) | 6.0 (0.22) | 96.0 (9.2) | 8.6 (1.8) | 57.4 (10.7) | 2257(99) |

### 4.3.3 Vibration energy in the Beam test

The energy loss caused by the specimen vibration is considered, and assumed to be the major form of energy loss apart from that for the generation of the fracture surfaces. This assumption was based on the experimental observation that showed little indication of any other forms of energy loss being significantly involved in the Beam test. With this assumption, the vibration energy loss is measured, and then $G_C$ for delamination is corrected by excluding the vibration energy loss from the calculation. It is believed that this approach has improved accuracy of the measured $G_C$ value.

Specimen vibration after the start of the delamination is recorded using a high-speed camera (Redlake MotionPro™) at a speed of 5000 frames/sec. A cracking noise was generated when delamination occurred, which provided a clear signal for manually triggering the video camera to stop the recording. Therefore, the fracture process for a duration before the triggering was recorded. The images were then analysed using MiDAS® to determine the frequency and the amplitude of the specimen vibration, which were used to estimate the kinetic energy involved.

Figure 4.27 Photographs of the beam vibration: (a) beam deflection before delamination, and (b) beam deflection after delamination at the lowest position during vibration.

Figure 4.27 shows typical photographs recorded during the Beam test at the span length of 50 mm. Edge of the specimen in the figure is coated with a thin layer of liquid white and marked every 5 mm. Figure 4.27(a) was taken just before the delamination, and Figure 4.27(b) after the delamination with the left overhanging section at the maximum deflection in the vibration.

Figure 4.28 Vibration motion of the Beam test specimen.

Figure 4.28 demonstrates the vibration in the specimen due to the unstable delamination growth, which was created by contrasting the two photographs of Figure 4.27. The photograph in Figure 4.28 suggests that specimen vibration mainly occurred in the left over-hanging section, with the vibration root located around the left support. The amplitude and frequency of the specimen vibration were measured and later used to estimate the associated kinetic energy.

To estimate the kinetic energy associated with the specimen vibration, the following process is used. Firstly, it is assumed that for each point in the overhanging section the motion is in a harmonic mode. Thus, the displacement $w$ and velocity ($\dot{w}$) at each point of the overhanging section are expressed as:

$$w(x,t) = w_{\max}(x) \cdot \sin(2\pi f_r t) \tag{4.17}$$

$$\dot{w}(x,t) = w_{\max}(x) \cdot 2\pi f_r \cdot \cos(2\pi f_r t) \tag{4.18}$$

where $f_r$ is vibration frequency (measured experimentally), $x$ distance to the vibration root, $w_{\max}(x)$ amplitude of vibration at $x$, and $t$ time.

The maximum kinetic energy for the vibration motion ($U_K^{\max}$) is

$$U_K^{\max} = \int_0^l \frac{1}{2}\dot{w}_{\max}^2(x) A\rho\, dx = \int_0^l \frac{1}{2}\left[w_{\max}(x) 2\pi f_r\right]^2 A\rho\, dx \tag{4.19}$$

where $A$ is the cross-sectional area of the specimen, $l$ total length of the over-hanging section from the support, and $\rho$ the density of the specimen. The images taken by the high-speed video camera were used to identify the function $w_{\max}(x)$ that fit the deflection profile of the over-hanging section.

Figure 4.29 compares the motion of the overhanging section with a swing motion and a cantilever beam vibration motion of the same amplitude. The figure suggests that the motion profile obtained experimentally can be more closely represented by the simple swing motion than by the cantilever beam vibration. This is probably because in the simply supported bending condition, the root of the overhanging section is not rigidly restricted from the rotation. The small amplitude resulted in a close approximation of the vibration motion by the swing motion. This is supported by the frequency of the vibration that was measured to be around 450 Hz, while the natural frequency for the equivalent cantilever beam vibration should be 1760 Hz. Therefore, the swing motion was used to approximate the maximum amplitude at each point during the vibration, that is,

$$\left|\delta_{\max}(x)\right| \cong (B_V / l)x \tag{4.20}$$

where $B$ is half of the maximum displacement of the specimen tip during the vibration motion, as illustrated in Figure 4.29. As a result, $E_{\max}^K$ in Eq. (4.19) can be expressed as:

$$E_{\max}^K \cong \int_0^l \frac{1}{2}(B_V\, x/l)^2 (2\pi f)^2 A\rho\, dx = \frac{1}{6}(2\pi f B_V)^2 A\rho l \tag{4.21}$$

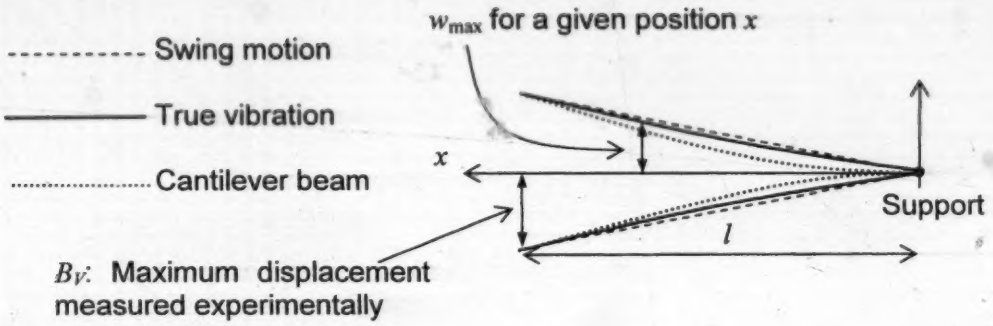


Figure 4.29 Schematic description of two modes of motion used to simulate the vibration.

An example for estimating the kinetic energy using the above approach is given here, based on the measured vibration frequency $f_r$ and $B_V$-to-$l$ ratio as 454 Hz and 0.0707, respectively. With known values of the cross-sectional area $A$, density $\rho$, and overhanging length $l$ (60.96 mm$^2$, $1.702\times10^{-3}$ g/mm$^3$ and 82 mm, respectively), the energy loss due to vibration, calculated using Eq. (4.21), is 0.169 J. This is about 12% of the total energy loss of 1.439 J. The average energy loss due to vibration, based on data from 5 specimens, is 12.7% of the total energy loss, with a standard deviation of 1.62%.

In a previous experimental study of the Beam test [40], using total energy loss to determine $G_C$ for delamination, it was found that the $G_C$ values were independent of the span length in the range from 30 to 60 mm. Since the true $G_C$ value should be independent of the span length, the fraction of energy loss for specimen vibration should also be independent of the span length, i.e. about 10% of the total energy loss. After excluding the energy loss for specimen vibration by subtracting it from the total energy loss, $G_C$ value for delamination should be around 2000 J/m$^2$, about 10% less than that reported in Ref. [40], 2200 J/m$^2$.

## 4.4 Concluding remarks

A new test method, named INF test, is proposed to quantify mode II delamination toughness of fiber-reinforced polymers, which generates unconditionally stable delamination growth. It was discovered that bridging fibers and matrix hackles on the crack surfaces incur shear force interaction and result in a lower compliance than the analytical prediction based on the same crack length. A data reduction method, DMC, was proposed to provide *R*-curve for delamination propagation. DMC requires the load-displacement curve and the final crack length to determine the R-curve. Compared to the commonly used CC method, DMC has fewer requirements on data acquisition, but provides more reliable R-curve.

By conducting a series of INF tests with variation in setup configurations and fiber volume fraction, $G_{IIC}$ was found to be irrelevant to the initial crack length or the span length of the fixture in the INF test, but could be significantly reduced by higher fiber volume fraction. The 4ENF tests were also employed to provide a crosscheck of the INF test results. Using the same data reduction methods (DMC and area methods), the 4ENF test generated similar *R*-curve and average $G_{IIC}$ value as those from the INF test, suggesting that both tests give essentially the same evaluation on the mode II delamination resistance.

The Beam test was also carried out. Since the Beam test always generated unstable crack growth, accompanied by specimen vibration, the kinetic energy loss due to vibration was estimated in order to correct the $G_C$ value determined from the area method. Although the $G_{IIC}$ values obtained from the Beam test may not be accurate, it is a good example to represent the delamination in fiber composites, compared to other types of

delamination tests. This is because the Beam test does not have an initial crack, consistent with most of real applications of fiber composites. Thus, the results include information such as delamination initiation location, final crack length and the critical load to generate delamination, which can be used as benchmarks to evaluate the simulation works, which will be presented in Chapters 5 and 6.

# Chapter 5 Analytical Prediction of Delamination Development in the Beam Test

## 5.1 Introduction

Crack growth is usually predicted by comparing the driving force of crack growth to a correlated threshold value. When the driving force is greater than the threshold, crack advances, otherwise arrests. The stress intensity factor ($K$) and the $J$-integral are often used as the driving forces in metallic materials, and correspondingly $K_C$ and $J_C$ are thresholds that govern the crack growth. In fiber reinforced composite materials, $G$ and $G_C$ are commonly adopted in the study of delamination. Therefore, this chapter will use these two parameters to predict the delamination development using analytical approaches.

The analytical approach is limited to problems that have explicit expression of $G$. However, the analytical solution is not always available especially for cracks with an irregular shape or subjected to complicated loading. As a result, the Beam test was selected for this study. Section 5.2 will discuss the delamination crack path in the Beam specimen, based on the criteria of the maximum energy release rate. Section 5.3 will predict the upper and lower bounds of the crack length through two approaches, one based on the energy release rate, and the other is based on the balance of the total energy. The latter is essentially the integral form of the energy release rate.

## 5.2 Prediction of delamination crack path

### 5.2.1 Criteria for crack growth direction

As mentioned in the previous chapter, delamination in the Beam specimen starts from the matrix cracking between the central loading pin and one of the supporting pins (see Figure 4.25), growing in the adjacent interlaminar regions in both directions. It was perceived that the delamination growth rates in the two directions might not be the same. Therefore, criteria are needed to determine the sequence of the delamination growth in the two directions. Two criteria are proposed here for this purpose.

Denoted by $da$, the total increment of the delamination crack length is

$$da = da_1 + da_2 = t \cdot da + (1-t) \cdot da \tag{5.1}$$

where $da_1$ is the growth of the delamination in the right direction (see Figure 4.25), $da_2$ the growth of the delamination in the left direction, and $t$ the ratio of $da_1$ to $da$ ($0 \le t \le 1$). Based on Eq. (2.2), the total energy release rate, $G_a$, is

$$G_a = \frac{P^2}{2B}\frac{dC}{da} = \frac{P^2}{2B}\left(\frac{\partial C}{\partial a_1}\frac{da_1}{da} + \frac{\partial C}{\partial a_2}\frac{da_2}{da}\right) = G_{a1} \cdot t + G_{a2} \cdot (1-t) \tag{5.2}$$

where $B$ is the width of the specimen, $G_{a1}$ and $G_{a2}$ are given by Eqs. (2.26-2.32) for different crack configurations. It should be noted that the presence of the 90-degree insert layer has been ignored in this analysis. This is because the 90° layer is located in the mid-thickness and has a very small fraction of the total thickness (1/25). As a result, it is not subjected to any significant level of stress and its presence should have little effect on the change of $G$.

The proposed 1st criterion is that the delamination grows in the direction that yields the maximum $G_a$ value. Based on this, in the case that $G_{a1} \neq G_{a2}$, Eq. (5.2) suggests

that $t$ should be equal to 1 or 0 to yield the maximum $G_a$. Therefore, the first criterion suggests that when $G_{a1} \neq G_{a2}$ delamination should grow in one direction only.

However, during the initial delamination growth from the matrix cracking, as described by Figure 5.1($a$), according to Eq. (2.26) $G_{a1}$ was found to be equal to $G_{a2}$. A 2nd criterion is proposed in this case to determine the ratio of the delamination growth length in the two directions.

The 2nd criterion states that the delamination growth should yield the maximum rate of increase of $G_a$ with respect to the total crack length $a$. That is, when $G_{a1} = G_{a2}$, delamination growth in either of the two directions should satisfy the following conditions:

$$\frac{d}{dt}(dG_a/da)=0 \text{ and } \frac{d^2}{dt^2}(dG_a/da)<0 \tag{5.3}$$

From Eq. (5.2), $dG_a/da$ in the above equations can be expressed as

$$\begin{aligned}\frac{dG_a}{da} &= \frac{d}{da}(G_{a1}\cdot t + G_{a2}\cdot(1-t)) \\ &= \frac{\partial G_{a1}}{\partial a_1}t^2 + (\frac{\partial G_{a2}}{\partial a_1}+\frac{\partial G_{a1}}{\partial a_2})(t-t^2)+\frac{\partial G_{a2}}{\partial a_2}(1-t)^2\end{aligned} \tag{5.4}$$

with $G_{a1}$ and $G_{a2}$ being given by Eqs. (2.26-2.32). Eq. (5.3) can be solved analytically to express $t$ as a function of $a_1$, $a_2$, $E$, etc.

### 5.2.2 Crack path in the Beam test

By applying the above criteria, i.e. primarily based on values of $G_{a1}$ and $G_{a2}$, and when $G_{a1} = G_{a2}$ on $dG_a/da$, delamination growth in the Beam test is expected to evolve in the following manner. Firstly, delamination is initiated from matrix cracking in one of the half-span sections. Since $G_{a1} = G_{a2}$ at this stage, delamination is expected to grow in both

directions, as shown in Figure 5.1(a). The two cracks in Figure 5.1(a) are named left crack and right crack, respectively, based on their positions relative to the initial matrix crack location. Using the $G$ expression for Scenario 1 of Figure 2.6, with $G_{a1} = G_{a2} = G$, Eq. (5.4) can be further simplified to be

$$\frac{dG_a}{da} = \frac{576\delta^2 h^3 E\mu^2 (a_1 - a_2)}{[8L^3\mu + 3(a_1 - a_2)^3\mu + 8Lh^2E]^3}\left[-3(a_1 - a_2)^3\mu + 4L^3\mu + 4Lh^2E\right] \qquad (5.5)$$

which suggests that $dG_a/da$ is also independent of $t$. Therefore, based on the two criteria, it is expected that the delamination growth in the two directions should have the same potential at this stage, until one of the delamination crack fronts reaches either the central loading point or the nearby support. After that, the 1st criterion suggests that further growth in the same direction does not occur until the other delamination crack front reaches the other point, S or C as depicted in Figure 5.1(b). This is based on $G_a$ values determined from Eqs. (2.27-2.28 and 2.31-2.32). As a result, delamination will grow beyond points C and S only after the crack is fully developed in the half-span section.

Delamination growth beyond the central loading point and the nearby support falls into scenario 3 of Figure 2.6(c). Based on the 2nd criterion, further delamination growth in the two directions must yield the maximum value of $dG_a/da$. Using Eqs. (5.3-5.4), with the definition of $t$ being

$$t(a_1, a_2, E, \mu, ...) = \frac{da_1}{da_2 + da_1} \qquad (5.6)$$

expression for $da_1 / da_2$ has been derived as a function of $a_1$, $a_2$, $E$, $\mu$, etc. The explicit expression of $da_1 / da_2$ is given below, after substituting $G_{a1}$ and $G_{a2}$ by expressions given in Eqs. (2.29-2.30) and force $P$ being replaced by $\delta/C$. That is, for delamination growth under the constant displacement,

$$\frac{da_1}{da_2} = \sum_{i=0}^{7} A_i L^i \Big/ \sum_{i=0}^{7} B_i L^i \tag{5.7}$$

where $A_0 = (48a_1^3a_2^4 + 54a_1^2a_2^5 + 15a_1a_2^6)\mu$,

$A_1 = (15a_2^6 - 126a_1^2a_2^4 + 18a_1a_2^5 - 192a_1^3a_2^3)\mu + (-16a_1^3a_2 - 24a_1^2a_2^2 - 8a_1a_2^3)h^2E$

$A_2 = (288a_1^3a_2^2 + 156a_1^2a_2^3 + 3a_2^4a_1)\mu + (-24a_1a_2^2 - 8a_2^3 + 16a_1^3)h^2E$

$A_3 = (-3a_2^4 - 256a_1^3a_2 - 348a_1^2a_2^2 - 140a_1a_2^3)\mu + (8a_1a_2 + 8a_1^2)h^2E$

$A_4 = (16a_2^3 + 129a_2^2a_1 + 112a_1^3 + 342a_1^2a_2)\mu - (8a_2 + 8a_1)h^2E$

$A_5 = (-142a_1^2 - 142a_2a_1 - 27a_2^2)\mu$

$A_6 = (16a_2 + 61a_1)\mu$

$A_7 = -9\mu$

$B_0 = (-6a_1a_2^6 + 3a_2^7)\mu$

$B_1 = (36a_1a_2^5 - 27a_2^6)\mu + (8a_1a_2^3 + 8a_2^4)h^2E$

$B_2 = (93a_2^5 - 42a_2^4a_1)\mu + (-24a_1^3 - 24a_1a_2^2)h^2E$

$B_3 = (-85a_2^4 - 40a_1a_2^3)\mu + (8a_1a_2 + 8a_2^2)h^2E$

$B_4 = (-87a_2^3 + 30a_2^2a_1)\mu + (8a_2 + 8a_1)h^2E$

$B_5 = (20a_1a_2 + 47a_2^2)\mu$

$B_6 = (2a_1 + 47a_2)\mu$

$B_7 = 9\mu$

With the initial conditions of $a_1 = L$ and $a_2 = 0$, the solution for Eq. (5.7) is

$$a_1 = L(L + a_2)/(L - a_2) \tag{5.8}$$

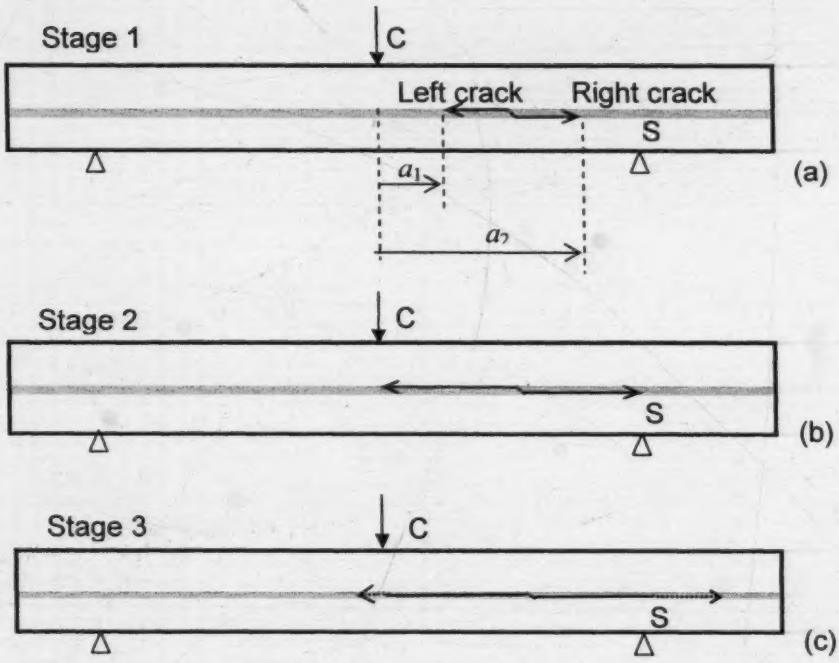


Figure 5.1 The process for delamination development in the Beam test: (a) stage 1, (b) stage 2, and (c) stage 3.

The above equation suggests that further delamination growth at stage 3 of Figure 5.1 should also occur in both directions, with delamination lengths $a_1$ and $a_2$ following the relationship governed by Eq. (5.8). This equation also suggests that the length of the right crack beyond the support should be more than twice of the left crack length beyond the central loading point, i.e. $(a_1 - L) > 2a_2$. By substituting Eq. (5.8) back into Eqs. (2.29-2.30), $G_{a1}$ and $G_{a2}$ were found to have the same value. Therefore, the crack growth in stage 3 is predicted to be simultaneous in both directions, but at different rates.

## 5.3 Prediction of the delamination crack length

### 5.3.1 Based on the energy release rate

Having identified the delamination crack growth pattern, the final crack length can be obtained simply by comparing $G_a$ to the material constant $G_C$ determined in the previous chapter. For example, Figure 5.2 presents a plot of $G$ as a function of the total crack length $a$, based on the crack path in Figure 5.1. $G$ values in the figure are calculated using the material properties listed in Table 5.1. Specimen geometry and loading conditions are the same as those given in the Beam test study (Section 4.3), with span length set at 50 mm. Since the load and the displacement follow a linear relationship prior to delamination growth, the displacement for the onset of delamination is determined based on $P_{max}C_0$, where $P_{max}$ is the critical load for delamination onset, as listed in Table 4.4, and $C_0$ the initial compliance of the corresponding beam specimen.

Table 5.1 Mechanical properties of the Beam test specimens

| | $E_{11}$ (GPa) | $E_{22} = E_{33}$ (GPa) | $G_{12} = G_{13}$ (GPa) | $\nu_{23}$ | $\nu_{12} = \nu_{13}$ |
|---|---|---|---|---|---|
| Glass/polyester composite | 28.6 | 6.0 | 6.0 | 0.3 | 0.3 |

Figure 5.2 shows that $G_a$ value increases with the increase of the total delamination crack length, until the length reaches the value of half span length, 25 mm, which is represented by the peak point of the curve. After that, $G_a$ value decreases. A horizontal dash line at 2000 J/m$^2$ is drawn in the figure to indicate the critical energy release rate for delamination ($G_C$), estimated from the experimental study described in Section 4.3. Based on the $G_C$ value, Figure 5.1 suggests that a critical delamination length of 12 mm is required to initiate unstable delamination growth. With the assumption that

$G_C$ for delamination arrest is the same as that for growth, the figure also suggests that the total delamination length is 38 mm, corresponding to point B in Figure 5.2. Eq. (5.8) suggests that for a total crack length of 38 mm, $a_1$ should be 3.9 mm and $a_2$ 34.1 mm. Since $G$ is always above the level of $G_C$ between points A and B, delamination growth in this crack length range should occur in an unstable manner.

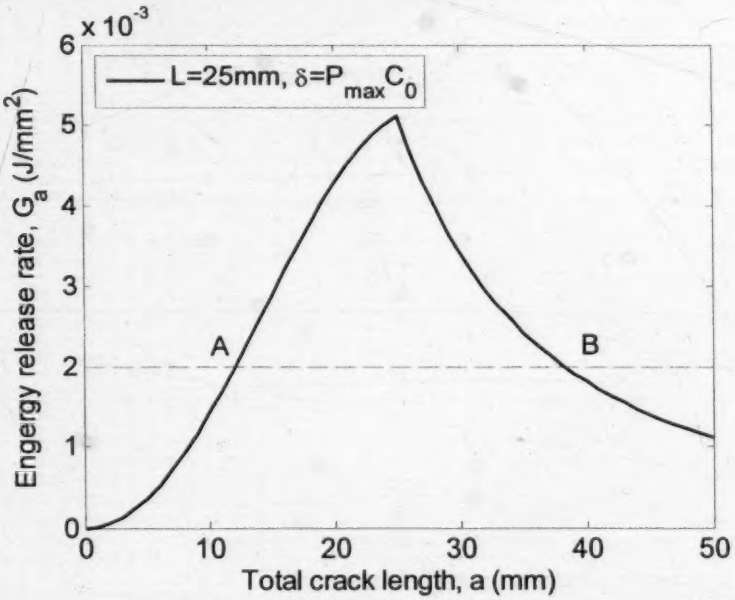


Figure 5.2 Variation of $G$ with delamination length for a beam specimen subject to constant deflection.

Using the above approach, the predicted values for total delamination crack length, $(a_1+a_2)$, are compared with those obtained experimentally, and summarized in Table 5.2 under the column ERR (representing the energy release rate). The table suggests that the predicted values of total delamination crack length are fairly consistent with, but slightly smaller than those measured experimentally, especially for span lengths up to 55 mm. Significant discrepancy was found at the span length of 60 mm. This discrepancy might

have come from the unstable manner of the crack growth, possibly because the analytical $G_a$ value was derived based on the static state.

Table 5.2 Comparison of the results from the Beam test and those predicted using the approaches based on $G$ (ERR) and change of total energy (TE).

| 2$L$ (mm) | Total crack length (mm) | | | $a_2$ (mm) | | | $a_1$ (mm) | | |
|---|---|---|---|---|---|---|---|---|---|
| | Prediction | | Test | Prediction | | Test | Prediction | | Test |
| | ERR | TE | | ERR | TE | | ERR | TE | |
| 30 | 18 | - | 17.3 | 1 | - | 0 | 32 | - | 32.3 |
| 35 | 22.0 | - | 22.6 | 1.4 | - | 0.6 | 38.1 | - | 39.5 |
| 40 | 27.5 | 33 | 30.0 | 2.3 | 3.8 | 1.3 | 45.2 | 49.2 | 48.8 |
| 45 | 32.0 | 41 | 34.0 | 2.9 | 5.1 | 2.2 | 51.6 | 13.4 | 54.3 |
| 50 | 38.0 | 65 | 42.5 | 3.9 | 9.5 | 3.3 | 59.1 | 80.5 | 64.3 |
| 55 | 46.0 | 91 | 51.0 | 5.3 | 13.1 | 3.7 | 68.2 | 105.4 | 74.8 |
| 60 | 54.0 | 122 | 96.0 | 6.7 | 16.7 | 8.6 | 77.3 | 135.3 | 117.4 |

### 5.3.2 Based on the balance of total energy

An alternative approach to predict the delamination length in the Beam test is described as follows. This approach considers the change of total energy of the beam specimen during the delamination development. The principle of energy conservation [51] is

$$\delta W - \delta U_D = \delta U + \delta U_K \tag{5.9}$$

where $W$ represents the input energy, $\delta U_D$ the irreversible energy loss, $\delta U$ the change of the strain energy, and $\delta U_K$ the kinetic energy generated by the unstable delamination growth. It should be noted that $\delta U_K$ will eventually be consumed by damping.

Since the Beam test generated delamination at constant deflection, the input energy, $\delta W$, is zero. By ignoring other types of energy loss, such as friction energy and plastic deformation of the matrix, the sole contribution of $\delta U_D$ is the formation of fracture surfaces, i.e. $\delta U_D = G_C \cdot \delta a$. By definition, $\delta U$ is equal to $(-G \cdot \delta a)$. Therefore, rewriting Eq. (5.9) in an integral form yields

$$\int G_C da - \int G da = -\int dU_K \tag{5.10a}$$

Through integration over the crack growth path, it yields:

$$G_c a - \int_0^a G\, da = -U_K \Big|_0^a \tag{5.10b}$$

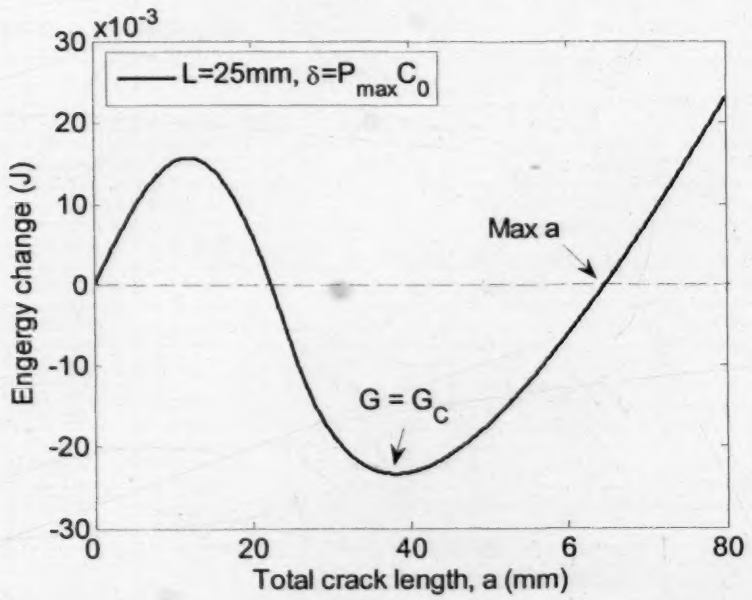


Figure 5.3 Total energy change during the delamination growth when subjected to constant deflection.

Since the kinetic energy during the delamination development must be either positive or zero, value of $[\, G_C a - \int_0^a G\, da \,]$ should be negative or zero. That is, the delamination growth should not result in a positive value of $[\, G_C a - \int_0^a G\, da \,]$.

As an example, value of $[\, G_C a - \int_0^a G\, da \,]$ is plotted in Figure 5.3 as a function of crack length in a beam specimen with a span length of 50 mm, under constant bending deflection of $P_{max} C_0$ (same as that used for Figure 5.2). Figure 5.3 shows that the value of $[\, G_C a - \int_0^a G\, da \,]$ becomes positive when the delamination length reaches 65 mm, which is the maximum length for delamination development. The true delamination length obtained experimentally, however, could be much shorter than that predicted by this approach, because the kinetic energy may not be negligible.

The delamination lengths for all test configurations predicted using this approach are listed in Table 5.2, under column TE (representing total energy). The TE column shows that for span lengths of 40 mm and longer, the predicted crack length values are consistently larger than those measured experimentally. Therefore, the approach of using the change of total energy provides an upper bound for delamination length developed in the Beam test.

It should be noted that for the short span lengths of 30 and 35 mm, a significant portion of the delamination growth was found to occur in a stable manner, producing a non-linear load-displacement curve. Therefore, it is questionable whether this approach can be applied to delamination development in Beam tests using such short span length, as the initial part of the crack growth is expected to occur in a stable manner.

## 5.4 Concluding remarks

Analytical studies were conducted to explore possibilities of predicting delamination development in the Beam test. Since the crack in the Beam test has two fronts, criteria for equal and unequal energy release rates in the two crack growth directions were proposed to determine their relative crack growth rate. Analytical approaches, based on either differential or integral form of the energy release rate, were proposed to estimate the lower and upper bounds of the delamination size. The prediction has shown good agreement with the experimental results, suggesting that the analytical approaches could be used to predict the delamination size developed in the Beam test.

# Chapter 6 Finite Element Simulation of Delamination

## 6.1 Introduction

The FEM techniques for determining the energy release rate such as the CDT, the EDT, the VCCT and the *J*-integral seems to be able to simulate delamination growth by simply comparing the FEM $G$ values to the experimentally determined $G_C$ value. However, there are difficulties for such applications. For example, the CDT and the EDT are inherently impossible to simulate crack growth, because the crack growth path and rate are the prerequisites for applying these techniques. The VCCT and the *J*-integral are hindered by the lack of topological information of the crack profile that is needed to calculate $G$ for the crack growth. As a result, these techniques are only used to predict the onset of crack growth.

A different approach, known as cohesive zone model (CZM), provides an alternative solution to avoid the above difficulties. Use of the CZM to simulate crack growth is depicted in Figure 6.1 in which a cohesive zone is bounded by upper and lower cohesive surfaces. A damage zone is developed in the cohesive layer to simulate crack growth, properties of which degrade with deformation due to the material damage or plastic softening. A stress limit is set for the cohesive zone based on the material strength, which also serves as a criterion for the damage initiation. That is, when the stress limit is reached, the damage starts to develop, and the stress decreases with the increase of the relative displacement ($\delta$) between the two cohesive surfaces. Eventually, the stress is

reduced to zero, leading to the formation of a new crack area. The coupling between stress ($\sigma$) and $\delta$ is governed by the cohesive constitutive law, with the area underneath the $\sigma$–$\delta$ curve representing the critical energy release rate, $G_C$, as also shown in Figure 6.1.

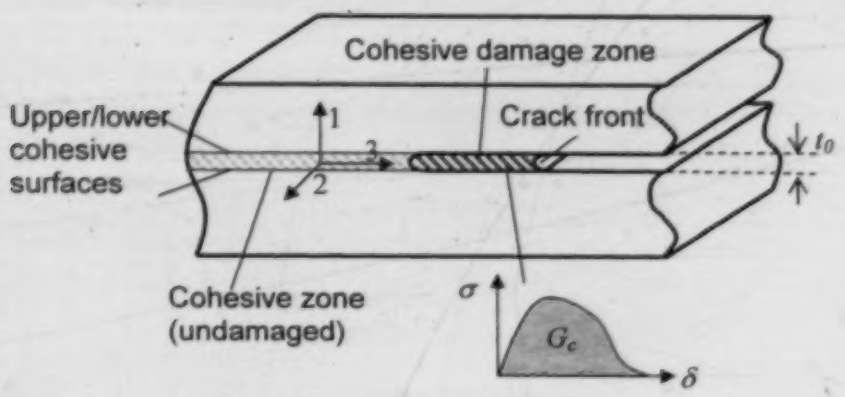


Figure 6.1 Schematic of the cohesive zone model.

In the past, the CZM was implemented in FEM using nonlinear spring [52-56] or interface elements [57-64, 64-77] that have all three key properties mentioned above, namely, damage initiation criterion, constitutive law ($\sigma$–$\delta$ curve), and the material property, $G_C$.

The critical energy release rate $G_C$ is a material constant that should be obtained experimentally, as discussed in Chapter 4.

Most of the constitutive laws in the literature were developed in a phenomenological way, in which the $\sigma$–$\delta$ curve was expressed in several functions, such as an exponential function [77, 78], a trapezoidal function [79], or the most commonly used bi-linear function [60, 64, 73, 80]. To our knowledge, there is no preferred function for the $\sigma$–$\delta$ curve, as these functions show similar results in simulation. This is because

the constitutive laws mainly govern the behavior within the cohesive damage zone that is too small to affect the global response.

The past FEM works using interface elements [59, 60] have shown that the simulation results, especially in terms of load-displacement curve, are not sensitive to the damage onset criteria, which are commonly functions of stress and material strength, except when an excessively "weak" material is used. The use of weak material results in a very large cohesive damage zone, thus significantly reducing the global stiffness of structures. Blackman et al. [60] and Alfano et al. [59] had suggested some methods to optimize the cohesive zone strength in the damage onset criteria for increasing the computational efficiency without losing the accuracy. Nevertheless, all examples studied in Refs. [59, 60] had an initial crack to ensure that the damage onset criterion is satisfied at least in one element in the crack tip region due to the stress concentration incurred by the crack. Thus delamination always starts from the initial crack tip. However for composites without initial defect, where delamination is believed to be initiated from matrix crack [46, 81, 82], the value of material strength and the expression of damage onset criterion could be of great importance to the simulation results. Criteria for the accurate prediction of damage onset in defect-free composites may involve all stress components, such as the criteria by Choi et al. [81] and by Hou et al. [83, 84]. However, these criteria cannot be implemented in any CZMs using interface elements. This is because the interface elements [57-64, 64-77] are formulated based on the displacement jump vector and the corresponding energy-conjugated traction vector. They do not have the in-plane normal stress components. Another approach in the literature using spring

elements [52-56] can only adopt the simple maximum stress criterion, since axial stress is the only stress component that can be considered.

To overcome the above difficulties, a new approach is developed, which uses solid elements and a new material model called "cohesive damage material", to implement the CZM in FEM. Solid elements have all the stress components so that multi-axial-stress-based damage initiation criteria can be used. Meanwhile the cohesive damage material will adopt a damage evolution law based on the concept of the CZM, i.e. using critical energy release rate to control the damage development.

Note that there are many damage material models reported in the literature to simulate delamination. However, none of them considers the critical energy release rate for the damage evolution. For example, refs. [83, 84] used a prescribed function for the damage development; Ref. [81] assumed an immediate drop of material modulus to zero after the damage initiation.

In brief, compared to the interface elements, the new approach to be described in this chapter has the advantage of being able to adopt any damage initiation criterion, while compared to other damage material models, the new approach has a physically meaningful delamination evolution law.

## 6.2 Cohesive damage material

Using the cohesive damage material approach, the cohesive zone is represented by a thin layer of continuum solid elements, of which the properties change due to the damage development. The cohesive zone is inserted between two potentially separable surfaces with local coordinates that have 1-axis perpendicular to the crack surfaces, as shown in Figure 6.1, in order to facilitate determining the fracture mode. For example, when

subjected to mode I loading, the cohesive zone layer is expected to extend in the 1-direction. Thus, by examining deformation of the cohesive zone layer, the fracture mode can be determined. In this chapter, all stresses are expressed according to the local coordinates shown in Figure 6.1.

### 6.2.1 Constitutive relationship

The cohesive damage material adopts the isotropic damage elastic constitutive relationship. Denoting $d$ as the ratio of the damaged (or cracked) surface over total surface area at a local material point, the physical stress could be correlated to a reference stress state $\bar{\sigma}_{ij}$ [85], by

$$\sigma_{ij} = (1-d)\bar{\sigma}_{ij} \quad (i,j = 1, 2, 3) \tag{6.1}$$

with $\bar{\sigma}_{ij}$ being the corresponding stress of the physical strain $\varepsilon_{ij}$ in the undamaged state,

$$\bar{\sigma}_{ij} = E_{ijkl}\varepsilon_{kl} \quad (i,j,k,l = 1, 2, 3) \tag{6.2}$$

where $E_{ijkl}$ is the initial elastic stiffness. Substituting Eq. (6.2) to (6.1) gives the constitutive equation for the isotropic damage linear elasticity:

$$\sigma_{ij} = (1-d)E_{ijkl}\varepsilon_{kl} \quad (i,j,k,l = 1, 2, 3) \tag{6.3}$$

The range of $d$ is from 0 to 1. When the damage is fully developed, i.e. $d$=1, based on Eq. (6.3) the material cannot withstand any types of load, thereby possibly leading to the interference between the upper and lower cohesive surfaces. To avoid the interference, stiffness degradation in the out-of-plane direction (1-direction in Figure 6.1) is prohibited when the compressive strain occurs in that direction.

### 6.2.2 Damage initiation criterion

Previous experimental studies on fiber composites [46, 81, 82] have shown that specimens without a starting defect are expected to initiate delamination from matrix cracking in the resin-rich region between two adjacent layers. For this cohesive damage material model, the damage initiation criterion is expressed in two functions, depending on the hydrostatic stress component ($\sigma_{ii}$) being positive or negative:

$$e = \begin{cases} (\sigma_{ii}/T)^2 + (\sigma_{12}^2 + \sigma_{13}^2)/S^2 & (\text{for } \sigma_{ii} > 0) \\ [\sigma_{12}^2 + \sigma_{13}^2 - (\alpha\sigma_{ii})^2]/S^2 & (\text{for } \sigma_{ii} \le 0) \end{cases} \tag{6.4}$$

where $\sigma_{12}$ and $\sigma_{13}$ are shear stresses, $\alpha$ a non-dimensional parameter that is used to quantify the effect of the compressive hydrostatic stress on the suppression of the matrix cracking, $T$ the transverse tensile strength and $S$ the shear strength of the cohesive zone. The only adjustable parameter $\alpha$ is determined using the critical load for damage initiation, of which the details will be discussed later. The value of $e$ determines whether the critical condition for damage initiation is reached. That is, the damage is initiated when $e$ is equal to or larger than 1.

The use of the expression of Eq. (6.4) for the damage initiation criterion reflects the common phenomenon that the hydrostatic compression may slow down or suppress the damage initiation [86]. Note that when subjected to pure tensile or shear stresses, the above criterion is identical to the maximum tensile or shear stress criterion, respectively. Section 6.4 will present an example with the damage development in a stress state that is a combination of normal and shear stresses, to evaluate the validity of the criterion for the damage initiation.

### 6.2.3 Damage evolution law

*$G_C$ in mixed mode fracture*

The total critical energy release rate $G_C$ in mixed mode fracture is assumed to be a function of $G_{IC}$ and $G_{IIC}$. Several approaches have been suggested to determine $G_C$ for the mixed mode of fracture, such as power-law, exponential, or linear/bilinear functions, as summarized by Reeder [32]. In this cohesive damage material model, the simple B-K criterion [33], proposed by Benzeggagh and Kenane, is used. It assumes $G_C$ as

$$G_C = G_{IC} + (G_{IIC} - G_{IC})\beta^{\eta} \tag{6.5}$$

where $\eta$ is a semi-empirical parameter and $\beta$ the mode-mixing ratio that is defined as the ratio of $G_{shear}$ to $G_C$. Note that $G_{shear}$ gives no distinction between the sliding mode (mode II) and the tearing mode (mode III) of fracture, following the suggestion by Camanho et al. [63]. The total energy release rate due to mode II and mode III of fracture is simply regarded as $G_{shear}$.

*Mixed mode ratio*

In principle, the $\beta$ value in Eq. (6.5) should be determined after the damage has been fully developed. On the other hand, the FEM simulation based on the cohesive damage material model needs a $\beta$ value to determine $G_C$ (see Eq. (6.5)) once the material starts to degrade. To overcome this dilemma, a temporary $\beta$ value is assigned based on present state of the energies absorbed by the deformations of shear and opening modes, $U_{Shear}$ and $U_I$, respectively. Thereby,

$$\beta^{temp} = U_{shear}/(U_{shear} + U_I) \tag{6.6}$$

where $U_{shear}$ and $U_I$ are defined as,

$$\begin{cases} U_{shear} = 2t_0 \int \sigma_{12} d\varepsilon_{12} + 2t_0 \int \sigma_{13} d\varepsilon_{13} \\ U_I = t_0 \int \langle \sigma_{11} \rangle d\varepsilon_{11} \end{cases} \tag{6.7}$$

where $t_0$ is the thickness of the cohesive zone (see Figure 6.1) and $\langle * \rangle$ denotes that the term equals zero if "*" is negative, otherwise equals "*". The $\beta$ value will be recalculated at each time increment according to the updated $U_{shear}$ and $U_I$ values. Eventually, $\beta$ is fixed when the material is completely damaged, and by that time all stress components are zero.

*Development of damage parameters*

Eq. (6.3) shows that the damage factor $d$ is the only parameter that governs the degradation of the material stiffness. The evolution of $d$ can be defined by any non-decreasing function, valued from 0 to 1, of any state variables such as stresses, strains and strain energy. In the cohesive damage material, the evolution of $d$ is given below as a function of $U_{shear}$ and $U_I$ (see Eq. (6.7)),

$$d = \frac{d^E G_C}{d^E (G_C - U_0) + U_0} \tag{6.8}$$

where $d^E$ is

$$d^E = \max \begin{pmatrix} 1 - \sqrt{1 - (U_{shear} + U_I - U_0)/(G_C - U_0)} \\ \text{historically high } d^E \end{pmatrix} \tag{6.9}$$

$U_0$ in Eqs. (6.8-6.9) equals to the summation $U_{shear}$ and $U_I$ when damage initiation criteria are satisfied at the first time, i.e.

$$U_0 = (U_{Shear} + U_I)|_{e=1} \tag{6.10}$$

It is easy to find that $d^E$ increases monotonically with the increase of $(U_{Shear} + U_I)$ in Eq. (6.9). In the case of unloading, i.e. with the decrease of $(U_{Shear} + U_I)$, $d^E$ will remain its historically high value. The physical significance of $d^E$ will be discussed in the following. Note that the damage parameter $d$ fully governs the degradation of the stiffness in the cohesive damage material. The other parameter $d^E$ is merely for the convenience of modeling the swelling and frictional force effect which will be discussed in Section 6.2.5.

### 6.2.4 Stress-strain response in pure mode fracture

The cohesive damage material model defined in Section 6.2.1~3 is implemented in the finite element code ABAQUS/Explicit through its user subroutine VUMAT. The stress-strain response of this material model under pure mode I loading is obtained by applying tensile deformation to a single element with the cohesive damage material properties, as described in Figure 6.2.

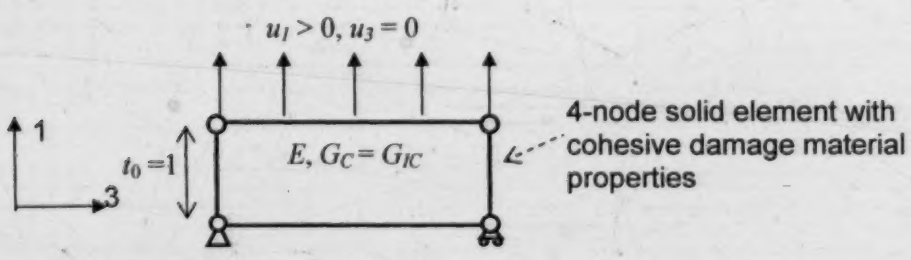


Figure 6.2 Finite element model for determining load-displacement response in opening mode fracture.

The stress-strain response obtained from the single element test is a bilinear curve, as illustrated in Figure 6.3(a). The horizontal axis of the figures in Figure 6.3 can also

represent the opening distance $u_1$ which equals the product of $\varepsilon_{11}$ and thickness $t_0$ (=1 in this single element test), thus the area in the figure represents energy per unit area.

In Figure 6.3(a), point A refers to the moment when the damage initiation criterion is met. Therefore, the area OAD equals $U_0$. Beyond point A the stress reduces linearly with the opening distance ($\varepsilon_{11}t_0$). Let point B represent the current state, the total energy input per unit cohesive zone area at B is the area of the quadrangle OABE, which can be divided into triangle OAB and OBE, representing the unrecoverable energy loss due to material damage and the recoverable elastic strain energy, respectively. If the opening load keeps increasing from current state, point B, the stress will go down following the line segment BC until unrecoverable energy loss equals $G_C$ that is the area of triangle OAC. After that all the stress components will be zero. On the other hand, if unloading is applied at point B, the stress will go back to zero linearly following the dashed line with a slope of $(1-d)E$.

Figure 6.3(b) plots the evolution of the damage parameters $d$ and $d^E$. Both start to increase from 0 (point A'), following two different paths, to 1 (point C') for the complete damage development. If unloading is applied during the damage development, for example, at the displacement corresponding point B, $d$ and $d^E$ defined by Eqs. (6.8-6.9) will maintain their historically high value with the decrease of displacement, as shown by the black dashed line in Figure 6.3(b). This is to reflect the fact that damage in the material is irreversible.

It is noticed that in Figure 6.3(b), the parameter $d^E$ is proportional to the opening displacement measured from point A', $\delta_I$, and its value is equal to the ratio of area OAB to OAC in Figure 6.3(a). We have shown that area OAB is the unrecoverable energy loss

in the cohesive damage material and area OAC equals the maximum energy that could be dissipated in the process of damage, i.e. $G_C$. Therefore, $d^E$ could be interpreted as the ratio of current energy loss to $G_C$. This interpretation is similar to the physical meaning of $d$, that is, the ratio of stiffness loss to the initial stiffness, as defined by Eq. (6.3).

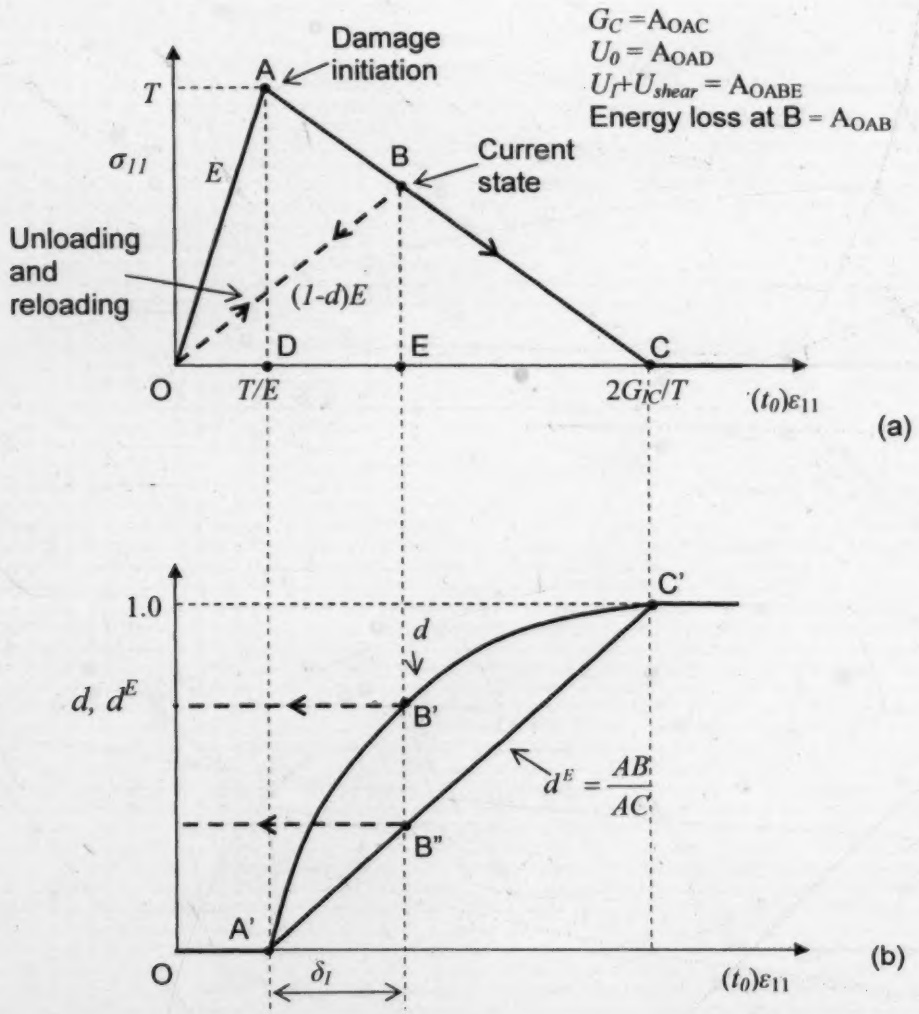


Figure 6.3 The developments of stress and damage parameters with strain.

By applying sliding motion on the single element, as depicted in Figure 6.2, stress-strain curve similar to Figure 6.3(a) can be obtained, with $d^E$ proportional to the sliding distance $\delta_{slide}$ measured from the damage initiation point and having similar meaning as the ratio of current energy loss to the critical energy release rate. However, when a mixed mode loading is applied, the load-displacement curves for the normal and shear stresses are not necessarily bilinear and $d^E$ does not hold the above physical meaning, because $G_C$ keeps changing with damage development due to the variation of $\beta$ value.

It should be noted that changing the expression of $d$ (Eq. (6.8)) could yield different shapes of stress-strain curves. The requirement on the expression of $d$ is that it has to be equal to 0 before the damage initiation criterion is fulfilled, and 1 when the total energy consumed by the material equals $G_C$. It should also increase monotonically and continuously in between. However, when the definition of $d$ changes from Eq. 6.8, $d^E$ may not represent the fraction of the energy release rate unless its definition in Eq. (6.9) is also changed.

### 6.2.5 Special issues related to mode II fracture

*Swelling*

Swelling refers to the inflation of the material in the direction normal to the crack surface, which is accompanied with the mode II facture. This phenomenon, as illustrated in Figure 6.4, is because of the mismatch of surface topography when sliding motion occurs. The coarse fracture surfaces might be formed by matrix hackles (see Figure 4.1), broken bridging fibers (Figure 4.10) and stitching threads (Figure 4.16). The swelling could incur

additional stress in the direction normal to the surface if the vertical motion is restricted, such as in the crack tip region caused by the adjacent non-cracked part. This effect on the stress may not exist in mode I fracture, because fracture occurs by moving the surface away from each other thus avoiding the interference.

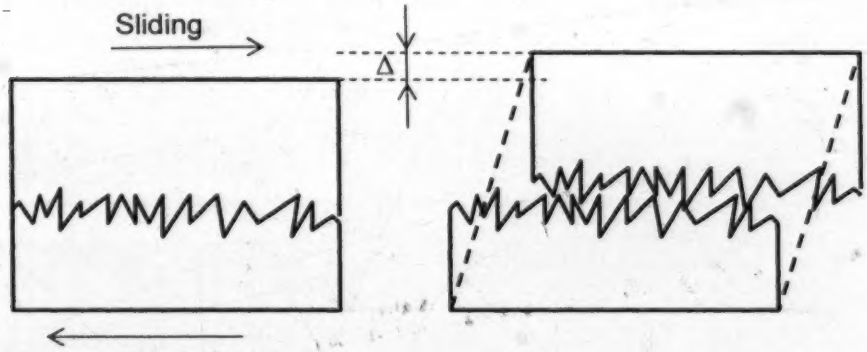


Figure 6.4. Swelling due to mode II fracture and coarse fracture surface.

Swelling is implemented in the cohesive damage material model by adding a mechanism as described in Figure 6.5 on top of the isotropic damage elastic material model (defined in Section 6.2.1). The mechanism for swelling contains a vertical spring that has one end fixed on the top surface and the other end rested on a slope. The four circles represent the nodes of an element for the cohesive layer. It is assumed that the spring is in an un-stretched state before the damage initiation. With shear motion, the spring starts to slide on the slope once damage process begins, thereby being compressed and generating compressive stress to account for the effect of mismatch of the surface topography.

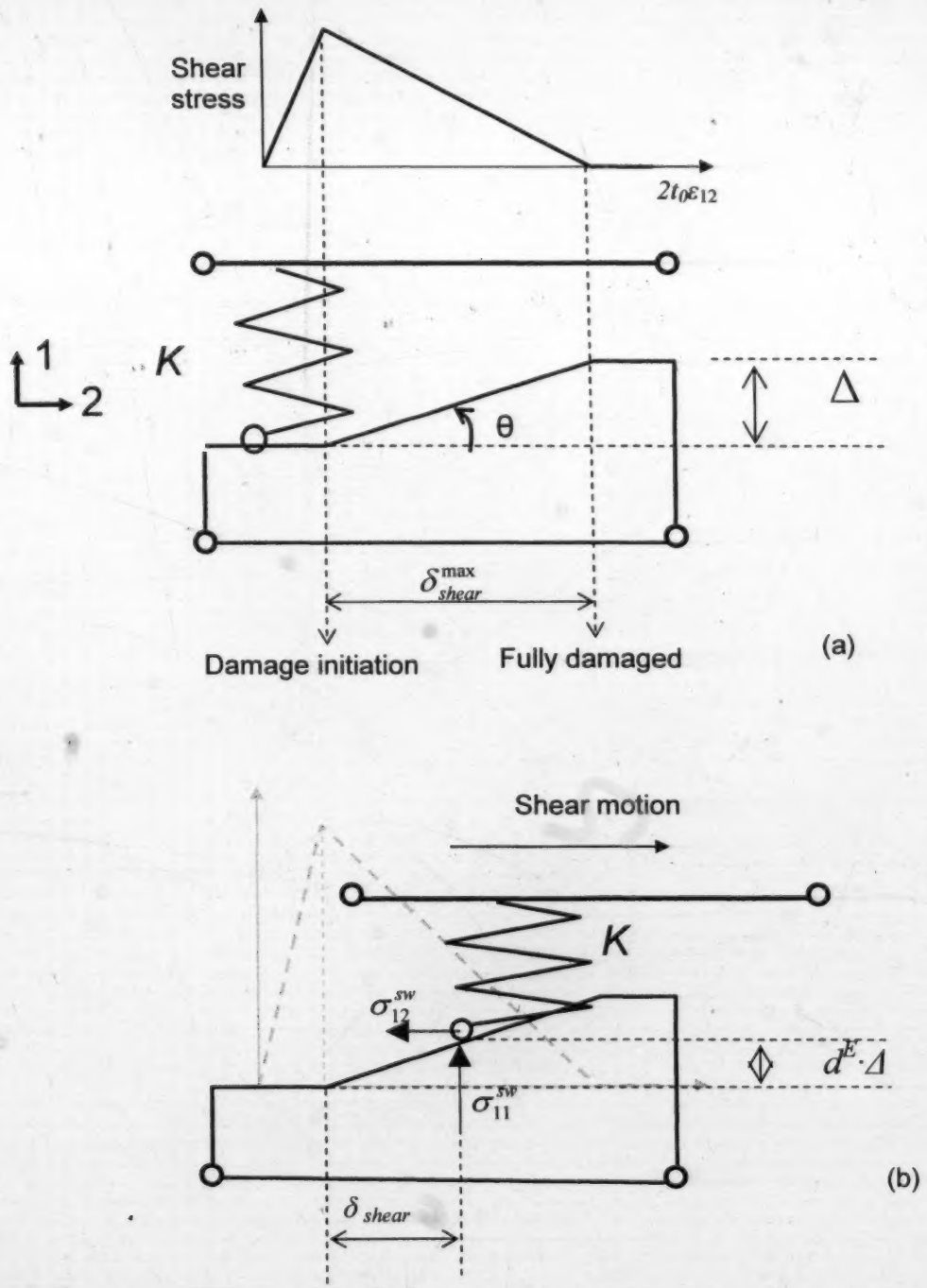


Figure 6.5 Modeling the swelling in the cohesive damage material model: (a) undeformed state and (b) with shear deformation.

The height of the slope $\Delta$ is the maximum value of the expansion when damage is fully developed without any deformation constraints in the 1-direction. The length of the slope is the sliding distance, $\delta_{shear}^{\max}$, measured from the damage initiation to the fully developed damage, as shown in Figure 6.5(a). Figure 6.5(b) suggests that the position of lower end of the spring is proportional to $\delta_{shear}$. Recall that in Section 6.2.4, we have shown the $d^E$ is linearly proportional to $\delta_{shear}$ and valued from 0 to 1. Therefore, the stress due to the spring in the direction normal to the fracture surface can be expressed as

$$\sigma_{11}^{sw} = -(K / t_0) \cdot \left\langle d^E \Delta - < \varepsilon_{11} > t_0 \right\rangle \tag{6.11}$$

where $d^E \Delta$ and $< \varepsilon_{11} > t_0$ are the relative positions of the lower and upper ends of the spring respectively, and $K$ is the spring stiffness constant. The associated shear stress is

$$\sigma_{12}^{sw} = D \cdot (\Delta / \delta_{shear}^{\max}) \cdot \sigma_{11}^{sw} \tag{6.12}$$

where $D$ is a parameter indicating whether the damage is developing at present, which is equal 1 if $\dot{d}^E > 0$, otherwise 0.

*Friction*

Friction between the cracked surfaces is modeled by introducing another term to the total shear stress in the direction opposite to the strain increment after damage takes place. The friction is assumed to be proportional to $\sigma_{11}^{total}$, $d^E$ and the frictional coefficient $\mu_f$. Thus,

$$\sigma_{12}^{f} = \mu_f \cdot \sigma_{11}^{total} \cdot |d\varepsilon_{12}| / d\varepsilon_{12} \tag{6.13}$$

where $\sigma_{11}^{total}$ is the normal stress in the 1-dirction, which is the summation of $\sigma_{11}$ (Eq. (6.3)) due to physical strain and $\sigma_{11}^{sw}$ due to the swelling,

$$\sigma_{11}^{total} = \sigma_{11} + \sigma_{11}^{sw} \tag{6.14}$$

As a result, the total shear stress is comprised of $\sigma_{12}$ (Eq. (6.3)), $\sigma_{12}^{sw}$ (Eq. (6.12)) and $\sigma_{12}^{f}$ (Eq. (6.13)),

$$\sigma_{12}^{total} = \sigma_{12} + \sigma_{12}^{sw} + \sigma_{12}^{f} \tag{6.15}$$

*Stress-strain curves for mode II fracture loading with swelling and friction*

Stress-strain response with consideration of swelling and friction is obtained by applying horizontal displacement $u_2$ on the top surface of an element with unit thickness, as depicted in Figure 6.6. The loading history is also given in Figure 6.6, which suggests that this element is undergoing loading, unloading and reloading, with the damage initiated at point A, and completed at point D.

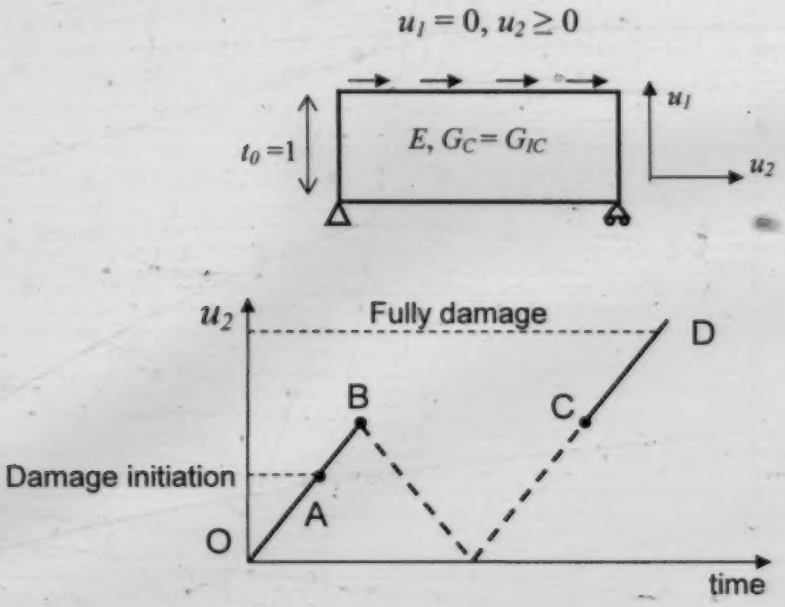


Figure 6.6 Single element for obtaining stress-strain curve and the loading history.

The responses of shear and normal stresses with shear strain for the element depicted in Figure 6.6 are presented in Figures 6.7(a) and 6.7(b), respectively. In both figures the black solid lines are corresponding to loading history A-B and C-D; the

dashed lines are corresponding to the unloading-reloading part B-C; and the gray lines are used as reference corresponding to the stresses without any swelling or fictional force effects.

From point O to point A, the material is in an undamaged state and the stress-strain curves for this part are indistinguishable whether with or without swelling and friction, i.e. $\sigma_{12}^{total}$ increasing linearly and $\sigma_{11}^{total}$ being zero.

From A to B the stress-strain responses start to deviate from the gray lines. The shear stress, in Figure 6.7 (a), is higher by the amount of $(\sigma_{12}^{sw} + \sigma_{12}^{f})$ during loading than that represented by the gray line. The compressive normal stress, plotted in Figure 6.7(b), is generated due to the effect of swelling (see Eq. (6.11)), even though the overall normal strain remains zero.

When applying unloading and reloading (between B and C in Figure 6.6), the normal stress $\sigma_{11}^{total}$ maintains the same value and the shear stress exhibits a hysteresis loop, of which the magnitude of change is $2\sigma_{12}^{f}$ since frictional force changes its direction when shear strain increment changes from positive to negative due to the unloading. Note that $\sigma_{12}^{sw}$ is not involved at this stage because $D$ in Eq. (6.12) is 0 from B to C as damage is not developing.

When reloading is applied and $u_2$ comes back to the same level as point B, the stress-strain will go back to its original path (solid black lines). When the material is completely damaged, $\sigma_{12}^{sw}$ will disappear but $\sigma_{11}^{sw}$ and $\sigma_{12}^{f}$ remain, according to Eqs. (6.11-6.13).

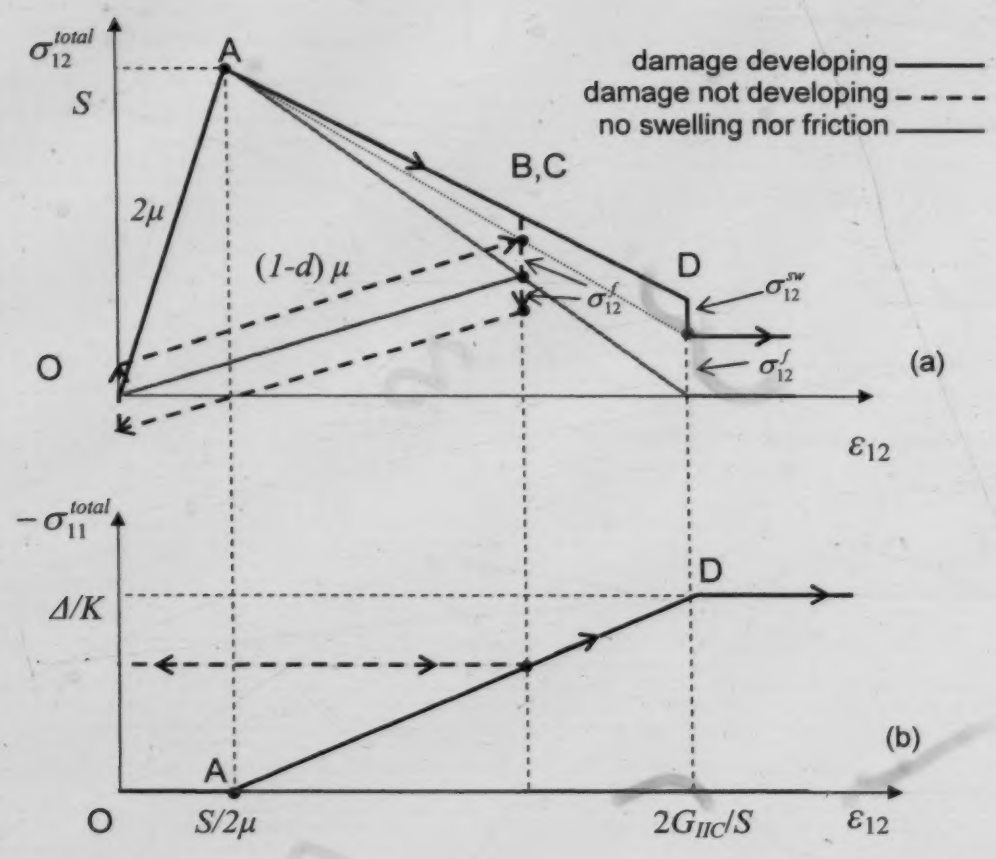


Figure 6.7 The development of stresses under pure mode II loading with swelling effect and friction.

## 6.3 Application to pre-cracked composites

The DCB, ENF, ELS and MMB tests were chosen to verify the validity of the new approach using cohesive damage material model for the simulation of delamination. These four tests cover the scenarios of pure mode I crack growth (DCB), pure mode II crack growth (ENF and ELS), mixed mode I and mode II crack growth (MMB). Configurations of these tests are shown in Figure 1.2. The dimensions of the specimen and test setup for each test were chosen elaborately so that stable crack growth (DCB),

unstable crack growth (ENF and MMB) and an ambiguous state between stable and unstable crack growth (ELS) are all included in these cases studies.

### 6.3.1 FEM models

FEM models for the DCB, ENF, ELS and MMB tests contain three parts: an upper beam, a lower beam and a layer of cohesive zone in between. The upper and lower beams were modeled based on transverse isotropic elasticity, as the specimen contains only 0-degree fiber. Material constants used for the upper and lower beams are listed in Table 6.2. The layer of cohesive zone has a small thickness of 0.02 mm to minimize its role on the global stiffness and to be consistent with physical dimension of the resin rich region. Material constants for the cohesive damage material model are listed in Table 6.3.

Mesh pattern of the FEM models, as shown in Figure 6.8, consists of 4-node, plane-strain continuum elements (CPE4R) for each of the upper and lower beams. To mimic the experimental condition, loading was applied by specifying a reasonably constant displacement rate that is computationally efficient without introducing significantly dynamic effect, such as that by the inertial force.

Table 6.1 Geometrical parameters of the DCB, ENF and ELS tests.

| | $L$ (mm) | $a_0$ (mm) | $h$ (mm) | $\dot{w}$ (mm/sec) | $c$ (mm) |
|---|---|---|---|---|---|
| DCB | - | 50 | 1.5 | 0.8 | - |
| ENF | 50 | 30 | 1.5 | 0.5 | - |
| ELS | 100 | 50 | 1.5 | 2.0 | - |
| MMB | 50 | 25 | 1.5 | 2.0 | 40 |

Table 6.2 Material properties for unidirectional fiber composites used in the study.

| | $E_{11}$ (GPa) | $E_{22}=E_{33}$ (GPa) | $G_{12}=G_{13}$ (GPa) | $\nu_{23}$ | $\nu_{12}=\nu_{13}$ | Material damping (kg/sec) |
|---|---|---|---|---|---|---|
| DCB, ENF, ELS and MMB | 150 | 11.0 | 6.0 | 0.3 | 0.3 | 100* |
| Beam test | 34.3 | 6.0 | 6.0 | 0.3 | 0.3 | 100 |

* Material damping is not used in the DCB model

Table 6.3 Properties for cohesive damage materials and parameters for the cohesive damage material model.

| | Parameters in Eq. (6.2) | | Parameters in Eq. (6.5) | | | Parameters in Eq. (6.4) | | |
|---|---|---|---|---|---|---|---|---|
| | $E$ (GPa) | $\nu$ | $G_{IC}$ (J/m$^2$) | $G_{IIC}$ (J/m$^2$) | $\eta$ | $T$ (MPa) | $S$ (MPa) | $\alpha$ |
| DCB, ENF ELS, MMB | 11.0 | 0 | 300 | 300 | 2.0 | 20.0 | 20.0 | 0 |
| Beam Test | 6.0 | 0 | 500 | 2500 | 2.0 | 47 | 40 | 0.3 |

The element length in the cohesive zone was chosen to be 0.05 mm. According to Turon et al. [76], element length in the cohesive zone layer should be small enough to capture the continuum stress field in the cohesive damage zone. Among many theories that have been used to estimate the cohesive zone length ($l_{cz}$), the most conservative estimate for mode I test is [76]:

$$l_{cz} = 0.21\frac{EG_C}{(T)^2} \tag{6.16}$$

Using the constants in Table 6.3, the above expression yields $l_{cz}$ of 0.77 mm which is more than 15 times of the element size selected for the cohesive layer (0.05 mm). Therefore, the mesh size used for the cohesive zone is deemed sufficiently small to

provide good resolution for the stress distribution. Note that the same element size was used for simulation of all four tests.

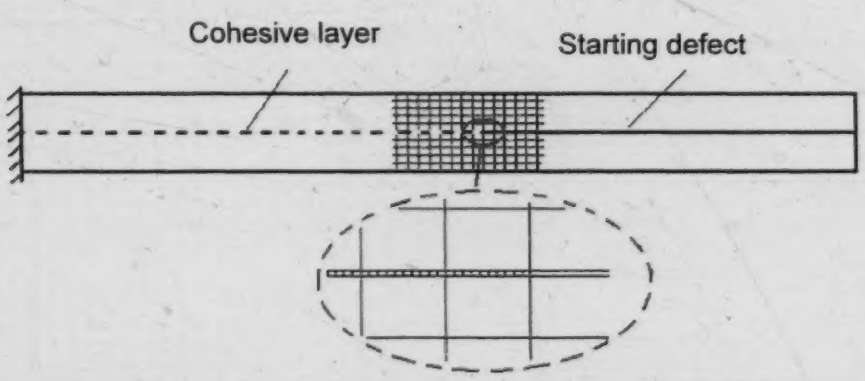


Figure 6.8 The mesh pattern for the DCB, ENF, ELS and MMB tests.

### 6.3.2 The DCB test

Analytical solution for the compliance ($C^{DCB}$) and energy release rate for the delamination growth ($G^{DCB}$) of the DCB specimen, based on beam theory and linear elastic fracture mechanics, are:

$$C^{DCB} = \frac{4a^3}{E_{11}h^3} \tag{6.17}$$

$$G^{DCB} = \frac{12P^2a^2}{E_{11}h^3} \tag{6.18}$$

where $E_{11}$ is the longitudinal Young's modulus, $a$ crack length, $h$ half specimen thickness, and $P$ the reaction force of nodes where the displacement was applied.

The load-displacement curve generated by the FEM model is compared with the analytical solution in Figure 6.9, which includes an initial linear loading section to

represent the response before the delamination propagation commences. The nonlinear descent section that follows the onset of delamination growth was determined based on Eqs. (6.17) and (6.18) by eliminating $a$ and assuming the value of $G^{DCB}$ to be $G_C$ of which the value is given in Table 6.3. The two curves in Figure 6.9 show good agreement, with discrepancy exists only before the delamination growth occurs. Such discrepancy is mainly caused by the underestimate of the compliance of the DCB specimen by the classical beam theory [11], not by the FEM model.

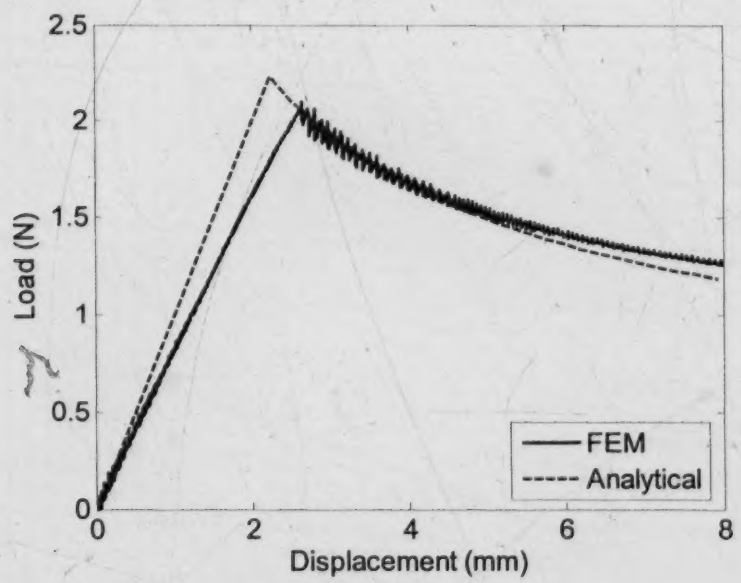


Figure 6.9 Load-displacement curves for the DCB test.

### 6.3.3 The ENF test

The analytical expressions of the ENF test for $C$ and $G$, based on the beam theory, are given by Eqs. (2.33-2.34). Different from the DCB test, the ENF test with setup parameters given in Table 6.1 is expected to generate unstable crack growth. The

unstable crack growth causes specimen vibration though eventually being damped out. Therefore, its FEM model has a material damping function to dissipate the extra energy. Figure 6.10 shows the load-displacement curves generated by the ENF test. The dashed line represents analytical solution, which shows that when the unstable crack growth occurs, i.e. after the maximum load is passed, a phenomenon of displacement snap-back occurs with decrease of the load. The corresponding FEM solution (solid line with "·"), however, shows a phenomenon of "snap-through" of the load decrease from the maximum point, without any decrease of the displacement. Apart from such difference, the FEM prediction shows excellent agreement with the analytical prediction.

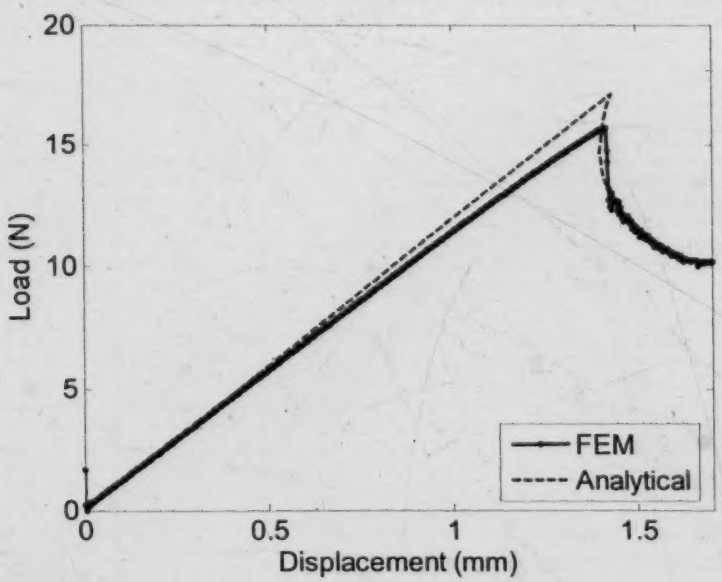


Figure 6.10 The load-displacement curves of the ENF test.

### 6.3.4 The ELS test

The analytical expressions for compliance and energy release rate are given by Eqs. (2.35-2.36). Similar to the ENF test, the analytical expressions generate a "snap-back" behaviour, as shown by the dashed line in Figure 6.11, indicating that the ELS test configuration may also generate unstable delamination growth. However, the FEM solution from the same test configuration shows a progressive drop of force with the increase of displacement, as shown by the thick solid line in Figure 6.11. The contradictory crack growth behaviour generated analytically is because the crack length used in the equations did not consider the additional crack length due to the presence of a damage zone at the crack tip, which based on the FEM model has a length of 9.5 mm. Such a damage zone length should effectively extend the initial crack length so that the ratio of the effective crack length to $L$ exceeds the minimum value required for the stable crack growth, 0.55 (see Table 4.1).

Figure 6.11 also shows that by doubling and tripling the shear strength used in the FEM model, thus decreasing the cohesive damage zone length to 3.9 and 2.4 mm, respectively, the snap-through behavior occurs, suggesting that the delamination growth becomes unstable. Since the two curves are very close to each other, they are presented as thin lines in Figure 6.11 without any distinction from each other.

The curves from FEM in Figure 6.11 indicate that even by tripling the shear strength of the cohesive damage material model, the maximum load only increases slightly. Therefore, the maximum load is not sensitive to the strength value used. This agrees with the conclusion drawn in Refs. [59, 60] in which the dependency on the strength of the cohesive damage material model was found to diminish when a relatively

large value was used. Its insensitivity to the material strength is probably because the stress at the tip of a starting defect can exceed the material strength at a very small load due to the stress concentration. Therefore, the delamination growth is mainly governed by the critical energy release rate ($G_C$). The results suggest that with an existing crack, the main role of material strength in the CZM is to change the size of the damage zone, which may sometimes affect stability of the delamination growth.

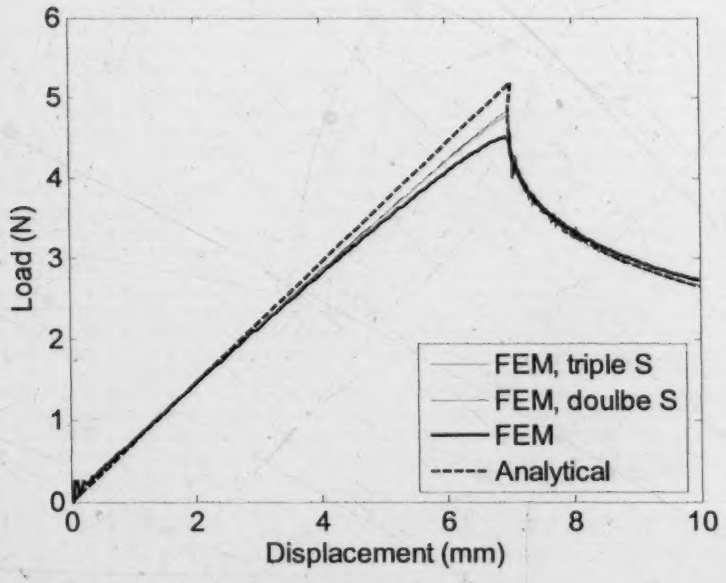


Figure 6.11 The load-displacement curves of the ELS test by the analytical solution and the FEM predictions with varied shear strengths.

### 6.3.5 The MMB test

The MMB test is to measure fracture toughness in mixed mode I and mode II delamination [3]. The load is applied at point A of Figure 1.2(e) at a distance of $c$ from point B that is located at the mid point of the span. The loading on the specimen could be

separated into mode I and mode II, corresponding to DCB- and ENF-type of loading. The analytical solution for the energy release rate in the MMB test is given in terms of $G$ for mode I and mode II fractures,

$$\begin{cases} G_I^{MMB} = 12P_1^2 a^2 / Eh^3 \\ G_{II}^{MMB} = 9P_2^2 a^2 / 16Eh^3 \end{cases} \tag{6.19}$$

where $P_1$ and $P_2$ are the forces for mode I and mode II loading, and can be determined as:

$$\begin{cases} P_1 = P(3c - L)/4L \\ P_2 = P(1 + c_{MMB}/L) \end{cases} \tag{6.20}$$

The compliance for the MMB test is

$$C^{MMB} = \frac{(c_{MMB} + L)[P_1 / C^{DCB} - P_2 / C^{ENF}] - 2c_{MMB} P_1 / C^{DCB}}{LP} \tag{6.21}$$

where $C^{DCB}$ and $C^{ENF}$ are given by Eqs. (6.17) and (2.33), respectively.

The load-displacement curve generated by the FEM model is compared with the analytical solution in Figure 6.12(a). The crack propagation parts of both curves show good agreement. The difference at the linear parts could be attributed to the mode I type of loading on the specimen, which leads to the inaccuracy in the initial slope as discussed in section 6.3.2.

The mixed mode ratio $\beta$ along the crack growth path, for $a_0$ from 25 to 50 mm, is plotted in Figure 6.12(b), compared by the analytical prediction from Eq. (6.19). Despite the discrepancy at the beginning of the crack propagation, the FEM solution matches the analytical one fairly well in the majority of the crack length, showing the accuracy of the cohesive damage material model for the prediction of mode mixing ratio.

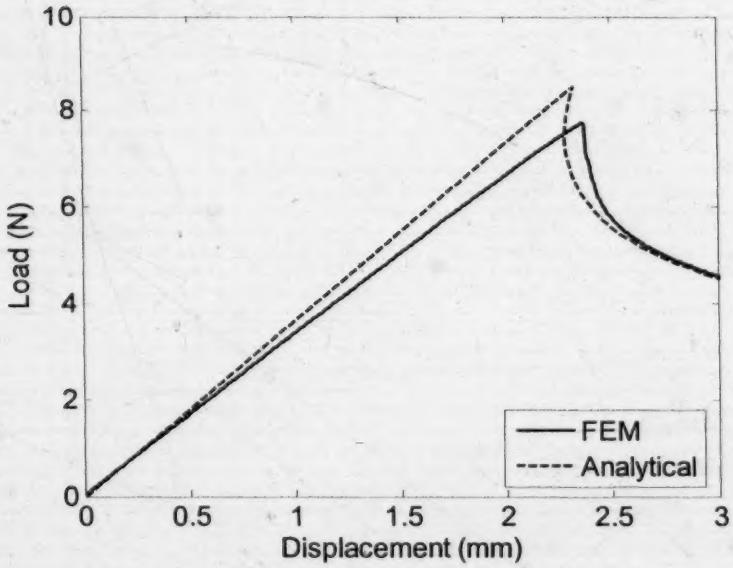


(a)

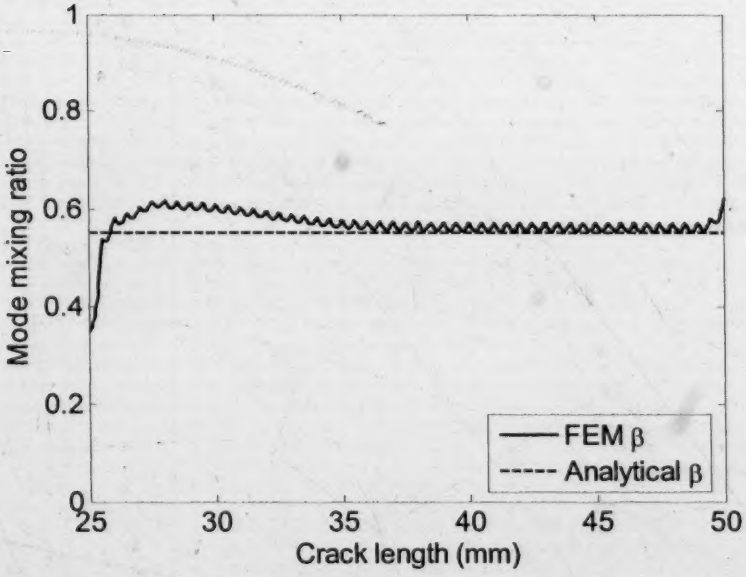


(b)

Figure 6.12 Comparison between the FEM results and the analytical solutions in the MMB test: (a) load-displacement curves; and (b) mode mixing ratio.

## 6.4 Application to the defect-free Beam test

The experimental results from the Beam test were used to further assess the validity of the new cohesive damage material model and the criteria for damage initiation. The main difference between the Beam test and the other delamination tests considered for FEM simulation in Section 6.3 is that the former does not have a starting defect to initiate the delamination.

### 6.4.1 Experimental results from the Beam test

The Beam test results employed in this section were from Ref. [82]. Note that these results are different from those in Chapter 5. All of the Beam test specimens in the previous chapter had the 90-degree layer in the mid-thickness and were loaded using 3-point bending with span lengths as a variable parameter. In Ref. [82] all specimens were loaded with a fixed span length, but with the 90-degree layer placed at a distance of 1/4, 1/2, or 3/4 of the thickness from the bottom surface. The purpose of choosing these Beam test results instead of those described in Section 4.3 is that the latter generated delamination development in the neutral plane of the beam specimen where shear stress is the only stress component, thus could not be used to assess the influence of hydrostatic stress on the delamination development.

The beam specimens are named 1/4-beam, 1/2-beam, and 3/4-beam specimens respectively, according to the position of the position of the 90-degree layer. The experimental phenomena in Ref. [82] were very similar to those described in Section 4.3.2, i.e. unstable delamination initiated from one side of the loading pin at the interface between 0- and 90-degree layers and propagated at the interfaces.

### 6.4.2 FEM simulation of the Beam test

*FEM model*

The simulation was based on a 2D plane-strain model, as shown in Figure 6.13. The model contains three layers, of which the top and bottom layers are orthotropic and elastic with properties corresponding to the 0-degree glass/polyester composite, as given in the lower row of Table 6.2. Properties in the middle layer where delamination occurs are based on the cohesive damage material model, with properties and parameters given in the lower row of Table 6.3. The loading pin had an offset to the right by 0.5 mm, to ensure that crack growth only occurs on one side of the loading pin. A constant loading speed of 10 mm/s was applied until unstable delamination occurred. The specimens were then unloaded at the same speed.

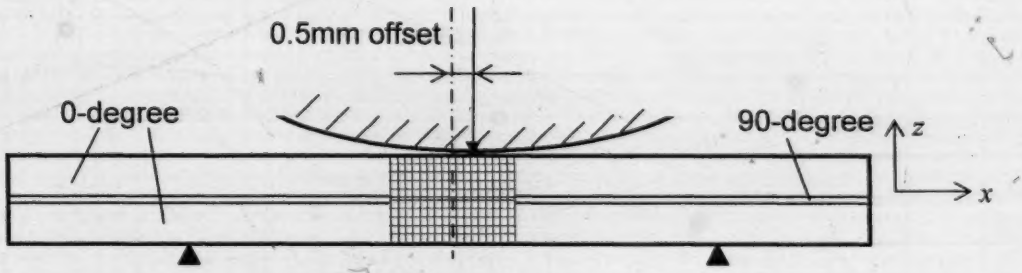


Figure 6.13 The finite element mode of Beam test.

Except Young's modulus $E$ and Poisson's ratio $\nu$ that were based on the previous experimental study [82], values in the lower row of Table 6.3 were chosen in the following way. Tensile strength $T$ was based on the tensile strength of the polyester resin [87], and the shear strength $S$ based on the maximum shear stress of the 1/2-beam test generated at the maximum load because shear stress is the only non-zero stress

component at the mid-thickness and is uniformly distributed between the loading pin and the support. $G_{IIC}$ was set to be equal to 2500 J/m$^2$, according to the value reported before [82], and $G_{IC}$ 500 J/m$^2$ [36]. The parameter $\eta$ was set to be equal to 2, following the suggestion by Benzeggagh and Kenane for brittle fracture [33]. Value of $\alpha$ was chosen to be 0.3 by matching the predicted maximum load for the 3/4-beam test with the experimental results.

*FEM results*

Figure 6.14 compares load-displacement curves for the 1/4-beam, 1/2-beam, and 3/4-beam specimens from the experiments with those from FEM simulations. All curves show that the load increased initially with displacement in a linear style but then dropped quickly to a lower level after a critical loading level was reached. The figures suggest that the FEM simulation generated consistent load-displacement curves with those from the experiments.

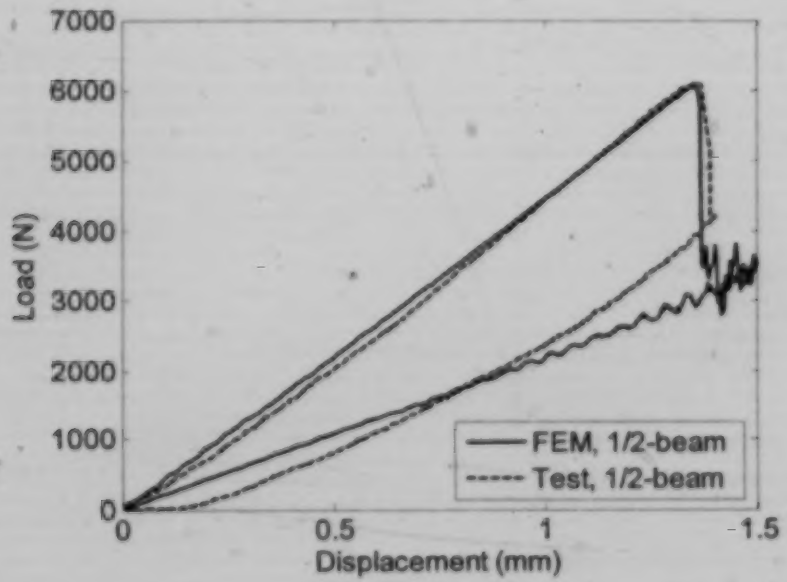


(a)

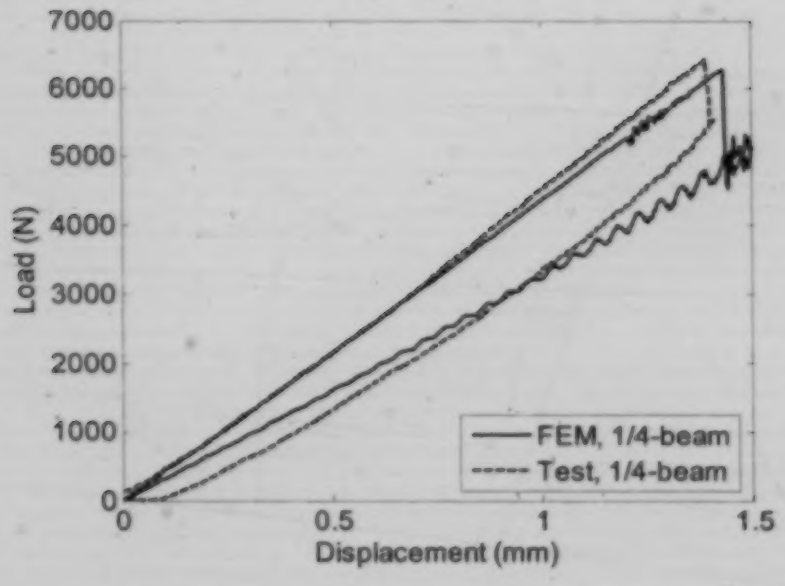


(b)

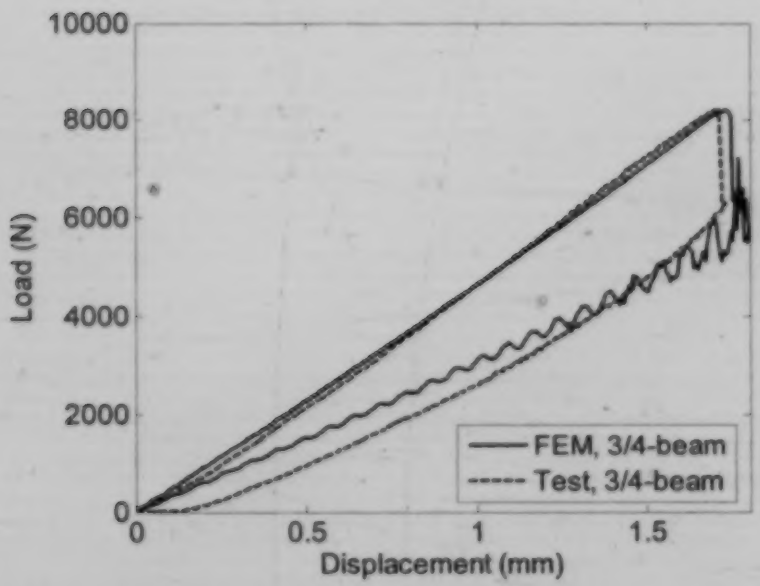


(c)

Figure 6.14 Comparisons of the load-displacement curves from Beam tests for (a) 1/2-beam, (b) 1/4-beam, and (c) 3/4-beam.

Note that the 3/4-beam, Figure 6.14(c), has the maximum load over 30% higher than those for the 1/2-beam or 1/4-beam. Since delamination in the former was initiated

under compressive hydrostatic stress, as mentioned earlier, its maximum load was used to determine $\alpha$ value in Eq. (6.4).

Figure 6.15 compares the locations (pointed by an arrow in the top photographs of all 3 figures) of the delamination initiation in the three types of Beam specimens, with those by the FEM simulation. These comparisons suggest that the delamination was initiated in a location within the range predicted by the FEM models, represented by contour plots of damage factor $d$ below each of the photographs. Note that the brightest region in the contour plots is that with the largest $d$ values. The plot of 1/2-beam, Figure 6.15(a), has almost constant $d$ values between the loading pin and the support. This is because the 90-degree layer lies on the neutral plane where the shear stress distributes uniformly between the loading pin and the support and is the only stress component to initiate the delamination.

It was noticed that the location for delamination initiation, as shown by the photographs in Figure 6.15, has occurred closer to the loading pin and the support for the 1/4-beam and 3/4–beam specimens, respectively, than that in the 1/2–beam specimen. This can be explained by the effect of hydrostatic stress.

For the 1/4-beam specimen, delamination occurred in the region that is subjected to hydrostatic tension. Since the hydrostatic tension encourages damage initiation, delamination is expected to occur close to the loading point where the hydrostatic tension is high.

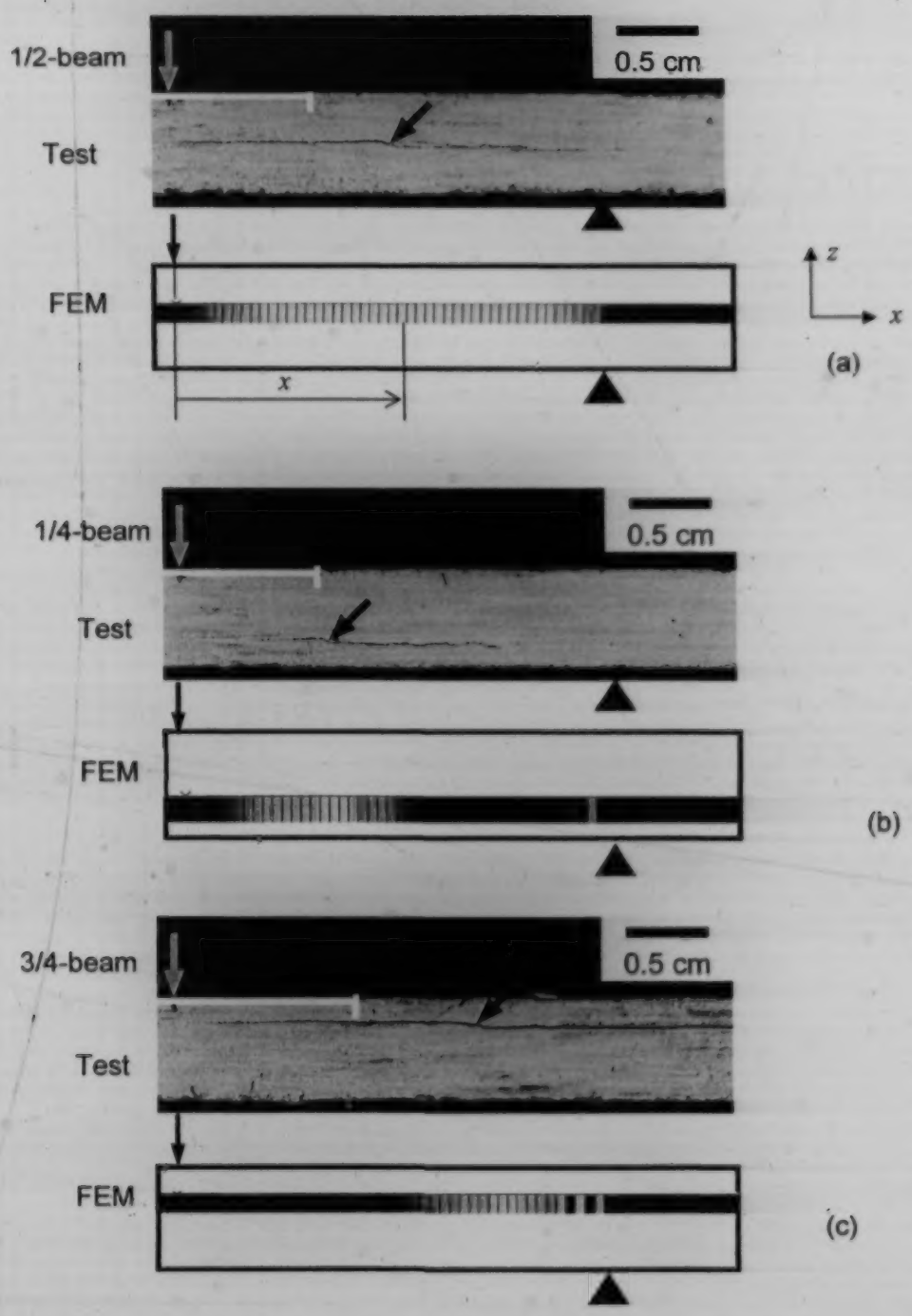


Figure 6.15 Comparisons of the delamination onset locations in the Beam test for (a) 1/2-beam, (b) 1/4-beam, and (c) 3/4-beam.

For 3/4–beam specimens, on the other hand, delamination occurred in the region that is subjected to hydrostatic compression which is known to suppress the damage initiation. Therefore, delamination initiation in the 3/4–beam specimens is expected to occur in a region close to the support where the hydrostatic compression is lowest. Figure 6.15 shows that the FEM models successfully predicted the trend of the locations for the delamination initiation.

Another feature that is significant in the experimental results is the final size of the delamination generated by the Beam tests. The delamination area can be detected by a bright region appearing on the surface of post-tested specimens, as shown by the top photographs in Figures 6.16(a-c), taken from the three types of post-tested specimens. The photographs suggest that size of the delamination is in the order of 1/4–beam < 1/2-beam < 3/4-beam. The trend has been correctly predicted by the FEM models, as shown by the contour plots of $d$ in Figure 6.16 that were taken right after the load drop from the peak load. The pair of white dashed lines in Figure 6.16 indicates where the loading pin (left line) and the support (right line) were.

The main difference in Figure 6.16 between the photographs and the $d$ contour plots is that the delamination area in the post-tested specimens barely went beyond the left dashed line where the loading pin was, while that in the FEM contour plot was slightly over. This was probably because the friction was not considered between fracture surfaces in the FEM simulations, but should have existed in the Beam specimens due to the out-of-plane compression generated by the loading pin. The friction must have prohibited further propagation of the delamination over the line of the loading pin.

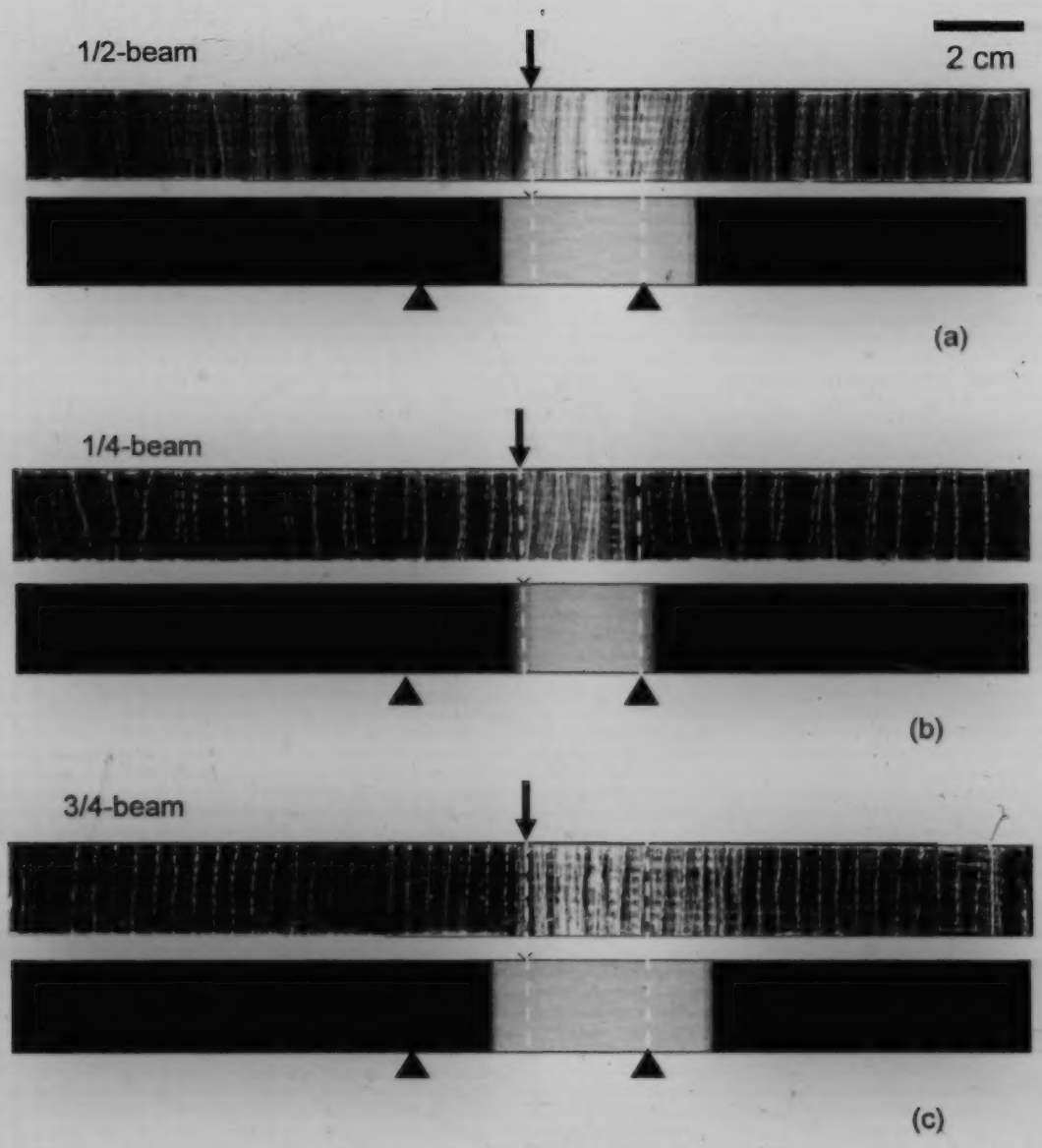


Figure 6.16 Comparisons of the final delamination area generated by the Beam test for (a) 1/2-beam, (b) 1/4-beam, and (c) 3/4-beam.

*Parametric study*

The sensitivity of the simulation results to the longitudinal normal stress $\sigma_{33}$ was examined by changing the term $\sigma_{ii}$ in Eq. (6.4) to $\sigma_{11}$ and setting $\alpha$ value equal to 0, following the criteria proposed by Camanho et al. [63]. Note that the normal stress in the 2-direction is always zero since Poisson's ratio is zero. A study was also carried out using the FEM model, to examine the effect of material tensile and shear strengths on the damage initiation for delamination, by increasing the tensile or shear strength, $T$ or $S$, by 50% but maintaining the same values for the other properties.

Using 1/4-beam as an example, the results from the two parametric studies are presented in Figures 6.17 and 6.18. Figure 6.17(a) shows that without the consideration of $\sigma_{33}$ the critical load for delamination initiation becomes much higher than that determined experimentally. Therefore, $\sigma_{33}$ should have played a significant role on the maximum load allowed before the delamination initiation. The resulted delamination areas are presented in Figure 6.17(b), which also suggests that $\sigma_{33}$ should be considered in the criterion for delamination initiation in order to reduce the delamination area to the size similar to that observed experimentally, Figure 6.17(b). In addition to the above differences, ignoring $\sigma_{33}$ also resulted in the location for delamination initiation at a distance of 19 mm away from the loading pin, which is quite different from the experimental observation of around 8 mm away from the loading pin.

Figure 6.18 summarizes the effect of material tensile ($T$) and shear ($S$) strengths for the cohesive damage material model on the damage development in the Beam specimens. By increasing $T$ or $S$ by 50%, Figure 6.18(a) suggests that a considerable increase of the maximum load is required to initiate the delamination. Figure 6.18(b)

shows that the resulted delamination area also increases, due to the increased amount of energy available for the fracture surface formation.

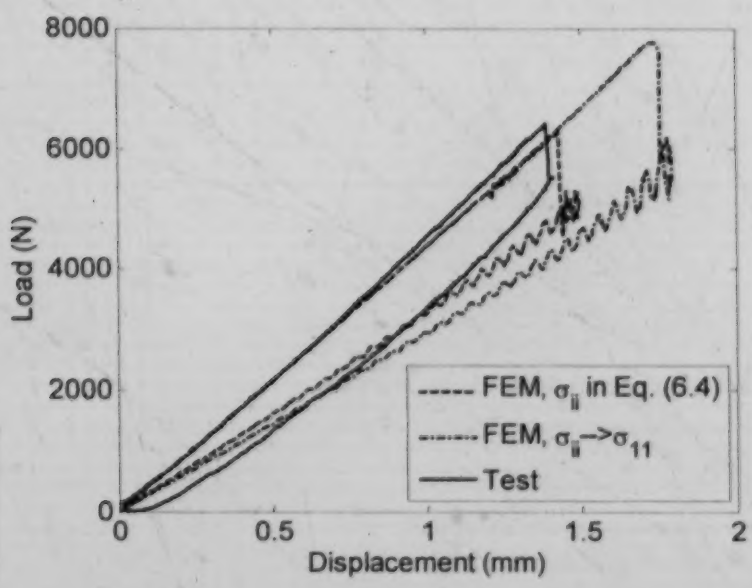


(a)

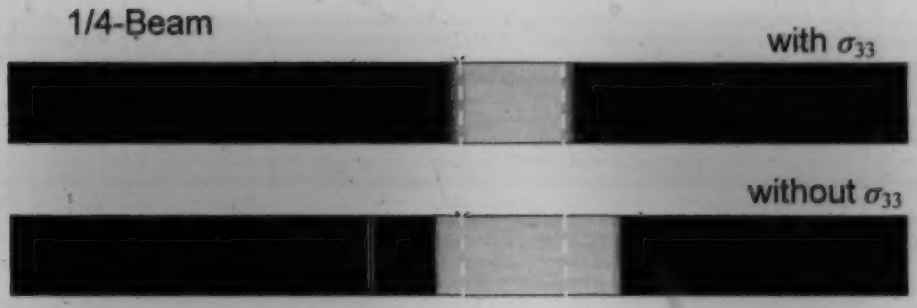


(b)

Figure 6.17 Parametric study of the effect of $\sigma_{33}$ in the 1/4-Beam test: (a) load-displacement curves, and (b) the resulting delamination area with and without the consideration of $\sigma_{33}$.

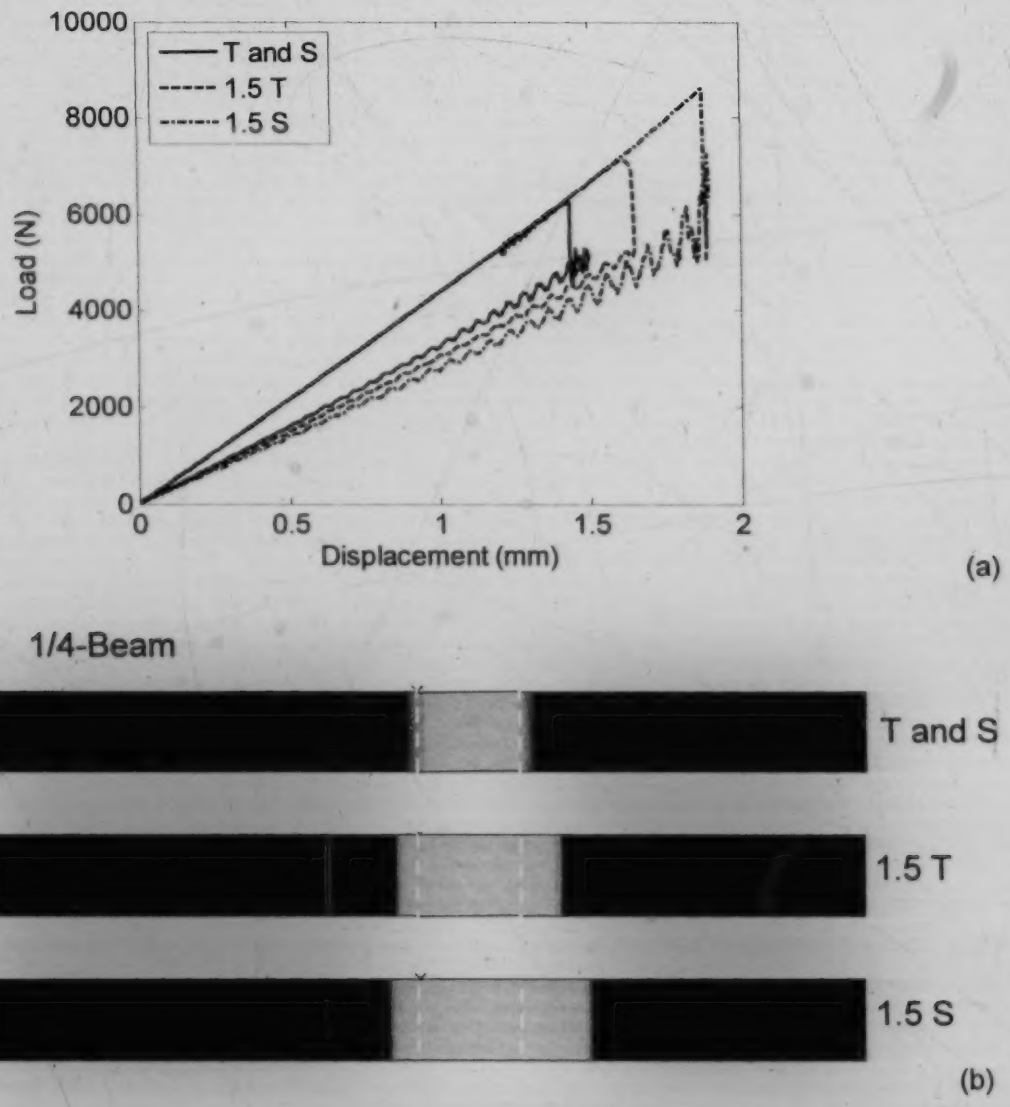


Figure 6.18 Parametric study of the effect of material strength (*T* and *S*) in the 1/4-beam test: (a) load-displacement curves, and (b) the resulting delamination area.

*With swelling and friction*

Swelling and friction are introduced into the simulation of 1/2-beam for mimicking a more realistic situation of the Beam test. Besides the material constants listed in Table 6.2,

three more parameters are needed in this simulation. They are the frictional coefficient that is assumed to be 0.5, $\Delta$ assumed to be 0.2 mm that is less than the average thickness of each fiber layer, and the stiffness $K$ being one-tenth of the stiffness of cohesive zone in undamaged state. These values were chosen intuitively. Therefore, the results are merely to address the influence of the swelling and friction qualitatively during the delamination crack propagation.

In this study two loading cycles were applied to the 1/2-beam. In the 1$^{st}$ cycle, it was loaded upon fracture and unloaded to zero deflection. The load-displacement curve from the FEM model for this cycle is represented by a thick solid line in Figure 6.19. The curve started to drop at about 6000 N which is the same as that shown in experiment (also included in Figure 6.19), suggesting that the swelling effect and friction did not affect the onset of delamination. In addition, the force from the FEM model dropped to 4200 N after the fast delamination growth, which is very close to the experimentally measured value, suggesting that the simulation with the swelling and friction is more realistic than that without these two effects.

In the second loading cycle, the cracked beam was loaded to the same deflection. Even though there was no indication of crack growth, the loading and unloading curves did not follow the same path because of the path-dependency of the friction. It was also found that the unloading part of the curve did not go back to the zero displacement, indicating the existence of the residual deformation. Figure 6.20 is a contour plot of strain in the thickness direction with darker color representing higher strain, after the two loading cycles. It shows the delaminated part between the loading pin and the right

support became thicker than the rest of the specimen, because of the residual strain in the damaged cohesive layer.

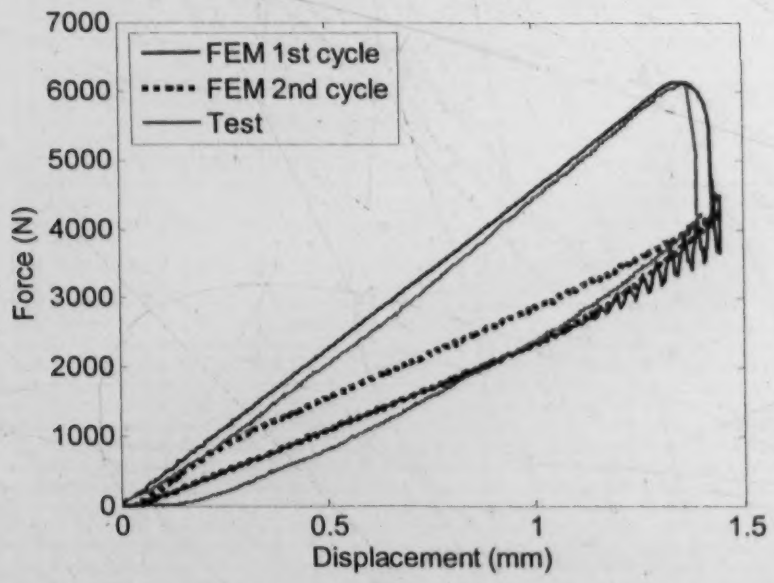


Figure 6.19 Load-displacement curves of the 1/2-beam with the swelling effect and friction.

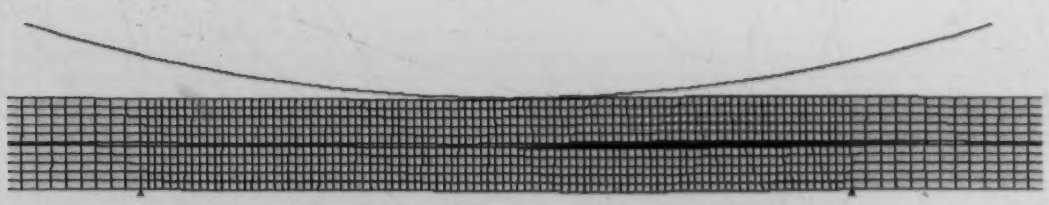

Figure 6.20 Residual strain in the 1/2-beam due to the swelling effect.

## 6.5 Conclusions

This chapter presents a new approach that uses cohesive damage material model and continuum elements in FEM to simulate damage initiation and propagation for the delamination fracture in fiber composites. The damage evolution law is based on the critical energy release rate; and the damage onset criterion takes into account the effect of

in-plane normal stress. The new approach has a major advantage over the existing interface-element-based approach in that the former can easily adopt any stress- or strain-based damage initiation criteria, benefited from the use of solid continuum elements.

It has been shown that with a simple bi-linear function for the damage evolution, the new cohesive damage material model can accurately predict the delamination development in either pure mode or mixed mode of fracture in fiber composites. The cohesive damage material model was firstly verified using benchmark problems such as the DCB, ENF, MMB and ELS tests, by comparing the simulation results with the analytical solutions, and then by the delamination development in the Beam specimens that did not contain any pre-crack. The study shows that the new approach predicts the fracture mode, the location for the delamination initiation and the final delamination size with good accuracy.

Parametric studies were conduced to investigate the sensitivity of the simulation to the damage initiation criterion, by using higher material strength values or ignoring the in-plane normal stress. Using the ELS test as an example, the results suggest that the damage initiation criterion for the cohesive zone plays a very minor role on the critical load for the onset of delamination growth from a starting defect (or a pre-crack). However, using the Beam test, the study shows that both the material strength for the cohesive zone and the form of damage initiation criterion have a significant effect on the critical load required for the delamination initiation.

A simulation using the 1/2-beam specimen was carried out to demonstrate the capability of modeling the swelling and friction in mode-II-dominated delamination. Though values of the parameters related to the swelling and friction need to be further

justified, the simulation results show some phenomena which are closer to the experiment observation but, to our knowledge, have never been obtained by others using FEM simulation, such as the hysteresis loop from cyclic loading and residual stress/strain in the cohesive layer after the delamination.

# Chapter 7 Conclusions and Future Work

## 7.1 Main conclusions

A framework has been proposed for the characterization and simulation of delamination in fiber reinforced composites. The critical energy release rate is the key parameter throughout all approaches developed in this study. The parameter serves as a measurement to assess the capability of composites to resist delamination propagation. It is also an ascertained quantity, in both analytical and numerical methods to govern the delamination development.

This study presented two analytical approaches for calculating the energy release rate with specified crack configurations and loading conditions. The first approach is the compliance method, which was reviewed and clarified for the limitation in its application. The second is the CTE analysis, which was redeveloped in a matrix form. Several examples were studied using both approaches and the results yielded essentially the same expressions for the energy release rate. The compliance method was also used to study the effect of the transverse shear force on the energy release rates in the mode II delamination tests, which concluded the irrelevancy of the shear force on the expression of the energy release rate in the force-controlled conditions. In addition, the CTE analysis was employed to derive a generalized formula to quantitatively assess the frictional force effect in beam-type mode II delamination tests.

The finite-element-based EDT was introduced to calculate the energy release rate for any quasi-static crack development problems. The EDT was shown for its accuracy in

predicting the energy release rate in composites in a variety of crack growth scenarios, including crack growth with friction and large deformation. Two additional examples other than composite materials were also presented, to demonstrate the capability of the EDT in complicated fracture situations. One is the deformation and fracture in nonlinear elastic, rubber-like materials, and the other is the crack growth in the elastic-plastic metals. Besides the excellent correlation with the results from the results in the literatures, the EDT also has good efficiency and the potential to deal with crack propagation problems that involve extensive, non-recoverable plastic deformation, for which any other existing method cannot be applied.

A new mechanical test, known as the INF test, was developed to quantify the mode II delamination toughness of composites. The INF test has the potential to be a standard mode II delamination test, together with the established mode I DCB test and mixed mode MMB test. The most significant feature of the INF test is its stable delamination growth, which has been proved theoretically and experimentally in this study. The INF test adopts 3-point bending that is the simplest fixture among all existing mode II delamination tests. In addition, the INF test is benefited from the newly developed data reduction method (DMC), to require only a load-displacement curve and the final crack length to establish the R-curve for the crack growth. Another advantage of the INF test is that the rate of delamination growth generated is proportional to the loading rate, thus making it possible to investigate the effect of the crack growth speed on the critical energy release rate. A series of the INF tests was conducted to investigate the sensitivity of the measured critical energy release rate to the test configurations and the fiber volume fraction. It was found that the geometrical parameters, such as the initial

crack length and the span length of the fixture, do not affect the measured value of the critical energy release rate, but the fiber volume fraction does. It was also discovered that the shear force interaction exists between the delamination surfaces generated in the INF test. The shear force, created by the bridging fibers, matrix hackles and stitching threads, provides explanations for the difference of the apparent crack length (from the compliance) to the visual crack length.

Analytical methods were used to explore possibilities of predicting the delamination development in the Beam test. Because the Beam test specimen contains an internal crack, thereby having two possible growing directions, two criteria were proposed to determine the crack growth rate in each direction, in order to determine the relation between the two crack front locations. The total crack length was then predicted using differential and integral forms of the energy release rate in a Beam specimen. Compared to the delamination length measured experimentally, the predicted values serve as the lower and upper bounds of the experimental values, suggesting that the analytical approaches provide a reasonable estimate for the delamination size developed in the Beam test.

A cohesive damage material model was developed to implement the CZM in the finite element codes for the delamination simulation. This approach has a major advantage over the traditional interface-element-based approach in that the former can easily adopt any stress- or strain-based damage initiation criteria. In this study, a novel criterion that takes into account the effect of in-plane normal stress was proposed for the damage initiation. The swelling and frictional force effects associated with mode-II-

dominated delamination were also implemented in the model to take into account the experimentally-revealed shear force interaction between the delaminated crack surfaces.

This cohesive damage material approach was verified in this study firstly by comparing the load-displacement curves and the mode mixing ratio from the finite element analysis, with the analytical solutions. Then, the approach was applied to the Beam test that does not contain any pre-cracks, to further verify the proposed damage initiation criteria. The study shows that the in-plane normal stress is crucial for successfully predicting the location for the delamination onset location and the final delamination size. Parametric studies were also carried out using ELS test and the Beam test to investigate the influence of the material strengths and other parameters in the damage initiation criteria on the simulation results. It is concluded that the material strength plays a very minor role in the situation that a starting defect (or a pre-crack) is in the structure, but has a significant effect on the delamination development in the defect-free composite structures.

Overall, systematic methods have been developed for the measurement of the critical energy release rate, including testing methods to generate delamination in the pure fracture mode and techniques to extract the critical energy release rate from the directly measurable quantities, such as force and displacement. Furthermore, analytical and numerical strategies have been proposed for the prediction of the delamination onset and propagation based on the critical energy release rate.

## 7.2 Future work

The results of experimental study of delamination (Chapter 4) using the INF and 4ENF tests have shown that both tests generate similar R-curves and average $G_{IIC}$ values, thus

giving confidence on the validity of the testing method. However, large amount of bridging fibers were also generated by these two tests. The bridging fiber introduces significant shear force interaction on the fracture surfaces, which affects the accuracy of the analytical analysis that is based on the assumption of stress-free fracture surfaces. It is speculated that that the bridging fibers are due to stable crack growth in these two tests, because stable crack growth may allow a bridging fiber to gradually peel off from the matrix. As a result, the amount of bridging fiber may be reduced by increasing the crack growth rate. However, it is not clear how the bridging fibers affect the delamination toughness. It is worthwhile to perform more INF test with varied loading speed to correlate the crack growth rate, amount of bridging fibers and the delamination toughness.

Mode III delamination, though less important than the mode I and II fractures, is not addressed in this study. A completed testing system for measuring the toughness of fiber composite should include this fracture mode. So the investigation on pure mode III and mixed mode delamination fracture with mode III involved is a new area to be explored.

To take mode III fracture into account is also a challenge for the finite element simulation of delamination into 3D cases. So far, the cohesive damage material model worked well in 2D simulations. The damage initiation criteria and the energy-based damage evolution law were all given based on 3D stress and energy states. If adopting the approach used by some interface elements [63], i.e. treating mode II and III equally as shear mode fracture, the proposed cohesive damage material model could be easily extended to 3D simulations. However, difficulty will be encountered if mode III fracture has to be distinguished from mode II, such as when similar amount of energies were

consumed by mode II and mode III fractures and $G_{IIIC}$ is quite different from $G_{IIC}$. In this case, the crack front profile is need to separate the energy consumed in the plane perpendicular to the crack profile from $U_{shear}$ (Eq. (6.7)), the former is the energy loss by mode II deformation and the later $U_{shear}$ is summation of energy loss of both mode II and III. The above discussion only provides a possible approach for mode separation strategy. There might be other ways to separate fracture modes, which need our further investigation.

# References


[1]. Anon. Farnborough 2004 - Good prospects for aerospace composites. *Reinforced Plast* 2004; 48(8): 42-46.

[2]. ASTM D5528-01. Standard Test Method for Mode I Interlaminar Fracture Toughness of Unidirectional Fiber-Reinforced Polymer Matrix Composites. *Annual Book of ASTM Standards* 2000; 15.03.

[3]. ASTM D 6671/D 6671M-04e1. Standard Test Method for Mixed Mode I-Mode II Interlaminar Fracture Toughness of Unidirectional Fiber Reinforced Polymer Matrix Composites. *Annual Book of ASTM Standards* 2005; 13.05.

[4]. Carlsson LA, Gillespie JWJ, Pipes RB. On the analysis and design of the end notched flexure (ENF) specimen for mode II testing. *J Composite Mater* 1986; 20(6): 594-604.

[5]. Zhou J, He T. On the analysis of the end-notched flexure specimen for measuring mode II fracture toughness of composite materials. *Composites Sci Technol* 1994; 50(2): 209-213.

[6]. Corleto CR, Hogan HA. Energy release rates for the ENF specimen using a beam on an elastic foundation. *J Composite Mater* 1995; 29(11): 1437-1457.

[7]. Schapery RA, Davidson BD. Prediction of Energy Release Rate for Mixed-Mode Delamination Using Classical Plate Theory. *Appl Mech Rev* 1990; 43(5): s281-s287.

[8]. Gere JM, Timoshenko S. *Mechanics of materials.* 3rd edition, UK: Chapman & Hall, 1991; 807.

[9]. Irwin GR.Onset of Fast Crack Propagation in High Strength Steel and Aluminum Alloys. In: *Sagamore Research Conference Proceedings*, 1956. p. 289-305.

[10]. Kageyama K, Kimpara I, Suzuki T, Ohsawa I, Kanai M, Tsuno. Effects of test conditions on mode II interlaminar fracture toughness of four-point ENF specimens. In: *Proceedings of the ICCM-12*, Paris, France: July 1999.

[11]. Wang Y, Williams JG. Corrections for Mode II fracture toughness specimens of composites materials. *Composites Sci Technol* 1992; 43(3): 251-256.

[12]. Salpekar SA, Raju IS, O'Brien TK. Strain energy release rate analysis of the end-notched flexure specimen using the finite-element method. *J Composites Technol Res* 1988; 10(4): 133-9.

[13]. Rybicki EF, Kanninen MF. A finite element calculation of stress intensity factors by a modified crack closure integral. *Eng Fract Mech* 1977; 9(4): 931-8.

[14]. Xie D, Waas AM, Shahwan KW, Schroeder JA, Boeman RG. Fracture criterion for kinking cracks in a tri-material adhesively bonded joint under mixed mode loading. *Eng Fract Mech* 2005; 72(16): 2487-2504.

[15]. Xie D, Waas AM, Shahwan KW, Schroeder JA, Boeman RG. Computation of energy release rates for kinking cracks based on virtual crack closure technique. *CMES - Computer Modeling in Engineering and Sciences* 2004; 6(6): 515-524.

[16]. *ABAQUS Verification Manual.* Version 6.5, United States of America: ABAQUS Inc., 2004.

[17]. Shih CF, Needleman A. Fully plastic crack problems. I. Solutions by a penalty method. *Transactions of the ASME Journal of Applied Mechanics* 1984; 51(1): 48-56.

[18]. Shih CF, Needleman A. Fully plastic crack problems. II. Application of consistency checks. *Transactions of the ASME Journal of Applied Mechanics* 1984; 51(1): 57-64.

[19]. Salpekar SA, Raju IS, Obrien TK. (1987). Strain-Energy-Release Rate Analysis of the End-Notched Flexure Specimen Using the Finite-Element Method. *J.Composites Technol.Res* 1988; 10(4): 133-139.

[20]. Shivakumar KN, Tan PW, Newman JC,Jr. A virtual crack-closure technique for calculating stress intensity factors for cracked three dimensional bodies. *Int J Fract* 1988; 36: 43-50.

[21]. Shih CF, Moran B, Nakamura T. Energy release rate along a there-dimensional crack front in a thermally stressed body. *Int J Fract* 1986; 30: 79-102.

[22]. Wang W, Takao Y, Nakata M. Effects of friction on the measurement of the mode II interlaminar fracture toughness of composite laminates. In: *Proceedings of 14th International Conference on Composite Materials (ICCM-14)*, San Diego, Califonia USA. San Diego, Califonia USA: 2003. p. 1-8.

[23]. Schuecker C, Davidson BD. Effect of friction on the perceived mode II delamination toughness from three- and four-point bend end-notched flexure tests. *ASTM Spec Tech Publ* 2000(1383): 334-344.

[24]. Davidson BD, Sun X. Effects of friction, geometry, and fixture compliance on the perceived toughness from three-and four-point bend end-notched flexure tests. *J Reinf Plast Compos* 2005; 24(15): 1611-1628.

[25]. Mall S, Kochhar NK. Finite-element analysis of end-notch flexure specimens. *J Compos Technol Res* 1986; 8(2): 54-57.

[26]. Yeoh OH. Relation between crack surface displacements and strain energy release rate in thin rubber sheets. *Mech Mater* 2002; 34(8): 459-74.

[27]. Yeoh OH. Some forms of the strain energy function for rubber. *Rubber Chemistry and Technology* 1993; 66(5): 754-771.

[28]. Kumar V, German MD, Shih CF. (July 1981). Engineering approach for elastic-plastic fracture analysis. Report No.: EPRI-NP-1931.

[29]. Kuboki T, Jar P-B, Cheng JJR. Interlaminar fracture toughness and the associated fracture behavior for glass fiber reinforced polymers (GFRP). *J Mater Sci* 2004; 39(4): 1419-1423.

[30]. O'Brien TK. Interlaminar fracture toughness: The long and winding road to standardization. *Compos Part B:Eng* 1998; 29(1): 57-62.

[31]. Anderson TL. *Fracture mechanics.* 2nd ed., Florida: CRC Press LLC, 1995.

[32]. Reeder JR. (1992). Evaluation of Mixed-Mode Delamination Failure Criteria. Report No.: NAS 1.15:104210. United States: .

[33]. Benzeggagh ML, Kenane M. Measurement of mixed-mode delamination fracture toughness of unidirectional glass/epoxy composites with mixed-mode bending apparatus. *Composites Sci Technol* 1996; 56(4): 439-449.

[34]. Blackman BRK, Brunner AJ, Williams JG. Mode II fracture testing of composites: a new look at an old problem. *Eng Fract Mech* 2006; 73(16): 2443-2455.

[35]. Szekrenyes A, Uj J. Mode-II fracture in E-glass-polyester composite. *J Composite Mater* 2005; 39(1): 1747-1768.

[36]. Davies P, Sims GD, Blackman BRK, Brunner AJ, Kageyama K, Hojo M, Tanaka K, Murri G, Rousseau C, Gieseke B, Martin RH. Comparison of test configurations for

determination of mode II interlaminar fracture toughness results from international collaborative test programme. *Plastics, Rubber and Composites* 1999; 28(9): 432-437.

[37]. Martin RH, Davidson BD. Mode II fracture toughness evaluation using four point bend, end notched flexure test. *Plastics, Rubber and Composites* 1999; 28(8): 401-6.

[38]. Kuboki T, Gallagher E, Jar P-B, Cheng JJR. A new method to quantify delamination resistance of fibre reinforced polymers (FRP) under transverse loading. *Applied Composite Materials* 2005; 12(2): 93-108.

[39]. Jar P-B, Dick TM. Comparison of testing methods for fibre-reinforced polymers (FRP) in resistance to in-plane sliding mode of delamination (mode II). *J Mater Sci* 2005; 40(6): 1481-4.

[40]. Gallagher E, Kuboki T, Jar P-B, Cheng JJR. Characterization of delamination resistance of fibre reinforced polymers (FRP) under transverse loading using a newly developed beam test. In: *ANTEC 2004 - Annual Technical Conference Proceedings*, May 16-20 2004, Chicago, IL., United States: Society of Plastics Engineers; 2004. p. 1364-1368.

[41]. Fan C, Ben Jar P-, Roger Cheng JJ. Energy-based analyses of delamination development in fibre-reinforced polymers under 3-point bending. *Composites Sci Technol* 2006; 66(1): 2143-2155.

[42]. Seung-Hwan Lee, Noguchi H, Young-Bae Kim, Seong-Kyun Cheong. Effect of interleaved non-woven carbon tissue on interlaminar fracture toughness of laminated composites. I. Mode II. *J Composite Mater* 2002; 36(18): 2153-68.

[43]. Hwang JH, Lee CS, Hwang W. Effect of crack propagation directions on the interlaminar fracture toughness of carbon/epoxy composite materials. *Applied Composite Materials* 2001; 8(6): 411-33.

[44]. Zile E, Tamuzs V. Mode II delamination of a unidirectional carbon fiber/epoxy composite in four-point bend end-notched flexure tests. *Mechanics of Composite Materials* 2005; 41(5): 383-390.

[45]. Hashemi S, Kinloch AJ, Williams JG. The analysis of interlaminar fracture in uniaxial fibre-polymer composites. *Proceedings of the Royal Society of London, Series A (Mathematical and Physical Sciences)* 1990; 427(1872): 173-99.

[46]. Choi HY, Downs RJ, Chang F. New approach toward understanding damage mechanisms and mechanics of laminated composites due to low-velocity impact. Part I. Experiments. *J Composite Mater* 1991; 25(8): 992-1011.

[47]. Schuecker C, Davidson BD. Evaluation of the accuracy of the four-point bend end-notched flexure test for mode II delamination toughness determination. *Composites Sci Technol* 2000; 60(11): 2137-2146.

[48]. Shi YB, Hull D, Price JN. Mode II fracture of + θ/-θ; angled laminate interfaces. *Composites Sci Technol* 1993; 47(2): 173-184.

[49]. Vinciquerra AJ, Davidson BD. Effect of crack length measurement technique and data reduction procedures on the perceived toughness from four-point bend end-notched flexure tests. *J Reinf Plast Compos* 2004; 23(10): 1051-62.

[50]. Davies P, Casari P, Carlsson LA. Influence of fibre volume fraction on mode II interlaminar fracture toughness of glass/epoxy using the 4ENF specimen. *Composites Sci Technol* 2005; 65(2): 295-300.

[51]. Williams JG. *Fracture Mechanics of Polymers.* New York: Ellis Horwood Limited, 1984; 302.

[52]. Cui W, Wisnom MR. Combined stress-based and fracture-mechanics-based model for predicting delamination in composites. *Composites* 1993; 24(6): 467-474.

[53]. Wisnom MR. Shear fracture of unidirectional composites without initial cracks. *Composites Sci Technol* 1994; 52(1): 9-17.

[54]. Wisnom MR. Modelling the effect of cracks on interlaminar shear strength. *Composites - Part A: Applied Science and Manufacturing* 1996; 27(1): 17.

[55]. Wisnom MR. Modelling of stable and unstable fracture of short beam shear specimens. *Composites* 1994; 25(6): 394-400.

[56]. Weicheng Cui, Wisnom MR, Jones M. Effect of specimen size on interlaminar shear strength of unidirectional carbon fibre-epoxy. *Composites Engineering* 1994; 4(3): 299-307.

[57]. Yan A-, Marechal E, Nguyen-Dang H. A finite-element model of mixed-mode delamination in laminated composites with an R-curve effect. *Composites Sci Technol* 2001; 61(10): 1413-1427.

[58]. Alfano G, Crisfield MA. Solution strategies for the delamination analysis based on a combination of local-control arc-length and line searches. *Int J Numer Methods Eng* 2003; 58(7): 999-1048.

[59]. Alfano G, Crisfield MA. Finite element interface models for the delamination analysis of laminated composites: Mechanical and computational issues. *Int J Numer Methods Eng* 2001; 50(7): 1701-1736.

[60]. Blackman BRK, Hadavinia H, Kinloch AJ, Williams JG. The use of a cohesive zone model to study the fracture of fibre composites and adhesively-bonded joints. *Int J Fract* 2003; 119(1): 25-46.

[61]. Bui VQ, Marechal E, Nguyen-Dang H. Imperfect interlaminar interfaces in laminated composites: Interlaminar stresses and strain-energy release rates. *Composites Sci Technol* 2000; 60(1): 131-143.

[62]. Camanho PP, Davila CG, Pinho SS. Fracture analysis of composite co-cured structural joints using decohesion elements. *Fatigue and Fracture of Engineering Materials and Structures* 2004; 27(9): 745-757.

[63]. Camanho PP, Davila CG, De Moura MF. Numerical simulation of mixed-mode progressive delamination in composite materials. *J Composite Mater* 2003; 37(16): 1415-1438.

[64]. Qiu Y, Crisfield MA, Alfano G. An interface element formulation for the simulation of delamination with buckling. *Eng Fract Mech* 2001; 68(16): 1755-76.

[65]. Corigliano A. Formulation, identification and use of interface models in the numerical analysis of composite delamination. *Int J Solids Structures* 1993; 30(20): 2779-2811.

[66]. Crisfield MA, Alfano G. Adaptive hierarchical enrichment for delamination fracture using a decohesive zone model. *Int J Numer Methods Eng* 2002; 54(9): 1369-1390.

[67]. Davila CG, Camanho PP. Analysis of the effects of residual strains and defects on skin/stiffener debonding using decohesion elements. In: *44th AIAA/ASME/ASCE/AHS/*

*ASC Structures, Structural Dynamics, and Materials Conference*, Apr 7-10 2003, Norfolk, VA, United States: American Inst. Aeronautics and Astronautics Inc; 2003. p. 600-608.

[68]. Davila CG, Camanho PP, De Moura MF. Mixed-mode decohesion elements for analyses of progressive delamination. In: *42nd AIAA/ASME/ASCE/AHS/ASC Structures, Structural Dynamics, and Materials Conference and Exhibit Technical Papers*, Apr 16-19 2001, Seattle, WA: American Inst. Aeronautics and Astronautics Inc; 2001. p. 2277-2288.

[69]. de Moura MFSF, Goncalves JPM, Marques AT, de Castro PMST. Prediction of compressive strength of carbon-epoxy laminates containing delamination by using a mixed-mode damage model. *Composite Structures* 2000; 50(2): 151-157.

[70]. de Moura MFSF, Goncalves JPM, Marques AT, de Castro PMST. Modeling compression failure after low velocity impact on laminated composites using interface elements. *J Composite Mater* 1997; 31(15): 1462-1479.

[71]. El-Sayed S, Sridharan S. Predicting and tracking interlaminar crack growth in composites using a cohesive layer model. *Compos Part B:Eng* 2001; 32(6): 545-553.

[72]. Liu D, Xu L, Lu X. Stress analysis of imperfect composite laminates with an interlaminar bonding theory. *Int J Numer Methods Eng* 1994; 37(16): 2819-2839.

[73]. Mi Y, Crisfield MA, Davies GAO, Hellweg H-. Progressive delamination using interface elements. *J Composite Mater* 1998; 32(14): 1246-1272.

[74]. Pantano A, Averill RC. A mesh-independent interface technology for simulation of mixed-mode delamination growth. *Int J Solids Structures* 2004; 41(14): 3809-3831.

[75]. Turon A, Camanho PP, Costa J, Davila CG. (2004). Interface Damage Model for the Simulation of Delamination Under Variable-Mode Ratio in Composite Materials. Report No.: NASA/TM-2004-213277. United States: .

[76]. Turon A, Davila CG, Camanho PP, Costa J. (2005). Engineering Solution for Using Coarse Meshes in the Simulation of Delamination with Cohesive Zone Models. Report No.: NASA/TM-2005-213547. United States: .

[77]. Xu X-, Needleman A. Numerical simulations of fast crack growth in brittle solids. *J Mech Phys Solids* 1994; 42(9): 1397-1434.

[78]. Goyal VK, Johnson ER, Davila CG. Irreversible constitutive law for modeling the delamination process using interfacial surface discontinuities. *Composite Structures* 2004; 65(3-4): 289-305.

[79]. Tvergaard V, Hutchinson JW. The relation between crack growth resistance and fracture process parameters in elastic-plastic solids. *J Mech Phys Solids* 1992; 40(6): 1377-97.

[80]. Turon A, Camanho PP, Costa J, Davila CG. A damage model for the simulation of delamination in advanced composites under variable-mode loading. *Mech Mater* 2006; 38(11): 1072-1089.

[81]. Choi HY, Wu HT, Chang F. New approach toward understanding damage mechanisms and mechanics of laminated composites due to low-velocity impact. Part II. Analysis. *J Composite Mater* 1991; 25(8): 1012-1038.

[82]. Yuen S, Fan C, Kuboki T, Jar P-B, Forest TW, Cheng JJR. Delamination resistance of fibre-reinforced polymers (FRP) under transverse loading - Criteria for on-set of delamination. In: *ANTEC 2004 - Annual Technical Conference Proceedings*, May

16-20 2004, Chicago, IL., United States: Society of Plastics Engineers; 2004. p. 1374-1378.

[83]. Hou JP, Petrinic N, Ruiz C, Hallett SR. Prediction of impact damage in composite plates. *Composites Sci Technol* 2000; 60(2): 273-281.

[84]. Hou JP, Petrinic N, Ruiz C. A delamination criterion for laminated composites under low-velocity impact. *Composites Sci Technol* 2001; 61(14): 2069-2074.

[85]. Lemaitre J, Desmorat R. *Engineering damage Mechanics.* Springer-Verlag Berlin Heidelberg, 2005; 380.

[86]. Hoppel CP, Bogetti TA, Gillespie JW. (1995). Effects of Hydrostatic Pressure on the Mechanical Behavior of Composite Materials. Report No.: Army Research Lab.: ARL-TR-727. United States: .

[87]. Sediadi Y, Jar P-B, Cheng, J. J. Roger. Evaluation of toughness transfer from matrix to random-fibre-reinforced polymers (FRP) under Cyclic Loading. In: *Proceedings of the Fifth Canadian-International Composites Conference*, UBC, Vancouver. 2005. p. 1-12.